

MODELING AND SIMULATION OF COMPOSITIONAL ENGINEERING IN SIGE
FILMS USING PATTERNED STRESS FIELDS

Daniel Kaiser

A DISSERTATION

in

Chemical and Biomolecular Engineering

Presented to the Faculties of the University of Pennsylvania

in

Partial Fulfillment of the Requirements for the

Degree of Doctor of Philosophy

2016

Supervisor of Dissertation

Talid Sinno, Professor of Chemical and Biomolecular Engineering

Graduate Group Chairperson

Talid Sinno, Professor of Chemical and Biomolecular Engineering

Dissertation Committee:

Dr. Robert Riggelman, Assistant Professor of Chemical and Biomolecular Engineering

Dr. Amish Patel, Assistant Professor of Chemical and Biomolecular Engineering

Dr. John Bassani, Professor of Materials Science and Engineering

ACKNOWLEDGMENTS

I would first and foremost like to thank my advisor, Prof. Talid Sinno, who spent countless hours helping me to analyze every aspect of what I present in this thesis and, most importantly, to grow as both a student and future independent researcher. I would also like to thank my thesis committee, Prof. Robert Riggleman, Prof. Amish Patel, and Prof. John Bassani, for the extremely helpful discussions as my research progressed, and for helping me to understand the core engineering principles through my coursework. On a personal note, I would like to thank my parents, Steven Kaiser and Phyllis Jacobs, and my brother, William Kaiser, without whom I would never have had the courage to go back to graduate school after years in the workforce, and who have supported me throughout every endeavor my entire life. Finally, last but certainly not least, I would like to thank my girlfriend, and love of my life, Jennifer Horne, who has made the stressful times during my PhD studies bearable, and who has kept me going every day as I worked to complete this Thesis.

ABSTRACT

MODELING AND SIMULATION OF COMPOSITIONAL ENGINEERING IN SiGe FILMS USING PATTERNED STRESS FIELDS

Daniel Kaiser

Prof. Talid Sinno

Semiconductor alloys such as silicon-germanium (SiGe) offer attractive environments for engineering quantum-confined structures that are the basis for a host of current and future optoelectronic devices. Although vertical stacking of such structures is routinely achieved via heteroepitaxy, lateral manipulation has proven much more challenging. I describe a new approach that suggests that a patterned elastic stress field generated with an array of nanoscale indenters in an initially compositionally uniform SiGe substrate will drive atomic interdiffusion, leading to compositional patterns in the near-surface region of the substrate. While this approach may offer a potentially efficient and robust pathway to producing laterally ordered arrays of quantum-confined structures, there is a large set of parameters important to the process. Thus, it is difficult to consider this approach using only costly experiments, which necessitates detailed computational analysis.

First, I review computational approaches to simulating the long length and time scales required for this process, and I develop and present a mesoscopic model based on coarse-grained lattice kinetic Monte Carlo that quantitatively describes the atomic interdiffusion processes in SiGe alloy film subjected to applied stress. I show that the model provides predictions that are quantitatively consistent with experimental measurements, and I examine the impact of basic indenter geometries on the patterning

process. Second, I extend the model to investigate the impact of several process parameters, such as more complicated indenter shapes and pitches. I find that certain indenter configurations produce compositional patterns that are favorable for use as lateral arrays of quantum-confined structures. Finally, I measure a set of important physical parameters, the so-called “activation volumes” that describes the impact of stress on diffusion. The values of these parameters are not well established in the literature. I make quantitative connections to the range of values found in the literature and characterize the effects of different stress states on the overall patterning process. Finally, I conclude with ideas about alternative pathways to quantum confined structure generation and possible extensions of the framework developed.

TABLE OF CONTENTS

ACKNOWLEDGMENTS	ii
ABSTRACT.....	iii
TABLE OF CONTENTS	v
LIST OF TABLES	ix
LIST OF FIGURES	x
Chapter 1. Introduction	1
1.1 Surface Stress Mediated Patterning of Compositional Rearrangement	10
Chapter 2. Demonstration of Stress-Directed Patterning in SiGe	15
2.1 Introduction.....	15
2.2 Experimental Findings	17
2.3 Conclusions.....	22
Chapter 3. Review of Computational Approaches	24
3.1 Metropolis Monte Carlo.....	29
3.2 Kinetic Monte Carlo Method	30
3.3 Continuum Methods.....	38
3.4 Conclusions.....	42
Chapter 4. Computational Analysis of Interdiffusion in Silicon-Germanium Heterosystem for Axisymmetric and Two-Dimensional Geometries.....	43
4.1 Introduction.....	43
4.2 Model for Atomic Diffusion in SiGe	45
4.2.1 Diffusion of Point Defects Under Stress.....	51

4.3	Simulation Details.....	53
4.3.1	Lattice Kinetic Monte Carlo (LKMC) Simulation Framework	53
4.3.2	Rate Modifications Due to Stress and Compositional Gradients...	58
4.3.3	Continuum Stress Field Calculation Framework	62
4.3.4	Atomistic Stress Field Comparison	65
4.4	Simulation Results	71
4.5	Conclusions.....	89
Chapter 5. Generating Ge Quantum Dots Using Complex Nanoindenter Geometries and Annealing Schedules		92
5.1	Introduction.....	92
5.2	Lattice Kinetic Monte Carlo (LKMC) Model.....	93
5.2.1	“Net event” LKMC Framework.....	94
5.2.2	Multiresolution LKMC	96
5.3	Continuum Stress Calculation.....	99
5.3.1	Analysis of Mesh Used During Stress Computation	101
5.4	Results and Discussion	105
5.4.1	Indenter Size	107
5.4.2	Indenter Spacing (Pitch)	109
5.4.3	Indenter Array Patterns	110
5.4.4	Indenter Shape	111
5.4.5	Film Ge Concentration.....	115
5.5	Variable Stress Anneals	116
5.6	Conclusions.....	119

Chapter 6. Analysis of Point Defect Diffusion In Stressed Si and Ge	121
6.1 Introduction.....	121
6.2 Theoretical Formalism for Stress Impact on Point Defect Thermophysical Properties	123
6.2.1 Point Defect Formation in a Stress Field	125
6.2.2 Point Defect Diffusion in a Stress Field	128
6.3 Computational Details	131
6.4 Results.....	132
6.4.1 Quantitative Analysis of Formation Volume Tensor.....	132
6.4.2 Quantitative Analysis of Migration Volume Tensor	137
6.4.3 Impact of Different Stress States on Atomic Diffusion	145
6.5 Conclusions.....	150
Chapter 7. Conclusions and Future Work	151
7.1 Summary.....	151
7.2 Future Work	154
7.2.1 Optimization of Vast Parametric Space Relevant to Compositional Redistribtution.....	154
7.2.2 Alternative Pathways to Ge Quantum Confined Structure Generation.....	155
7.2.3 Compositional Redistribution in Semiconductor Heterosystems Other Than SiGe	158
Appendix 1. Results From Activation Volume Studies	159

BIBLIOGRAPHY 189

LIST OF TABLES

Table 4.1. Parameters used for point defect and self-diffusion in Si, Ge and $\text{Si}_{1-x}\text{Ge}_x$. A denotes the defect type. Taken from ref. [38].	48
Table 4.2. Elastic constants for Si, Ge and $\text{Si}_{0.8}\text{Ge}_{0.2}$. Taken from ref. [91].	64
Table 4.3. Elastic constants for $\text{Si}_{0.8}\text{Ge}_{0.2}$. Tersoff potential values for film and Poisson's ratio of indenter taken from ref. [94]	70
Table 5.1. Parametric space considered in this Chapter, with relevant subsection considered.	105
Table 6.1. Defect concentration stress dependence, computed via molecular statics simulations. The equation model is $a\sigma^4 + b\sigma^3 + c\sigma^2 + d\sigma + e$, with σ in GPa. Note that e always is zero. See text for details on computation.	133
Table 6.2. Traces of relaxation volume tensor for Si as previously reported in the literature. All values correspond to zero hydrostatic pressure.	135
Table 6.3. Temperatures considered when conducting molecular dynamics, along with the melting temperatures for the potentials used in the calculation. The melting temperature found experimentally is 1683 K for silicon and 1210 K for germanium, as stated in ref. [129].	138
Table 6.4. Defect diffusivity stress dependence, computed via molecular dynamics simulations. The equation model is $a\sigma^4 + b\sigma^3 + c\sigma^2 + d\sigma + e$, with σ in GPa. Note that e always is zero. See text for details on computation.	139

LIST OF FIGURES

Figure 1.1. Shrinking of computer chip length scales with time. Perfect exponential shrinking law, as predicted by Moore, is shown with green line. Adapted from ref. [9]. ..	2
Figure 1.2. Schematic representation of three epitaxial growth pathways, starting from one monolayer of coverage to increasing coverage. Taken from ref. [10].	4
Figure 1.3. (a) InAs dots on GaAs (scale 100 nm). Taken from ref. [11] (b) Pyramid/hut (P) and dome (D) nanoclusters of Ge/Si (30% Ge) on Si (scale ~10 nm). Taken from ref. [12] (c) Ge hut cluster on Si (scan area is 40 nm × 40 nm and island height is 2.8nm). Taken from ref. [13].	4
Figure 1.4. (a) Bulk material with no quantum confinement and a continuous density of energy states (b) Quantum well, a material with one-dimensional quantum confinement, and a reduced energy density of states (c) Quantum wire, a material with two-dimensional quantum confinement, and a further reduced energy density of states (d) Quantum dot (QD), or three dimensionally quantum confined material, with delta function for energy density of states. Taken from ref. [21].	6
Figure 1.5. (a) Si _{0.50} Ge _{0.50} /Si superlattice with ATG undulations. Taken from ref. [27] (b) Ge dots aligning with undulations in Si/SiGe superlattice. Taken from ref. [28] (c) Bright Ge islands grown on vicinal Si (001). Taken from ref. [23] (d) Lithography/RIE (Reactive Ion Etching)-created pits lead to patterned Ge dots. Taken from ref. [24] (e) Atomic Force Microscopy scan and schematic of Ge dots on Si surface with patterned oxide. Taken from ref. [25] (f) Patterned Ga ion implanted seen to guide nucleation sites for Ge islands on Si. Taken from ref. [26].	9
Figure 1.6. (a) Schematic of InGaAs lines on the surface of the AlGaAs/GaAs heterostructure (b) Plan view transmission electron microscopy micrograph of an array of As particles below stressor lines. Taken from ref. [29].	11
Figure 1.7. A nanopillar template is applied to a SiGe wafer (a,b). During annealing, larger Ge atoms preferentially diffuse away from areas of compression, creating patches of enhanced Si content (c).	12
Figure 2.1. (a) Schematic representation of assembly used to create patterned stress fields in a SiGe substrate. (b) SEM image of Si nanopillar array used to apply a patterned stress field to the SiGe substrate. (c) Steps in the stress transfer process: (i) place Si nanopillar indenter array on top of SiGe substrate, (ii) press the indenters against the substrate, and (iii) thermally anneal the stack under patterned stress field.	16
Figure 2.2. SEM images of Si _{0.8} Ge _{0.2} substrates subjected to patterned stress fields and annealed for 3 hours, as a function of annealing temperature and maximum contact pressure. Each panel represents a region with dimension 1200 nm × 1200 nm.	18

Figure 2.3. Atomic percentage of Si and Ge near the surface of indented SiGe substrate. Case (a): $T = 1000\text{ }^{\circ}\text{C}$, $P = 35\text{ GPa}$. Case (b): $T = 1000\text{ }^{\circ}\text{C}$, $P = 45\text{ GPa}$. Case (c): $T = 1000\text{ }^{\circ}\text{C}$, $P = 40\text{ GPa}$. Inset TEM images show (a) complete Ge depletion with elastic deformation, (b) no discernable compositional change with plastic deformation, and (c) intermediate case with highly localized Ge depletion. 21

Figure 3.1. Schematic of defect mediated atomic diffusion. Red atoms represent Si and blue atoms represent Ge: (a) vacancy-enabled Si motion, (b) vacancy-enabled Ge motion, (c) Si interstitial ‘kicks out’ a Ge atom creating a Ge interstitial, and (d) a Ge interstitial kicks out an Si atom creating an Si interstitial..... 24

Figure 3.2. Concentration (a), diffusivity (b), and transport capacity (c) of neutral vacancies in silicon as a function of temperature. 26

Figure 3.3. Schematic of different computational techniques and accessible length and time scales..... 28

Figure 3.4. (a) Schematic of applied surface strain field to generate stresses in substrate (b) xz -cross section of film showing compositional evolution as a function of sweeps. Smaller B atoms (light gray) preferentially aggregate in regions of high stress. Taken from ref. [30]..... 30

Figure 3.5. Schematic of KMC algorithm 32

Figure 3.6. (a) Snapshot of vacancy clusters in silicon. Taken from ref. [44] (b) Single atom-thick island distribution (squares) during deposition on a patterned surface predicted by KMC. Here, the binding energy between substrate and adatom varies sinusoidally in x and y . Left – configuration at coverage 0.15 ($T=400\text{K}$); right – configuration after coarsening at $T=800\text{K}$. Taken from ref. [45] (c) Dewetting and islanding seen after three monolayers of growth. Taken from ref. [48] (d) Ripening of islands of Al on Al surface. Taken from ref. [50]..... 35

Figure 3.7. (a) Domain decomposition into nine regions, with shaded “ghost” regions and solid “skin” regions for the central domain. The ghost region of one domain is the skin region of its neighbor (b) Parallel efficiency, versus number of CPU cores (PEs), defined as the ratio of CPU time on one core for N rates divided by the CPU time on PE cores for $\text{PE}\times N$ rates., for some model diffusion systems. Taken from ref. [51]. 36

Figure 3.8. Temporal evolution of phase aggregation in the presence of periodic applied strain. The red regions are negatively (tensile) strained precipitates, which is equivalent to smaller atoms aggregating in regions of imposed compression. Taken from ref. [69]. 41

Figure 4.1. (a) Si and (b) Ge self-diffusivity at various temperatures in unstrained SiGe alloys of different compositions. (c) Transport capacities in pure, unstrained, Ge and Si as a function of inverse temperature. Solid lines and white symbols are DC_v and dashed lines and black symbols are DC_I . Symbols are literature values and lines are model fits. Taken from ref. [38]..... 50

Figure 4.2. (a) Schematic of LKMC domain comprised of cubic cells measuring L_{cell} in length and containing n_{tot} Si and/or Ge atoms (b) Schematic of coarse-graining atomic configurations in cells. Red atoms represent Si and blue atoms represent Ge (c) Schematic of LKMC switch move. In the depicted exchange, a Ge atom is moving from the lower left to the lower right and an Si atom is moving from the lower right to the lower left. 55

Figure 4.3. Energy change for an Si→Ge identity flip in a 64-atom cubic Si_xGe_{1-x} cell at different combinations of stress state and composition. (a) Uniaxial stress, (b) biaxial stress, and (c) hydrostatic stress. Ge→Si identity flips lead to equal and opposite energy changes..... 61

Figure 4.4. Schematic of simulator algorithm using stress field computed from molecular statics. See text for details..... 67

Figure 4.5. Binned atomistic pressure (circles) and quadratic fit (line, $R^2 > 0.999$) as a function of distance normal to the contact point between the 50-nm-diameter cylindrical indenter and substrate, predicted by quasi-static indentation of a $Si_{0.8}Ge_{0.2}$ slab. The annular segments used to bin the pressures are 3 nm wide (centered below the indenter) and 0.5 nm thick. The σ_{zz} profile shown here corresponds to an indenter applied with a force per length of 6.57×10^{-8} N/nm..... 69

Figure 4.6. Maximum contact pressure obtained from energy minimization of an atomistic model (red line), along with the continuum analysis fit to the data (green line), for the indentation of a $Si_{0.8}Ge_{0.2}$ film using a 25 nm (radius) cylindrical indenter. See text for details. 71

Figure 4.7. (a) Stress (σ_{zz}) in the xz -plane generated by an infinite (in y) cylindrical wire indenter of diameter 80 nm, corresponding to a maximum contact pressure of 15 GPa, mapped onto the undeformed domain. Result from plane strain calculation assuming isotropic elasticity. (b) FEM mesh used to generate the stress field in (a) (c) Indenter force versus maximum contact pressure for 80 nm-diameter, infinitely long, cylindrical indenter against $Si_{0.8}Ge_{0.2}$. Blue line – anisotropic elasticity, green line – isotropic elasticity, black dashed line – Hertz contact model..... 74

Figure 4.8. Simulated Ge concentration profiles (a,b) in an initially uniform $Si_{0.8}Ge_{0.2}$ film following 3 hours of thermal annealing at 1000 °C under stresses (c,d) induced by contact with an 80 nm-diameter spherical indenter with maximum contact pressure of 9 GPa (a,c) and 35 GPa (b,d). Note that (a)-(d) show an xz -plane of the three-dimensional simulation domain taken at the center of contact in y ; this convention is used throughout the Chapter. (e) Scanning electron microscopy (SEM) image of the Si nanopillar indenter array used in the experiments reported in Chapter 2. (f) Near-surface (see text) Ge concentration as a function of x -position. Black line—experimental EDS measurement with maximum contact pressure ~ 35 GPa (based on Hertz contact model), blue line—LKMC with maximum contact pressure 9 GPa, red line—LKMC simulation with maximum contact pressure 21 GPa, purple line—LKMC with maximum contact pressure

35 GPa. All LKMC simulations performed with coarse cell size $L_{cell}=6.56$ nm. Note that the simulation profiles in (f) represent two copies of the actual simulation domain. 78

Figure 4.9. Ge concentration profiles in the top layer of coarse cells of a $Si_{0.8}Ge_{0.2}$ substrate subjected to a 80 nm-diameter cylindrical wire indenter following 3 hours of annealing at 1000 °C. The maximum contact pressure was 18 GPa. Individual profiles obtained with different LKMC coarse cell sizes: Gray— $L_{cell}=2.19$ nm (512 atoms/cell), blue— $L_{cell}=3.28$ nm (1,728 atoms/cell), orange— $L_{cell}=4.37$ nm (4,096 atoms/cell), pink— $L_{cell}=6.56$ nm (13,824 atoms/cell). Note that all wire indenter simulations are based on two-dimensional LKMC domains that are a single cell thick in the y -direction. 80

Figure 4.10. Steady-state Ge concentration profiles in top layer of LKMC cells of an initially uniform $Si_{0.8}Ge_{0.2}$ film subjected to an 80 nm-diameter wire indenter (maximum contact pressure of 18 GPa) and annealed at 1000 °C. Red line—elastic constants corresponding to initial (uniform) composition, blue line—with lattice mismatch and elastic constants corresponding to spatially-varying steady-state compositional profile. 81

Figure 4.11. Simulated Ge concentration profiles (a,b) in an initially uniform $Si_{0.8}Ge_{0.2}$ film following 3 hours of thermal annealing at 1000 °C under stresses (c,d) induced by contact with (a) an 80 nm-diameter spherical indenter, and (b) an 80 nm-diameter wire indenter, both with maximum contact pressure of 18 GPa. (e) Compositional profiles in the top layer of cells; orange line—wire indenter, blue line—spherical indenter. As noted earlier, the spherical indenter LKMC simulation results represent an xz -slice taken from a three-dimensional domain, while the wire indenter simulations are two-dimensional. ... 83

Figure 4.12. Ge concentration profiles (a,b) in an initially uniform $Si_{0.8}Ge_{0.2}$ film following 3 hours of thermal annealing at 1000 °C under stresses (c,d) induced by contact with an 80 nm-diameter wire indenter (maximum contact pressure 18 GPa) with inter-wire spacing of (a,c) 105 nm, and (b,d) 210 nm. (e) Compositional profiles in the top layer of cells; orange line—105 nm pitch, blue line—210 nm pitch. 85

Figure 4.13. (a)-(d) Sequence of snapshots of Ge concentration fields in SiGe film during annealing at 1000 °C under a spherical indenter of diameter 80 nm and maximum contact pressure 21 GPa, (e) Ge concentration profile in top layer of LKMC cells after 0s (grey), 14s (blue), 74s (orange), 1 hour (pink) and 3 hours (red). 88

Figure 4.14. (a) Ge concentration in the top layer of LKMC cells in an initially uniform $Si_{0.8}Ge_{0.2}$ film following annealing for variable times under the action of a 80 nm-diameter wire indenter (maximum contact pressures 18 GPa). Annealing times are 30 min at 1050°C (pink), 180 min at 1000°C (blue), 700 min at 950°C, and 3300 min at 900°C. (b) Arrhenius plot of annealing time to reach set patterning extent versus inverse temperature; circles are simulation data, dashed line is the Arrhenius fit. 89

Figure 5.1. (a) Standard deviation of Ge concentration in uniform 20% Ge film with no externally applied stress field. (b) Top cell concentration profile of Ge concentration fields in SiGe film during annealing at 1000 °C under a spherical indenter of diameter 80

nm and maximum contact pressure 21 GPa (See Chapter 4). Green is net event LKMC and red is full LKMC.....	96
Figure 5.2. (a) schematic of changing entirely high resolution region of LKMC domain to variable resolution (b) schematic of exchanges between regions comprised of two different cell sizes (c) schematic of exchanges between equally size cells (d) sample LKMC grid. See text for details.....	98
Figure 5.3. Example mesh and geometry used to solve stress problems in this Chapter.	100
Figure 5.4. Meshes used in mesh refinement study (left), along with σ_{zz} in xy -plane at top substrate surface in z (right) for (a) coarsest mesh (b) intermediate mesh (c) finest mesh.	103
Figure 5.5. (a) Composition and (b) standard deviation in top layer of LKMC cells after 3 hours of annealing at 1000 °C after solving stress problem using mesh in Figure 5.4(a) (red), mesh in Figure 5.4(b) (blue), mesh in Figure 5.4(c) (green).....	104
Figure 5.6. (a) Sample indenter geometries, ranging from a spherical cap (radius of curvature of cap (R_{cap}) = indenter radius (R)) to an indenter with $R_{cap} \gg R$ (b) Two indenters separated by pitch, p	106
Figure 5.7. Compositional profiles after thermal annealing of a $Si_{0.8}Ge_{0.2}$ substrate under the action using a spherical indenter tip measuring (in R_{cap} and R) (a) 25 nm (b) 100 nm (c) 125 nm (d) 150 nm (e) 175 nm (f) 200 nm, at a cubic p of 210.3 nm.....	108
Figure 5.8. Compositional (a-b) and stress (c-d) profiles after thermal annealing of a $Si_{0.8}Ge_{0.2}$ substrate at 1000 °C using a spherical indenter tip with $R_{cap} = R = 125$ nm at a cubic p of (a,c) 105.2 nm (b,d) 210.3 nm.	110
Figure 5.9. Compositional (a-b) and stress (c-d) profiles after thermal annealing of a $Si_{0.8}Ge_{0.2}$ substrate at 1000 °C using a spherical indenter tip with $R_{cap} = R = 125$ nm at a p of 210.3 nm with an (a,c) cubic indenter array (b,d) hexagonal indenter array.....	111
Figure 5.10. Stress field during thermal annealing of a $Si_{0.8}Ge_{0.2}$ substrate under the action of an indenter with $R = 125$ nm at a cubic p of 210.3 nm for 3 hours at 1000 °C for (a) $R_{cap} = 125$ nm (b) $R_{cap} = 500$ nm (c) $R_{cap} = 1000$ nm (d) $R_{cap} = 2000$ nm.	113
Figure 5.11. Compositional profile after thermal annealing of a $Si_{0.8}Ge_{0.2}$ substrate under the action an indenter with $R = 125$ nm at a cubic p of 210.3 nm for 3 hours at 1000 °C for (a) $R_{cap} = 125$ nm (b) $R_{cap} = 500$ nm (c) $R_{cap} = 1000$ nm (d) $R_{cap} = 2000$ nm.....	114
Figure 5.12. Stress field (a) and compositional profile (b) in yz -plane at $x = 210.3$ nm for (top) $R_{cap} = 1000$ nm (bottom) $R_{cap} = 2000$ nm after thermal annealing of a $Si_{0.8}Ge_{0.2}$ substrate under the action of an indenter with $R = 125$ nm at a cubic p of 210.3 nm.....	115

Figure 5.13. Compositional profiles after thermal annealing of a $\text{Si}_{1-x}\text{Ge}_x$ substrate under the action of a spherical indenter tip with $R_{cap} = R = 125$ nm at a cubic p of 210.3 nm, with the substrate compositions of (a) 20% Ge (b) 40% Ge (c) 60% Ge (d) 80% Ge. .. 116

Figure 5.14. (a) Stress before (left) and after (right) rotation of cylindrical indenter after 3 hours of thermal annealing of a $\text{Si}_{0.8}\text{Ge}_{0.2}$ substrate annealed at 1000 °C (b) compositional profile at time of rotation. 118

Figure 5.15. Compositional profiles after rotating indenter field and continuing the thermal anneal at 1000 °C for (a) 1 minute (b) 10 minutes (c) 1 hour (d) 3 hours. 119

Figure 6.1. (a) Film dimension changes upon formation of vacancy (b) Film dimension changes upon formation of interstitial (c) Film dimension changes upon migration of vacancy (d) Film dimension changes upon migration of interstitial. See text for details 125

Figure 6.2. $tr(\mathbf{V}^f) = V^r \pm \Omega$ (positive for vacancies) for (a) Si vacancies and (b) Si interstitials. Red = T3, yellow = EDIP, green = SW, light blue = T-EA, dark blue = MEAM, black dashed line = average of literature values, black solid line = fit to data from ref. [78]. 136

Figure 6.3. $tr(\mathbf{V}^m)$ for (a) vacancies and (b) interstitials. Red = T3 (Si), yellow = EDIP, green = SW, light blue = T-EA, dark blue = MEAM, purple = T3 (Ge). 142

Figure 6.4. $d(tr(\mathbf{V}^m))/dT$ for (a) vacancies and (b) interstitials. Red = T3 (Si), yellow = EDIP, green = SW, light blue = T-EA, purple = T3 (Ge). 144

Figure 6.5. Values of $DC(P)/DC(0)$ under hydrostatic stress for (a) vacancies and (b) interstitials, for silicon and germanium as computed in this work. Red = T3(Si), purple = T3(Ge), yellow = EDIP, green = SW, light blue = T-EA, dark blue = MEAM. Diffusion is isotropic under hydrostatic stress [32]. 147

Figure 6.6. Values of $DC_{001}(\boldsymbol{\sigma})/DC(\mathbf{0})$ under biaxial stress, $\sigma_{11} = \sigma_{22} = \sigma, \sigma_{33} = 0$, for (a) vacancies and (b) interstitials, and values of $DC_{100}(\boldsymbol{\sigma})/DC(\mathbf{0}) = DC_{010}(\boldsymbol{\sigma})/DC(\mathbf{0})$ for (c) vacancies and (d) interstitials, for Si and Ge as computed in this work. Red = T3(Si), purple = T3(Ge), yellow = EDIP, green = SW, light blue = T-EA, dark blue = MEAM. 148

Figure 6.7. Values of $DC_{001}(\boldsymbol{\sigma})/DC(\mathbf{0})$ under uniaxial stress, $\sigma_{33} = \sigma, \sigma_{11} = \sigma_{22} = 0$, for (a) vacancies and (b) interstitials, and values of $DC_{100}(\boldsymbol{\sigma})/DC(\mathbf{0}) = DC_{010}(\boldsymbol{\sigma})/DC(\mathbf{0})$ for (c) vacancies and (d) interstitials, for Si and Ge as computed in this work. Red = T3(Si), purple is T3(Ge), yellow = EDIP, green = SW, light blue = T-EA, dark blue = MEAM. 149

Figure 7.1. Residual hydrostatic stress components along the top layer of LKMC cells following removal of the indenter for the 80 nm-diameter wire indenter (maximum

contact pressure of 18 GPa) and annealed at 1000 °C in Chapter 4: red line – σ_{zz} , blue line – σ_{xx} , and green line – σ_{yy} 156

Chapter 1. Introduction

At the heart of all electronic and optoelectronic devices fabricated on semiconductor substrates are abrupt compositional transitions. Such transitions may be the result of the joining of two dissimilar materials [1], the growth of one material onto a substrate of another [2], or be created in a single material that is compositionally altered in a spatially varying manner. An example of the latter case is the ubiquitous silicon p - n junction which is formed by doping adjacent regions in a pure silicon wafer with electron-deficient (e.g., boron) and electron-rich (e.g., arsenic) chemical species [3].

The creation of compositional transitions at very small length scales may be regarded as the essential goal of conventional microelectronic device processing. Here, lithographic patterning, in which a masking material is used to create highly structured apertures for introducing dopants [4], is combined with some means of introducing the various dopant species into the semiconductor substrate, typically by diffusion [5] or ion implantation [6] followed by thermal annealing. This sequence of steps is often combined with deposition of multiple layers of material on the base substrate in order to build increasingly complex structures [7]. This overall strategy is a classic example of so-called ‘top-down’ processing whereby the device features are built using (lithographic) patterns at the same scale as the features.

The robustness of this approach in the face of continuously shrinking device feature lengths, as originally predicted by Gordon Moore [8], has been truly remarkable—as shown in Figure 1.1, today's devices are fabricated with features approaching just a few nanometers. While the end of Moore's law scaling has been

prematurely predicted for a number of years, it is inevitable that the current materials and/or approaches to semiconductor device fabrication will have to evolve. In this regard, much research emphasis has been placed on the notion of ‘bottom-up’ fabrication, whereby spontaneous self-organization or self-assembly is driven and guided to produce structures that are otherwise inaccessible with traditional top-down techniques. The realization of this goal will not only extend the life of Moore’s law scaling, but is expected to make feasible the fabrication of a host of new electronic and optoelectronic devices.

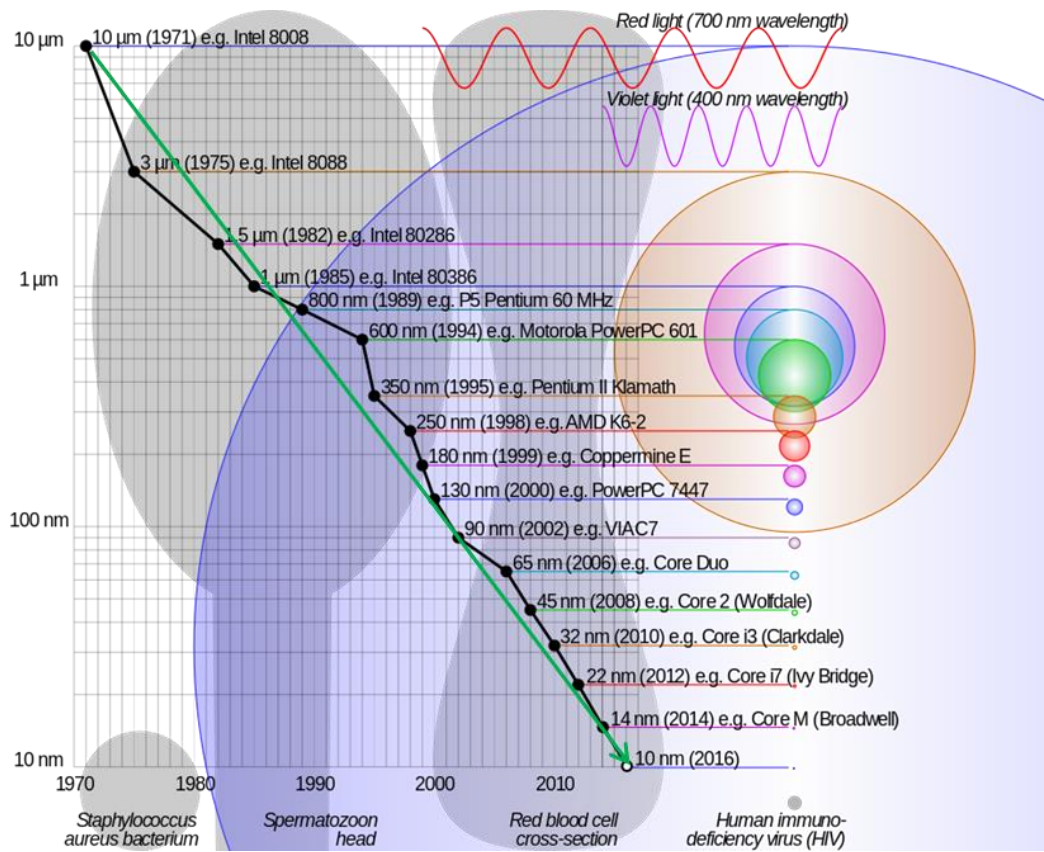


Figure 1.1. Shrinking of computer chip length scales with time. Perfect exponential shrinking law, as predicted by Moore, is shown with green line. Adapted from ref. [9].

A well-studied example of this type of process is the spontaneous formation of well-defined, three-dimensional islands observed during heteroepitaxial deposition (by any technique, such as molecular beam epitaxy (MBE), chemical vapor deposition (CVD), or physical vapor deposition (PVD)) of structurally similar, but lattice mismatched materials, such as semiconductors (e.g., Ge on Si or InAs on GaAs) and metals (e.g., Au on Ag). Generally, the atomistic details of the heteroepitaxial deposition process are strongly influenced by the degree of lattice mismatch, which creates misfit strain and increases the energy of the system. At low levels of mismatch, the deposited adatoms fully wet the surface and lead to layer-by-layer, or Frank van der Merwe, growth (Figure 1.2(a)); an example of this type of growth is observed in the Ag/Au heterosystem. At high degrees of mismatch, no wetting is possible and the deposited species immediately forms three-dimensional islands directly on the substrate with a very wide size distribution; this is the so-called Volmer-Weber growth mode (Figure 1.2(b)). In between these extremes, at moderate levels of lattice mismatch, a wetting layer is formed, upon which further deposition leads to the formation of three-dimensional islands with relatively good size and spatial distribution uniformity—this is known as the Stranski-Krastanov (SK) growth mode (Figure 1.2(c)). It has been observed and studied in a variety of semiconductor heterosystems including InAs/GaAs and Ge/Si (Figure 1.3).

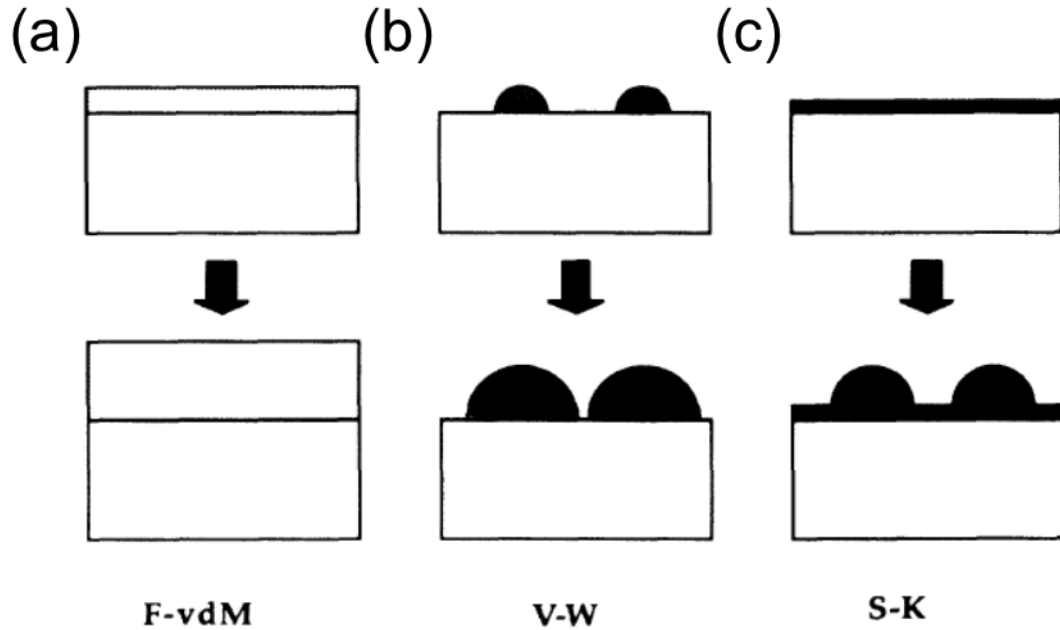


Figure 1.2. Schematic representation of three epitaxial growth pathways, starting from one monolayer of coverage to increasing coverage. Taken from ref. [10].

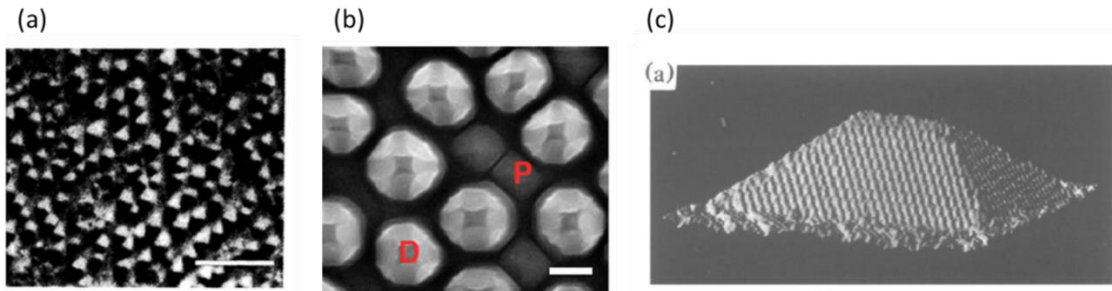


Figure 1.3. (a) InAs dots on GaAs (scale 100 nm). Taken from ref. [11] (b) Pyramid/hut (P) and dome (D) nanoclusters of Ge/Si (30% Ge) on Si (scale ~10 nm). Taken from ref. [12] (c) Ge hut cluster on Si (scan area is 40 nm \times 40 nm and island height is 2.8nm). Taken from ref. [13].

Scientific interest in the semiconductor islands formed by SK heteroepitaxial growth stems from their potential use as three-dimensionally quantum confined structures. Generally, quantum confinement occurs as the length scale of a bulk semiconductor material is reduced to the nanoscale. Here, the band gap of the material,

which determines the available electron energy states, is altered such that electrons can only occupy certain energy levels, restricting the energetic density of states (See Figure 1.4). The restriction increases as the dimensionality of confinement increases: quantum wells (Figure 1.4(b)) exhibit one dimension of confinement, quantum wires (Figure 1.4 (c)) exhibit two dimensions of confinement, and quantum dots (Figure 1.4(d)), exhibit confinement in all three dimensions. While confinement in each dimension leads to some discretization of the bulk material density-of-states, three-dimensional confinement is particularly exciting because the electronic density of states of QDs are fully discrete and open up the possibility for creating devices with new capabilities, such as quantum encryption and quantum computing [14-17]. Although a robust way to produce large arrays of highly uniform and addressable quantum dots has not yet been demonstrated, quantum wells are in routine use in a variety of optoelectronic devices such as lasers [18], infrared photodetectors [19], and solar cells [20]. This is because while, it is quite straightforward to modulate the composition of deposited layers in the direction of growth to produce a sequence of thin layers of material with differing electronic band structures, it is much more difficult to achieve this modulation in the lateral directions (perpendicular to the growth direction).

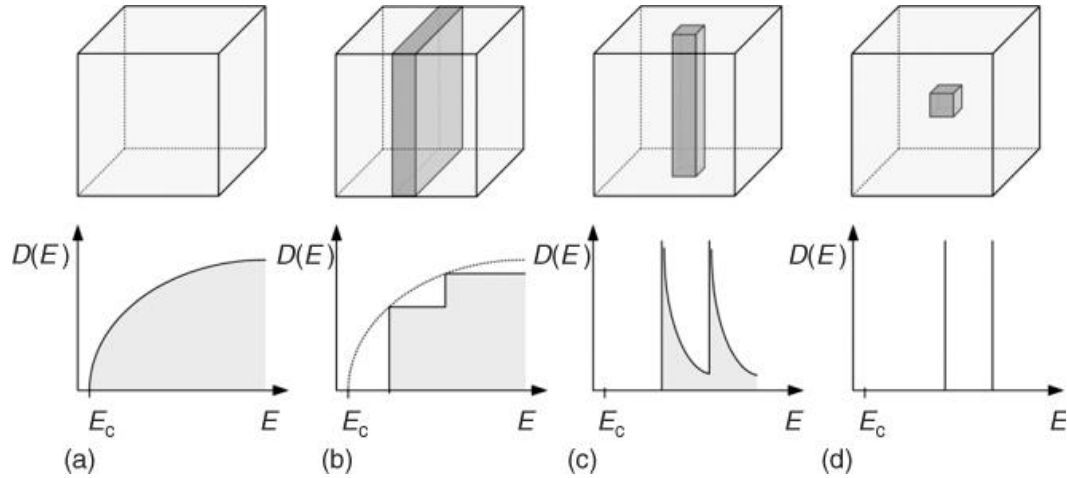


Figure 1.4. (a) Bulk material with no quantum confinement and a continuous density of energy states (b) Quantum well, a material with one-dimensional quantum confinement, and a reduced energy density of states (c) Quantum wire, a material with two-dimensional quantum confinement, and a further reduced energy density of states (d) Quantum dot (QD), or three dimensionally quantum confined material, with delta function for energy density of states. Taken from ref. [21].

The fundamental challenge of creating highly uniform arrays of QDs on semiconductor substrates has attracted a large amount of attention. In general, approaches to increase size and spatial uniformity have been aimed at overcoming the inherently random or stochastic nature of island nucleation by pre patterning the surface in some manner to create preferential island nucleation sites. Selected examples are shown in Figure 1.5. In (a), it is observed that an $\text{Si}_{1-x}\text{Ge}_x$ layer grown on Si roughens, leading to undulations in the adlayer, due to the Asaro-Tiller-Grinfeld (ATG) instability in the system [22]. The ATG instability arises from a competition between surface energy and elastic (mismatch) energy. Ge atoms in $\text{Si}_{1-x}\text{Ge}_x$ migrate toward the peaks of the undulations to reside in regions with a lattice parameter closest resembling $\text{Si}_{1-x}\text{Ge}_x$ [22]. If Si is deposited on top of the $\text{Si}_{1-x}\text{Ge}_x$ layer, followed by another layer of $\text{Si}_{1-x}\text{Ge}_x$, correlation is observed between the positioning of undulations (see, e.g., Figure 1.5(a)).

These “stacked” undulations are seen to guide the nucleation of Ge SK growth on the surface of the superlattice (e.g., Figure 1.5(b)). A second approach to directing Ge SK growth deposited Ge on a Si surface that contained steps, as islands are seen to preferentially nucleate at the step locations [22]. In one example of this approach, miscut Si (001) is used as a substrate [23]. A Si buffer layer is then grown on the substrate, leading to a faceted surface with different orientations ((001) and (11 x), $x=8-10$), with the (001) facets being the preferred island nucleation location. Subsequent deposition of Ge leads to dots nucleating in an ordered fashion (Figure 1.5(c)).

Another study employed surface “pits” generated in the substrate, which serve as preferential nucleation sites [24]. Here, a two dimensional array of holes in a (001) Si substrate was created via lithography and reactive ion etching, followed by a buffer layer of Si. Upon deposition, Ge islands are seen to nucleate in a two-dimensionally ordered manner (Figure 1.5(d)). A second lithographic surface pre patterning approach [25] (Figure 1.5(e)) used patterned lines of oxide on Si (001) as a substrate. In this case, Ge islands were observed to nucleate preferentially in alignment with the Si stripes.

Finally, altering the surface chemistry of the substrate can yield desirable control over the dot formation process. One study used Ga ion implantation into an Si(100) surface to create preferential nucleation sites for Ge island nucleation [26]. The subsequently nucleated dots are seen to be very well ordered (Figure 1.5(f)).

These surface pre patterning approaches are all at least somewhat successful at achieving spatial and size uniformity of islands formed during SK growth. However, it is important to note that nucleation, in general, is very difficult to modulate because it is

usually a strongly driven process, making near-perfect uniformity in island size and distribution virtually impossible to achieve. In addition, given the strong driving force toward nucleation, annealing away undesirable surface features is also very difficult.

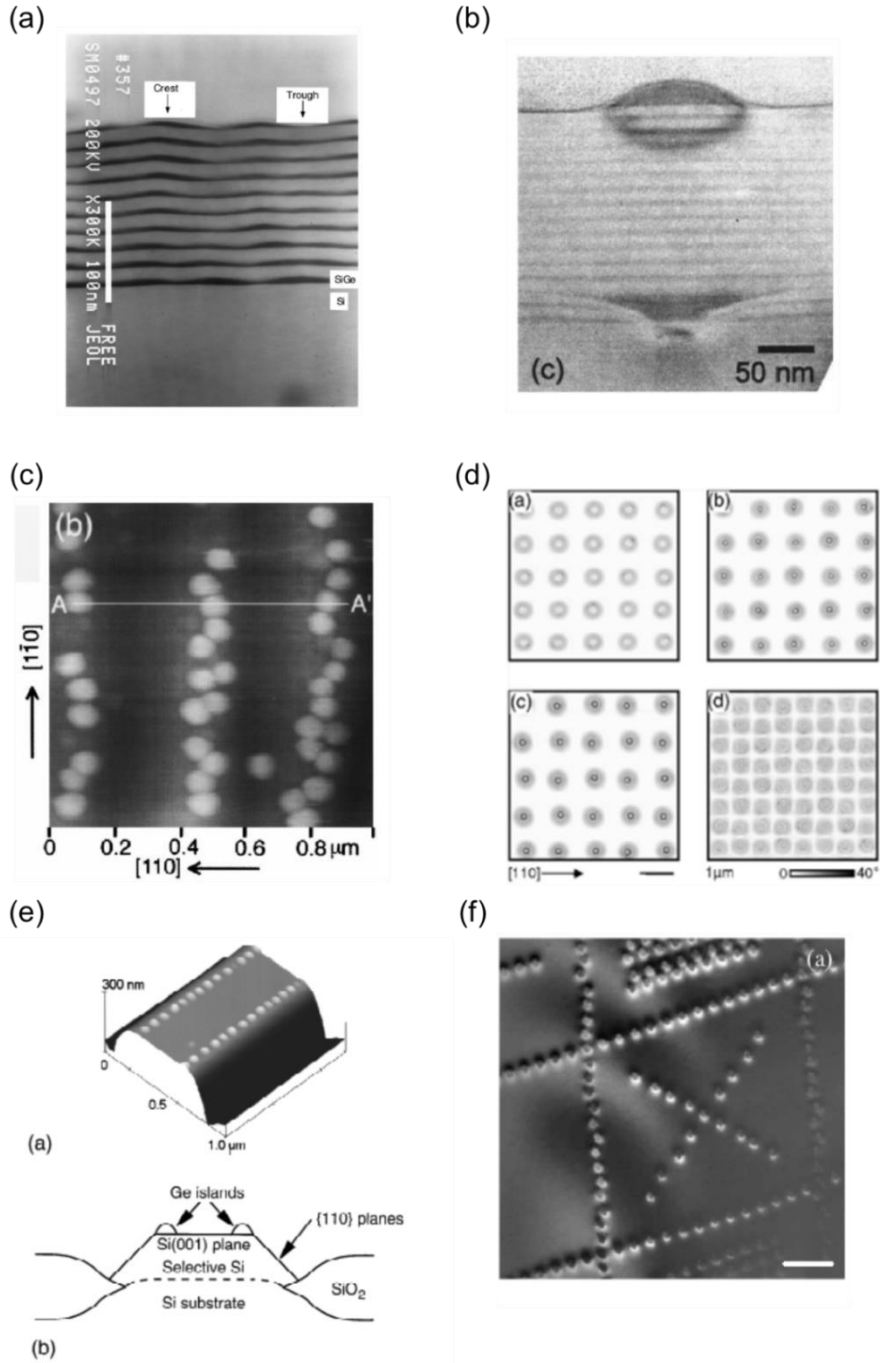


Figure 1.5. (a) $\text{Si}_{0.50}\text{Ge}_{0.50}/\text{Si}$ superlattice with ATG undulations. Taken from ref. [27] (b) Ge dots aligning with undulations in Si/SiGe superlattice. Taken from ref. [28] (c) Bright Ge islands grown on vicinal Si (001). Taken from ref. [23] (d) Lithography/RIE (Reactive Ion Etching)-created pits lead to patterned Ge dots. Taken from ref. [24] (e) Atomic Force Microscopy scan and schematic of Ge dots on Si surface with patterned oxide. Taken from ref. [25] (f) Patterned Ga ion implanted seen to guide nucleation sites for Ge islands on Si. Taken from ref. [26].

1.1 Surface Stress Mediated Patterning of Compositional Rearrangement

As discussed in the preceding section, the numerous experimental studies aimed at controlling Stranski-Krastanov growth of discrete islands on a semiconductor surface are limited by the highly driven nature of nucleation during the island formation process. A novel variation on the general theme of stress-mediated compositional evolution to form structures with potential quantum confinement properties was demonstrated in a pioneering study by Hung and co-workers [29]. Here, a GaAs-based multilayer structure was grown via MBE, in which a thin layer of GaAs containing an excess of As atoms was sandwiched between two AlGaAs layers (see Figure 1.6(a)). Stripes of InGaAs were then lithographically patterned onto the heterostructure. Since InGaAs has a larger lattice constant than GaAs (7.1% larger for InAs), localized stress fields were generated within the sandwiched GaAs layer. Upon annealing, precipitates were found first to nucleate homogeneously within the sandwiched GaAs layer, but eventually coarsened preferentially in regions below the stressor stripes (Figure 1.6(b)). Moreover, the size distribution of the ordered precipitates was found to be reasonably narrow. These observations are consistent with nature of the nucleation process, discussed in the preceding section, along with the weaker driving conditions governing the growth and coarsening processes that are more amenable to the influence of the patterned stress field [30, 31].

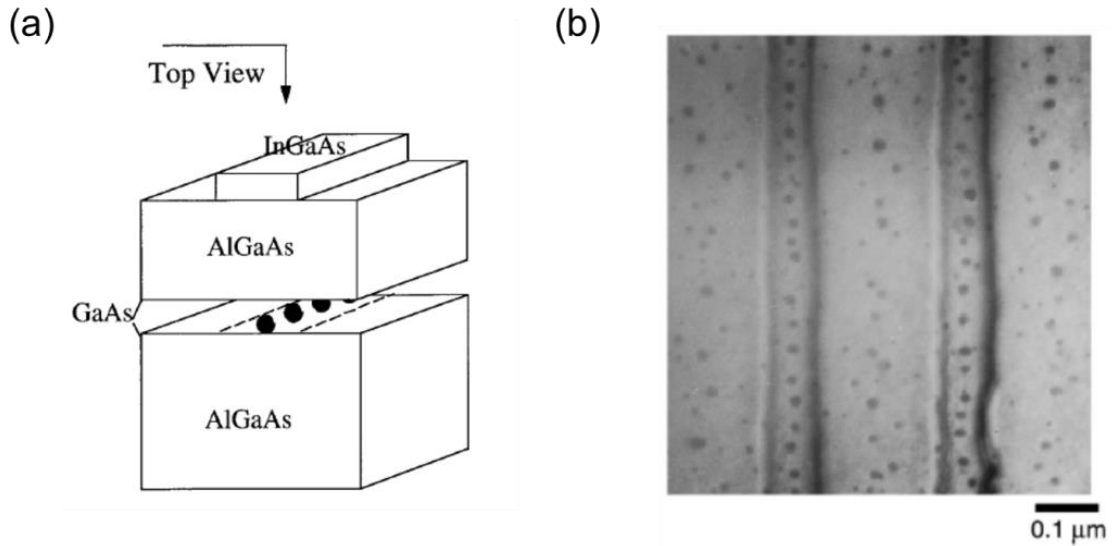


Figure 1.6. (a) Schematic of InGaAs lines on the surface of the AlGaAs/GaAs heterostructure (b) Plan view transmission electron microscopy micrograph of an array of As particles below stressor lines. Taken from ref. [29].

In this thesis, I computationally assess a new robust methodology to generate Ge QCSs in SiGe, schematically illustrated in Figure 1.7. The approach involves subjecting a uniform SiGe wafer, at relatively high temperature, to a spatially variable stress field generated by indentation on the film surface (Figure 1.7(b)). Upon annealing, the larger Ge atoms preferentially diffuse away from areas of high compression, leaving behind regions of enhanced Si in the previously compressed patch (Figure 1.7(c)). Regions of variable composition created by this procedure can serve as QCSs. Given that no precipitates are nucleated in this approach, we hope to avoid many of the limitations associated with previous demonstrations. To enable near-perfect scalability of the procedure proposed here, we perform indentation using a reusable, albeit costly to lithographically manufacture, indenter template. As far as residual surface modifications due to the indentation, it will be demonstrated that the required stresses to cause

patterning are seen to be well within the elastic regime, which will lead to substrates containing a minimal amount of surface damage.

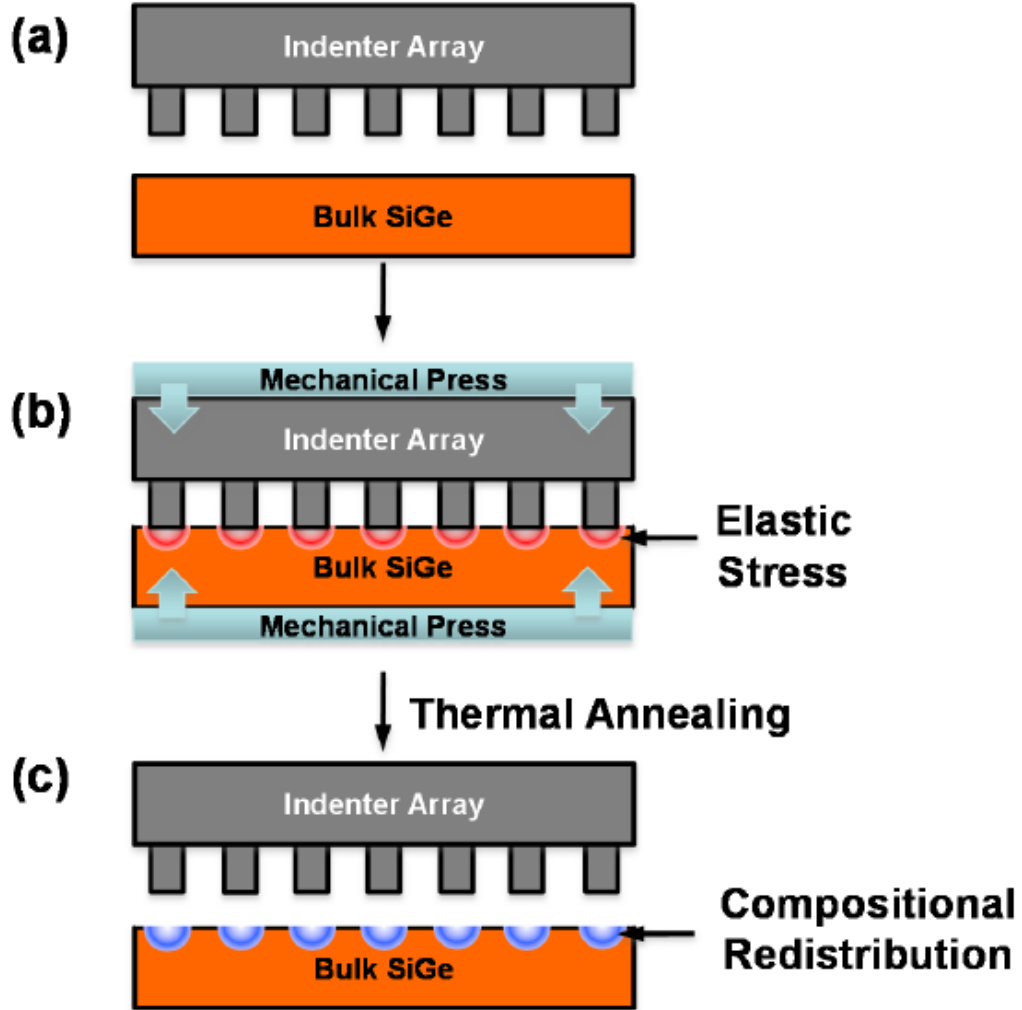


Figure 1.7. A nanopillar template is applied to a SiGe wafer (a,b). During annealing, larger Ge atoms preferentially diffuse away from areas of compression, creating patches of enhanced Si content (c).

The remainder of the thesis is structured as follows. Chapter 2 provides experimental evidence of the viability of the approach, along with pertinent details regarding the experimental setup and characterization techniques used to analyze the

results. Chapter 3 provides a discussion of the fundamental modeling challenges associated with interdiffusion in the SiGe system and describes the most common modeling alternatives used to address related problems. In Chapter 4, a coarse-grained lattice kinetic Monte Carlo model is introduced and discussed in detail; this model serves as the basis for all the validation and prediction studies carried out in this thesis. The simulator, which is based on a similar model used to describe interdiffusion in biaxially strained SiGe films, is parameterized using a large database obtained from numerous literature studies, both experimental and computational. Chapter 4 also includes a discussion of the impact of indentation strength and indenter size. Connections to the experimental results discussed in Chapter 2 also are presented here.

Next, in Chapter 5, a detailed parametric analysis is presented of indenter geometry, pitch, and annealing schedule, along with substrate composition, to determine how to best generate compositional patterns that are consistent with quantum confinement and therefore of greatest technological relevance. While many of the parameters related to interdiffusion in SiGe are well-known (e.g., point defect diffusivity in unstressed material as a function of temperature), the impact of stress on diffusion is not well established at a quantitative level in the literature—this is perhaps the chief modeling uncertainty in the results presented in Chapters 4 and 5. In Chapter 6, a comprehensive analysis is presented of point defect diffusion under variable stress. In particular, molecular dynamics simulations are used to estimate the so-called activation volumes [32] for point defects using several popular empirical potentials. Finally, in Chapter 7 conclusions are presented and some directions are proposed for future work related to this nascent technology. In particular, work is proposed that could be used to

further optimize and extend the stress-patterning approach with the ultimate aim of producing substrates with ordered arrays of uniform and addressable quantum structures.

Chapter 2. Demonstration of Stress-Directed Patterning in SiGe

2.1 Introduction

In this chapter, experimental verification of a new approach for creating microscale compositional patterns in an SiGe wafer is presented. This work was performed at the University of New Mexico by the experimental research group of Professor Sang Han [33]. As briefly outlined in Chapter 1, a Si nanopillar indenter array was used to apply a spatially patterned mechanical load onto the surface of a Si_{0.8}Ge_{0.2} wafer and then the assembly was subjected to thermal annealing. As a result, the larger Ge atoms migrated away from areas of compressive stress, leaving well-defined, Si-enriched areas surrounded by bulk SiGe. The approach is depicted in Figure 2.1. The various components of the experimental assembly are shown in Figure 2.1(a). A 2D array of Si nanopillars (Figure 2.1(b)) and the SiGe substrate were pressed against each other in a mechanical press consisting of top and bottom molybdenum (Mo) plates held together with 10 tungsten(W)-coated stainless steel screws. Each pillar was 80 nm in diameter and placed at a 200 nm pitch. The individual steps in the stress transfer process are shown in Figure 2.1(c). A torque of 2-20 N-m was applied to each screw. The total applied force (F) was related to the applied torque (T) according to [34]

$$F = T \frac{N_s}{CD}, \quad (2.1)$$

where $N_s = 10$, $C = 0.2$, and $D = 0.00417$ m represent number of screws, torque coefficient [35], and nominal screw diameter, respectively. The maximum contact pressure, approximately 20-45 GPa, was computed via a Hertzian contact analysis [36]

between a spherical indenter top and a film plane. Details on the Hertzian contact model are discussed in Chapter 4.

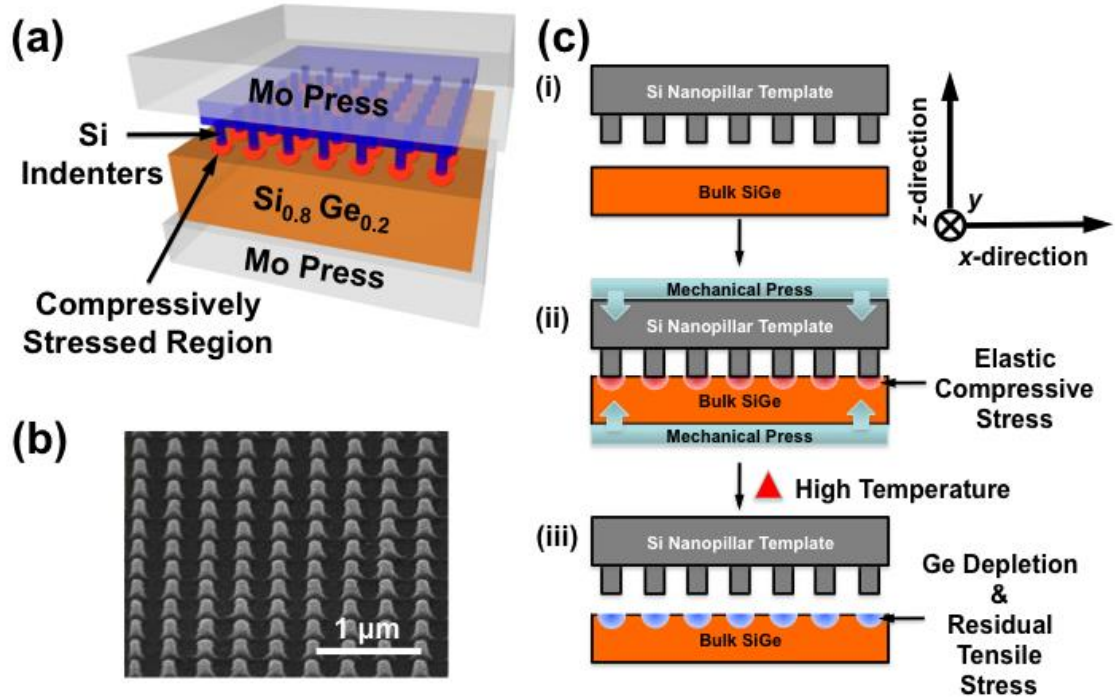


Figure 2.1. (a) Schematic representation of assembly used to create patterned stress fields in a SiGe substrate. (b) SEM image of Si nanopillar array used to apply a patterned stress field to the SiGe substrate. (c) Steps in the stress transfer process: (i) place Si nanopillar indenter array on top of SiGe substrate, (ii) press the indenters against the substrate, and (iii) thermally anneal the stack under patterned stress field.

Following the application of stress, the entire assembly was placed in a furnace at elevated temperatures (900-1000 °C) for 3 hours to allow sufficient time for Ge atoms to diffuse. After annealing, the furnace was brought to room temperature, and the mechanical assembly was retrieved from the furnace and disassembled. The annealed SiGe substrate was imaged, using scanning electron microscopy (SEM). The SEM

images were used to identify any material transfer from the Si indenters to the SiGe substrate and any permanent plastic deformation. The SiGe substrate surface was further characterized, using cross-sectional and scanning tunneling electron microscopy (XTEM and STEM) to assess in more detail the crystalline structure below the indented regions. Nano-probe energy dispersive spectroscopy (EDS) was also applied to map the compositional redistribution near the SiGe substrate surface.

2.2 Experimental Findings

Figure 2.2 shows SEM images of post-annealed $\text{Si}_{0.8}\text{Ge}_{0.2}$ substrates as a function of annealing temperature and maximum indenter contact pressure. Some of the SEM images reveal visible residual post-anneal features on the $\text{Si}_{0.8}\text{Ge}_{0.2}$ substrates; these are more prominent as the compressive stress and/or the temperature increases. Two different features are highlighted in Figure 2.2. The dotted circle ($T = 1000\text{ }^\circ\text{C}$, $P = 40\text{ GPa}$) highlights a piece of Si left over from one of the indenter pillars as the indenter array was separated from the $\text{Si}_{0.8}\text{Ge}_{0.2}$ substrate. The Si is likely to be evidence of bonding between the Si nanopillars and $\text{Si}_{0.8}\text{Ge}_{0.2}$ substrate. The solid circle ($T = 1000\text{ }^\circ\text{C}$, $P = 45\text{ GPa}$), by contrast, appears to show a permanently indented area and is evidence of plastic deformation within the $\text{Si}_{0.8}\text{Ge}_{0.2}$ substrate.

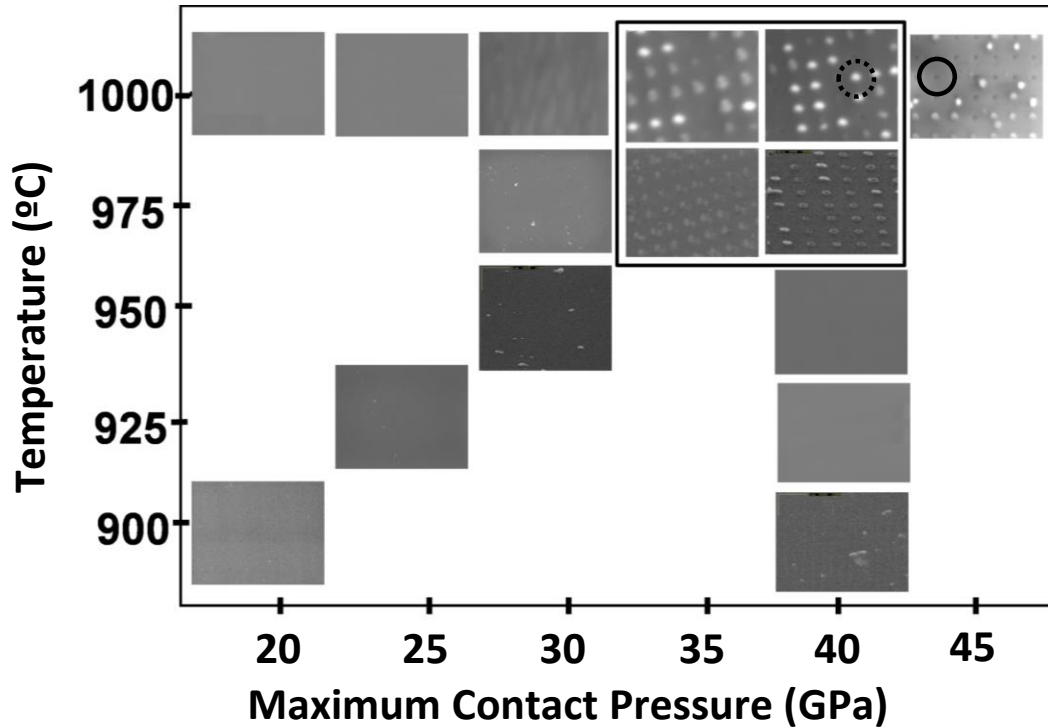


Figure 2.2. SEM images of $\text{Si}_{0.8}\text{Ge}_{0.2}$ substrates subjected to patterned stress fields and annealed for 3 hours, as a function of annealing temperature and maximum contact pressure. Each panel represents a region with dimension $1200 \text{ nm} \times 1200 \text{ nm}$.

A subset of the $\text{Si}_{0.8}\text{Ge}_{0.2}$ substrates was subjected to further analysis with XTEM and EDS. Three different maximum contact pressures for constant annealing temperature at $1000 \text{ }^\circ\text{C}$ were considered: $P = 35 \text{ GPa}$ [Figure 2.3(a)], $P = 45 \text{ GPa}$ [Figure 2.3(b)], and $P = 40 \text{ GPa}$ [Figure 2.3(c)]. For each case, EDS was used to sample a total of 45 uniformly spaced locations separated by 10 nm and sequentially denoted as (P1 to P45) [see left-side inset XTEM images for each case] to infer a compositional profile near the substrate surface. Each EDS measurement (P1 to P45) corresponded to a compositional average over a $3 \times 3 \times 3 \text{ nm}^3$ cuboidal region based on the electron beam diameter and probing depth of EDS. Note that the irregularly-shaped objects present on the surface of the substrate in each of the left-side XTEM insets (labeled as “indenter”) were identified

by EDS as being pure Si in composition, confirming that they were residual pieces of Si nanopillars that became bonded to the SiGe substrate. Fortuitously, these residual Si pieces were immensely useful as “markers” to precisely locate the regions where the compressive stress is applied. For this reason, the high-stress cases were selected for EDS analysis.

Case (a) in Figure 2.3 shows almost complete segregation of the larger Ge atoms away from the compressively stressed areas below two distinct nanopillar contact regions centered at locations P13 and P33. The width of the Ge-depleted regions is approximately 30 nm, although some Ge depletion is observed over a total distance of ~100 nm. No visible defects or dislocations are found underneath the indented regions [see right-side inset XTEM image of Figure 2.3(a)]. By contrast, the Ge segregation effect is almost entirely absent for case (b), which, unlike case (a), exhibits a high density of line defects up to a depth of about 30 nm from the surface [see right-side inset XTEM image of Figure 2.3(b)]. These results suggest that only elastic deformation can induce Ge diffusion and subsequent compositional variation, whereas plastic deformation actually inhibits it. The intermediate indentation case (c) further supports this hypothesis. Here, a low density of line defects (right-side inset) is shown to correspond to a microscopically complex segregation pattern in the regions immediately below the indenter contact areas. While it is very difficult to align the compositional fluctuations with specific microscopic defect features, the highly localized nature of Ge segregation below the indenter contact areas [e.g., note the absence of Ge depletion at P12 and P15, highlighted with rectangles in (c)] strongly suggests that the segregation effect is controlled by the local microstructure. The results in Figure 2.3(c) also highlight the fact that the EDS

measurements were able to resolve the compositional profile down to length scales of at least 10 nm.

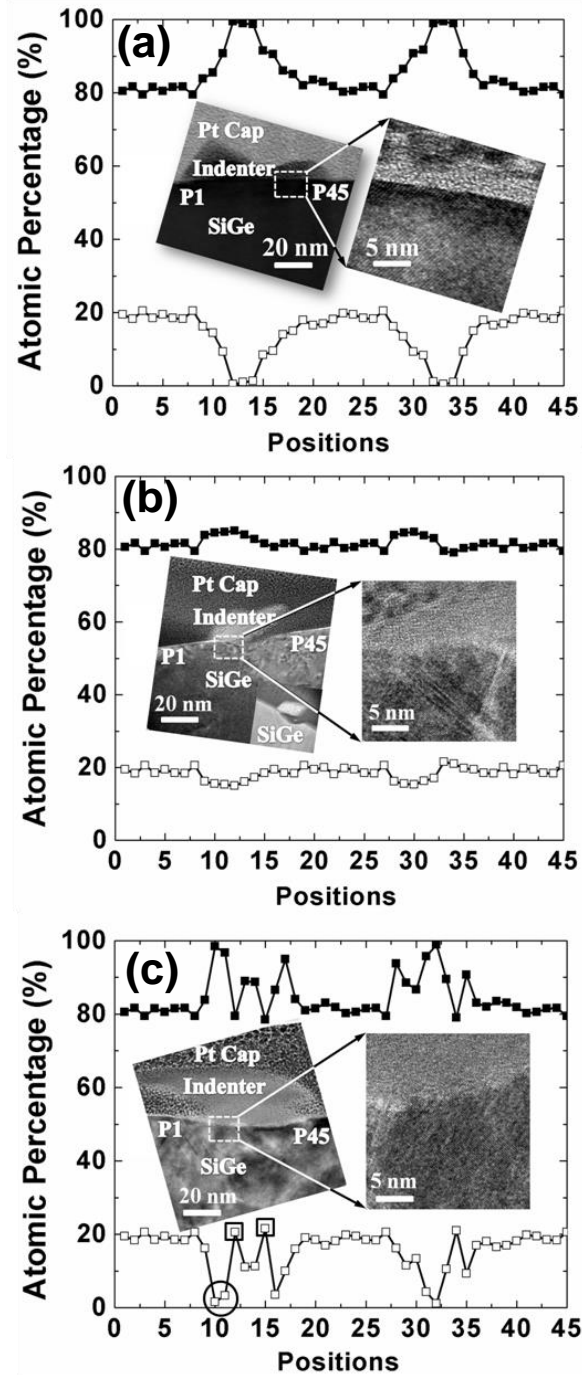


Figure 2.3. Atomic percentage of Si and Ge near the surface of indented SiGe substrate. Case (a): $T = 1000\text{ }^{\circ}\text{C}$, $P = 35\text{ GPa}$. Case (b): $T = 1000\text{ }^{\circ}\text{C}$, $P = 45\text{ GPa}$. Case (c): $T = 1000\text{ }^{\circ}\text{C}$, $P = 40\text{ GPa}$. Inset TEM images show (a) complete Ge depletion with elastic deformation, (b) no discernable compositional change with plastic deformation, and (c) intermediate case with highly localized Ge depletion.

While elastic compression is required to drive the segregation effect, the results in Figure 2.3 suggest that plastic deformation resulted in a near-complete relaxation of the local elastic compression presumably by creep. This hypothesis is supported by the permanent indentations observed on the substrate surface when both the temperature and applied pressure were high (Figure 2.2). However, additional mechanisms may be operational and cannot be ruled out. For example, line defects may locally impact the concentration of the point defect diffusion mediators for Si-Ge exchange (e.g., by acting as strong point defect sinks), thus inhibiting the stress-driven segregation process. Moreover, plastic deformation of the nanopillars may be responsible for the reduced elastic stress in the substrate during annealing. Note that for all cases considered here, both Si and $\text{Si}_{0.8}\text{Ge}_{0.2}$ were well above their brittle-to-ductile transition temperatures ($T_{BDT}^{\text{Si}} \sim 550^\circ\text{C}$ [37]) where dislocation mobility is high. There also is the possibility of surface melting; the low Ge concentrations used in this work suggest that surface melting was not a factor, although higher Ge concentration substrates will likely limit the annealing temperatures that can be applied.

2.3 Conclusions

In summary, we have described experiments examining a new approach for establishing sharp lateral compositional profiles in the near-surface region of SiGe substrates. Such profiles may provide useful building blocks for a new generation of devices that take advantage of lateral quantum confinement. The approach relies on a reusable indenter template to apply a patterned stress field to the surface of the SiGe substrate, driving Si-Ge exchange and subsequent compositional modulation.

While these preliminary experimental results clearly demonstrate the feasibility of mechano-patterning in the SiGe system, it will be difficult to evaluate and optimize the process because of the costs associated with electron microscopy and the need for visible surface features to locate the indentation sites. Consequently, a computational model is essential to fully analyze the compositional segregation process. In the next Chapter, I present an overview, with examples, of available computational tools.

Chapter 3. Review of Computational Approaches

Diffusion of Si and Ge atoms in bulk SiGe is entirely mediated by native point defects (namely vacancies (V) and interstitials (I)). Both types of defects may assume a variety of charge states, which will be addressed in the context of the model described in Chapter 4, but the overall diffusional mechanisms they mediate are independent of charge. Example point defect mediated diffusive processes are shown in Figure 3.1. In (a) and (b), Si and Ge lattice atoms hop into an adjacent empty site in the lattice (i.e., a vacancy), while the vacancy moves into the position previously occupied by the lattice atom. In (c) and (d), an atom between lattice sites (an interstitial), exchanges position with a lattice atom. In both cases, net motion of Si or Ge atoms has occurred; repetition of this process leads to long range diffusion.

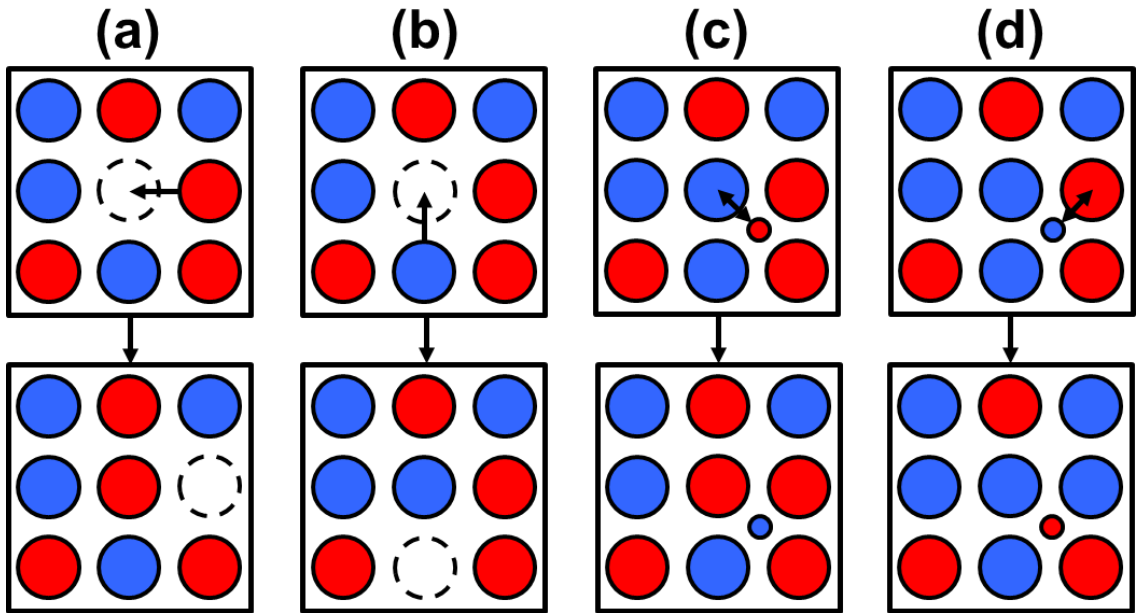


Figure 3.1. Schematic of defect mediated atomic diffusion. Red atoms represent Si and blue atoms represent Ge: (a) vacancy-enabled Si motion, (b) vacancy-enabled Ge motion, (c) Si interstitial ‘kicks out’ a Ge atom creating a Ge interstitial, and (d) a Ge interstitial kicks out an Si atom creating an Si interstitial.

Point defect equilibrium concentrations in Si and Ge are extremely low: For example, the concentration of neutral vacancies in Si is characterized by an Arrhenius relationship [38]

$$C_V = C_{0V} \exp\left(-\frac{E_{fV}}{kT}\right), \quad (3.1)$$

with $C_{0V} = 2.5 \times 10^{26} \text{ cm}^{-3}$ and $E_{fV} = 3.9 \text{ eV}$. Figure 3.2(a) shows the vacancy concentration over the range of annealing temperatures that are typical for the stress-mediated compositional patterning process considered here. The corresponding atomic fraction is in the range 10^{-11} - 10^{-14} (given an atomic density of $\sim 5 \times 10^{22} \text{ cm}^{-3}$ [38]). The diffusivities of point defects also are generally characterized by Arrhenius relationships. For instance, the diffusivity of neutral vacancies in Si is given as [38]

$$D_V = D_{0V} \exp\left(-\frac{E_{mV}}{kT}\right), \quad (3.2)$$

with $D_{0V} = 1 \times 10^{-3} \text{ cm}^2/\text{s}$ and $E_{mV} = 0.4 \text{ eV}$. Figure 3.2(b) shows these diffusivities over the same temperature range as shown for the equilibrium concentration. The product of concentration and diffusivity, or $D_V C_V$ in this case, is referred to as the transport capacity of a defect species and is a direct measure of the ability of a defect to move atoms. For neutral vacancies in Si, the transport capacity is shown in Figure 3.2(c) (based on the estimates in ref. [38]).

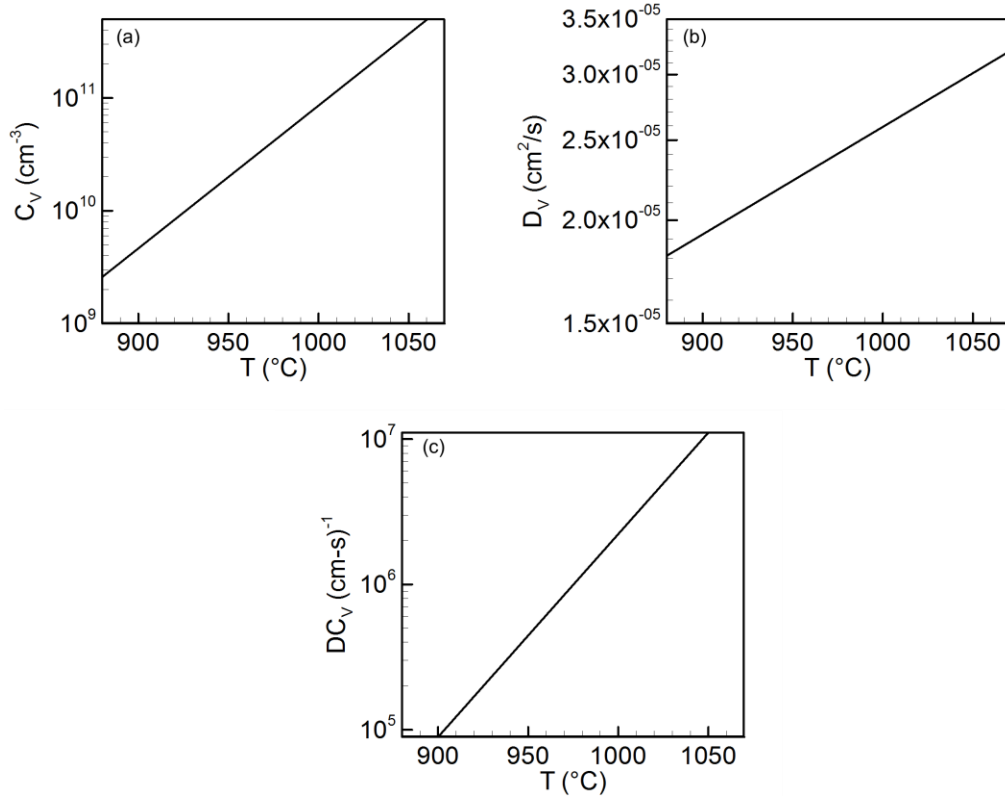


Figure 3.2. Concentration (a), diffusivity (b), and transport capacity (c) of neutral vacancies in silicon as a function of temperature.

The preceding considerations immediately lead to the conclusion that a direct molecular dynamics (MD) simulation of SiGe interdiffusion, especially over the length and timescales that are relevant to the stress transfer process described in Chapters 1 and 2, is simply infeasible. This is the case even if relatively efficient empirical potentials are employed to describe the interatomic interactions between silicon and germanium atoms.

Consequently, the appropriate simulation strategy must be based on some form of coarse-grained representation. Shown in Figure 3.3 is an example of a hierarchy of simulation representations beginning with quantum mechanical simulations (based on electronic density functional theory), to empirical potential-based atomistic simulations, to kinetic Monte Carlo (including both atomistically-resolved and coarse-grained

varieties), to continuum simulations (in this context, referring mainly to phase field simulations). In the ensuing discussion, we provide examples and brief introductions to these various simulation approaches.

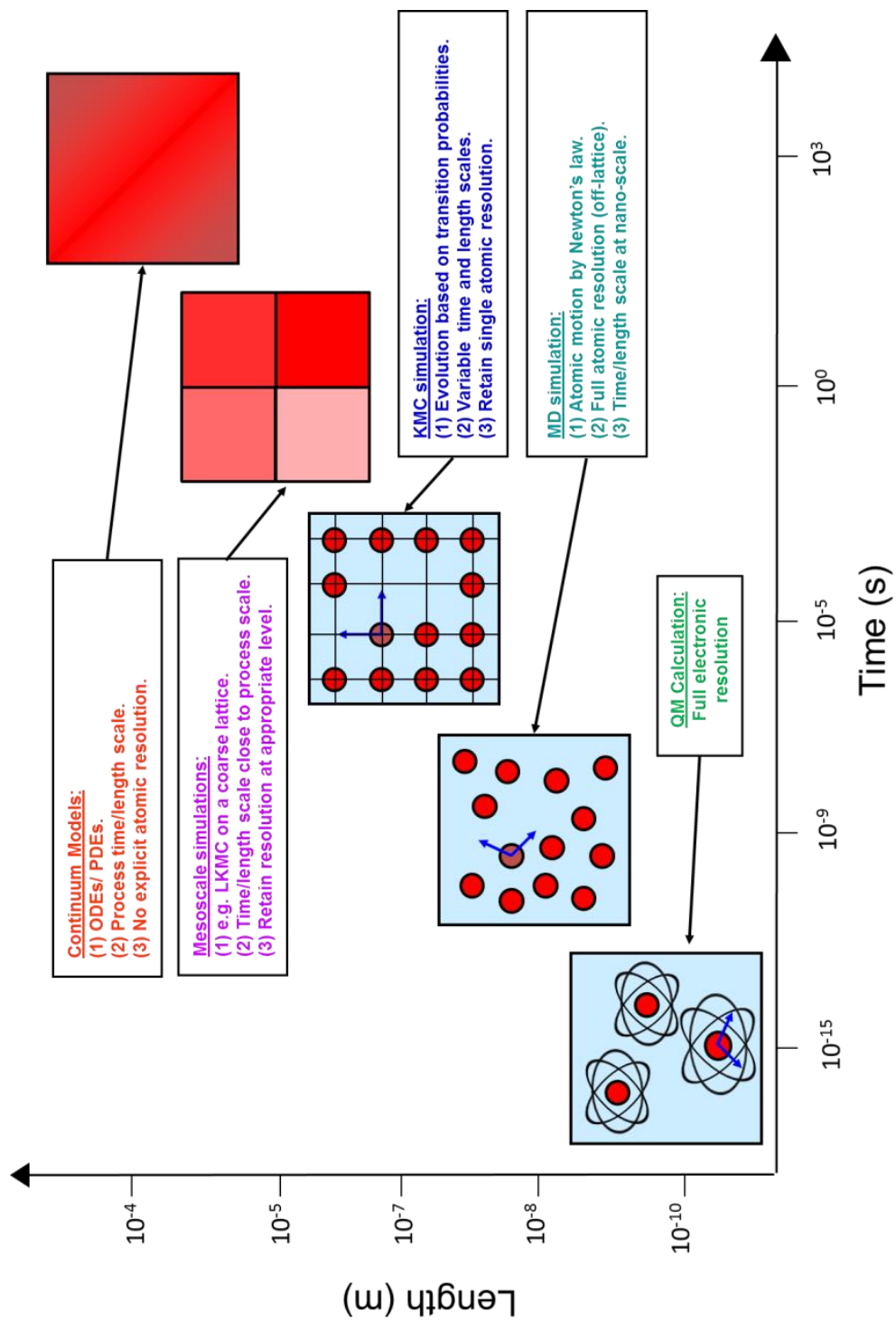


Figure 3.3. Schematic of different computational techniques and accessible length and time scales.

3.1 Metropolis Monte Carlo

Metropolis Monte Carlo (MMC) [39], while traditionally used to study systems at the same resolution as MD, was used by Nieves and co-workers in a model of diffusion under stress in which the individual point defect hops are coarse-grained, while an overall atomic level description of diffusion in an alloy is maintained [30, 31]. In this framework, a thin binary (*A-B*) film is created with imposed displacements in the *z*-direction to impose an external stress field on the film (see Figure 3.4(a)). In all cases, there is lattice misfit between *A* and *B* atoms, in order to drive compositional segregation. Compositional evolution in the film is performed using the MMC algorithm, with proposed moves comprised of nearest-neighbor atomic identity “switches,” in effect a compound move of many of the elementary steps depicted in Figure 3.1. However, the defects driving diffusion are implicitly accounted for in the simulation, thus increasing the scales achievable via ordinary MD. The studies performed include a range of potentials, from Lennard-Jones to MEAM, and all produce the same patterning behavior, from which it is concluded that these types of simulations could be applied to a wide variety of material systems, ranging from low to high misfit. The main physical limitation of this approach results from the move basis for system evolution; while there is qualitative progression of the compositional profile toward equilibrium (see Figure 3.4(b)), the dynamics of the process are not captured quantitatively. Given that there is no guarantee that an anneal procedure has reached equilibrium for a given protocol, this limits the predictive ability of the modeling proposed in this thesis. Computationally, this method is limited due to molecular static relaxations that must be performed to ensure

that accurate energies are used in the MMC acceptance criterion. The ability to only performing regionally local relaxations, does mitigate this limitation.

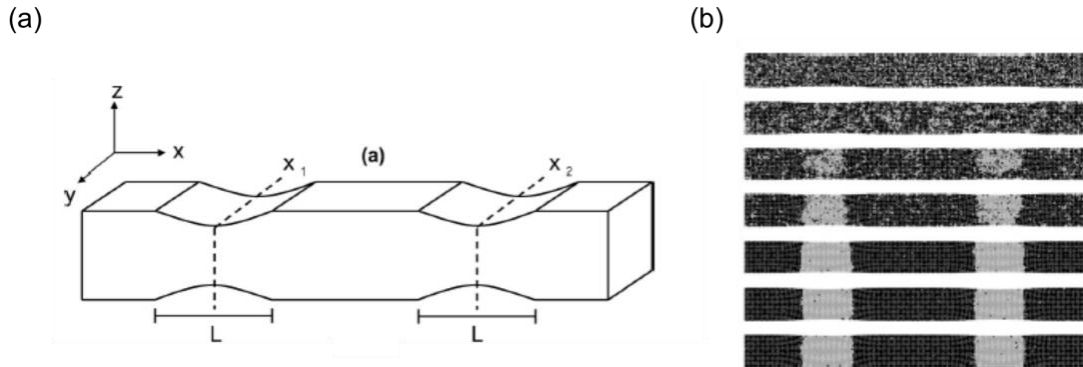


Figure 3.4. (a) Schematic of applied surface strain field to generate stresses in substrate (b) xz -cross section of film showing compositional evolution as a function of sweeps. Smaller B atoms (light gray) preferentially aggregate in regions of high stress. Taken from ref. [30].

3.2 Kinetic Monte Carlo Method

Kinetic Monte Carlo (KMC) (also known as dynamical Monte Carlo and in certain contexts also as the Gillespie method [40]) is a stochastic approach developed to model dynamics for systems that spend most of their time vibrating around potential energy minima, only occasionally overcoming the energy barrier between basins [41], creating a separation of time scales between vibrations and rare, basin-exiting events. For fully atomically resolved MD simulations of systems in which this time scale separation exists, e.g., for defects diffusing in a solid, one would integrate the equations of motion for a system of atoms, most of the computational resources would be spent in one potential energy minimum, and rarely, if ever, would a transition occur.

KMC assumes that due to the long time spent in one basin, a quasi-equilibrium is established as the system explores its current local energy minimum. In addition, all

events are assumed to be independent Poisson processes. Under these assumptions, the probability that the system remains in state i , is exponentially distributed [42]

$$p_{i \rightarrow j}(t) = \exp(-r_{ij}t), \quad (3.3)$$

where r_{ij} is the rate of leaving state i to go to state j . The average time to transition between transitions is $1/r_{ij}$. The total probability of the system remaining in state i can be written as the product of all of the individual probabilities [43]

$$p_i(t) = \exp\left(-\left(\sum_j r_{ij}\right)t\right), \quad (3.4)$$

with the average time between transitions being $1/\sum_j r_{ij}$. The probability density of the first escape time is written as

$$k_i(t) = \sum_j r_{ij} \exp\left(-\left(\sum_j r_{ij}\right)t\right). \quad (3.5)$$

A traditional KMC algorithm proceeds illustrated in Figure 3.5: All possible events are enumerated, and a rate table is generated that includes every possibility. The time until the next event is randomly chosen according to [42]

$$t_{rand} = \frac{-\ln(u)}{\sum_j r_{ij}}, \quad (3.6)$$

with u being a uniformly distributed random number on $[0,1]$. Choosing the next event time in this manner is consistent for a process with the rate constant of $\sum_j r_{ij}$, given the distribution in eq. (3.5) [42]. The identity of the event that takes place is chosen randomly, as well, biased such that possible events with faster rates are chosen more

often. After the chosen event is executed, the rate table is updated, and the algorithm repeats.

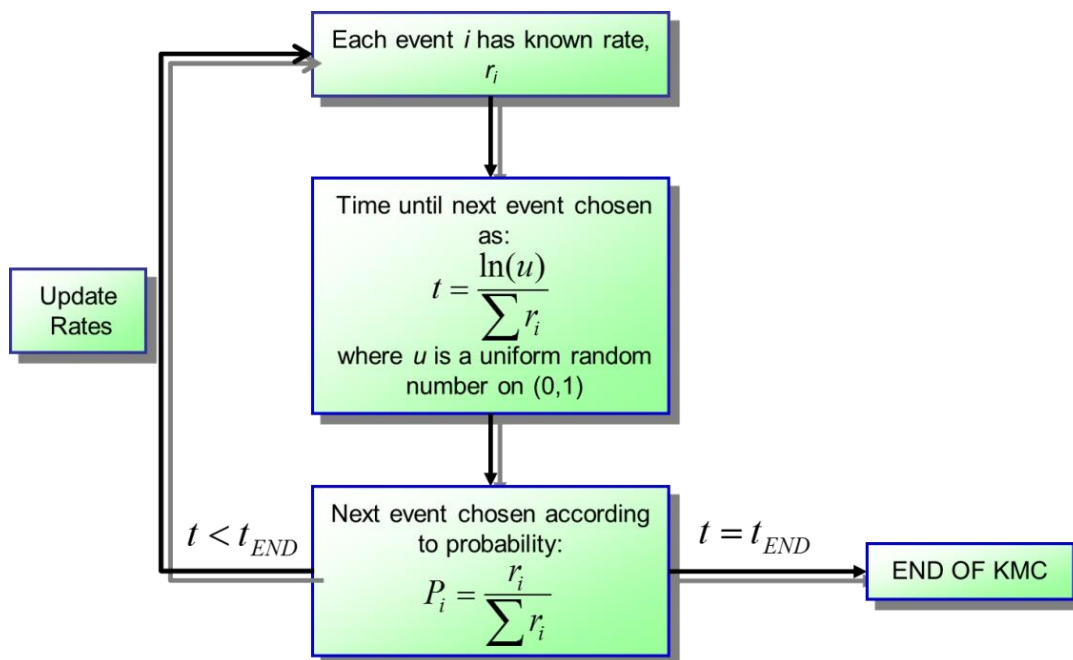


Figure 3.5. Schematic of KMC algorithm

The primary limitation of KMC is that all possible events need to be known (and specified quantitatively by rates) at all system states. Omission of important events generally leads to incorrect simulation predictions. In contrast, the single physical input to direct atomistic simulations such as MD or atomistic Monte Carlo is a potential function that may be empirical or quantum mechanical. Once this is specified, no other physical insight into the system behavior is required. In this context, KMC simulations are conceptually similar to other approaches that require mechanistic input, such as rate equation models based on ordinary or partial differential equations. However, as will be discussed further below, it is often the case that the inputs to KMC are more directly

available from molecular simulations, providing an advantage over other simulation methods.

KMC models may be posed at arbitrary length scales. At one end of the spectrum, the KMC representation may be fully atomically resolved, i.e., every atom in the system is explicitly represented. Here, there are two broad classes of models: on-lattice and off-lattice. On-lattice models, in which the atoms are constrained to a fixed set of sites (usually lattice sites in a crystalline system) are easier to construct because of easier enumeration of events and their rates. One example of an on-lattice KMC model was developed by Dai and co-workers [44] to study vacancy aggregation in silicon. Assuming that vacancies interacted up to the 8th-nearest neighbor shell, an 8 parameter model for the vacancy hopping rates as a function of local environment was parameterized using MD simulations. Figure 3.6(a) shows a vacancy aggregation configuration from a simulation. As will be discussed at the end of this Chapter, the expense of fully parametrizing a defect-mediated diffusion model was a factor in our choice of simulation technique.

Other examples of on-lattice KMC models have been applied in atomic surface morphological evolution studies. To illustrate the impact on surface morphologies of strained interactions between mismatched adatoms and an underlying substrate, Mattsson and Metiu [45, 46] imposed a periodic strain field on the surface of a substrate. This strain field was supposed to mimic the elastic interactions between deposited atoms and the surface, and the strain field was shown to induce the coalescence of the deposited layer into islands (Figure 3.6(b)). Notably, and consistent with the discussion about the nature of nucleation processes in Chapter 1, it was shown that these structured strain

fields impact coarsening of monolayer islands but do not affect the initial nucleation process, an important restriction to the impact of strain on patterning. A limitation to this analysis, however, is that only submonolayer (i.e., two-dimensional) regimes can be modeled using this approach due to the lack of an interaction potential between adatoms. Schulze and Smereka [47, 48] developed a more realistic KMC-based surface growth model, by explicitly considering surface strain effects. The elastic interactions were modeled using simplified ball-and-spring interactions, which greatly simplifies the computational cost of elastic energy calculations as opposed to solving the full stress problem within the linear elastic framework. Despite the simplification of the elastic field calculation, this approach is capable of producing faceted, three-dimensional islands during epitaxial growth (Figure 3.6(c)).

As discussed above, a primary limitation of KMC is needing to know the rates for all possible transitions at any time during the simulation. For on-lattice methods, enumerating a list of transitions is straightforward, as the connectivity of the lattice determines possibilities. However, to remove the assumption of all elements of a process happening in accordance with a pre-defined lattice, off-lattice KMC methods have been developed. In the off-lattice framework, a saddle point search is conducted for each atom at its arbitrary position [49], with each saddle point found added to the list of possible transitions. The KMC algorithm proceeds as usual, given the list of possible transitions. In one example of off-lattice KMC, Henkelman and Jonsson [50] simulated island ripening on a surface (Figure 3.6(d)).

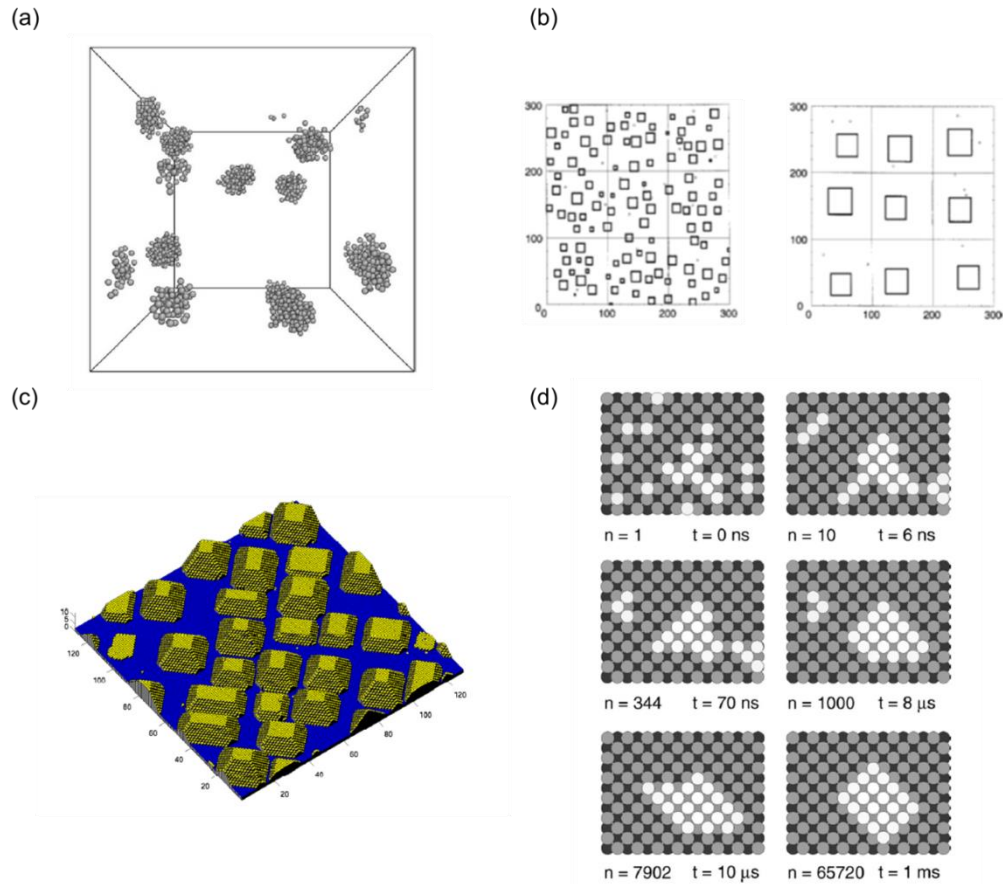


Figure 3.6. (a) Snapshot of vacancy clusters in silicon. Taken from ref. [44] (b) Single atom-thick island distribution (squares) during deposition on a patterned surface predicted by KMC. Here, the binding energy between substrate and adatom varies sinusoidally in x and y . Left – configuration at coverage 0.15 ($T=400\text{K}$); right – configuration after coarsening at $T=800\text{K}$. Taken from ref. [45] (c) Dewetting and islanding seen after three monolayers of growth. Taken from ref. [48] (d) Ripening of islands of Al on Al surface. Taken from ref. [50].

Both on- and off-lattice atomically resolved KMC achieve significant temporal gains versus fully resolved MD. However, both of these approaches are limited by the size of the atomic jump, which increases the number of possible events, shortening the average timestep (see eq. (3.6)). Thus, there have been a number of approaches to accelerate KMC, notably via parallelization and “net-event”: Parallelization of KMC is accomplished by subdividing the domain into different subdomains, which are assigned

to different CPU cores (See Figure 3.7(a)) [51]. The “skin” region of a domain is defined by the interaction distance of the transition, such that all events inside the skin region are independent of the other subdomains. Events are executed on each core, and if the event occurs in the skin region of a given core, the simulation stops on that core and waits for further instructions. Once all cores have events in the skin region, the least advanced time among all the cores is determined, the overall system clock is advanced by that time, and all events after that time on all the cores other than the one with the least advancement are reversed. The algorithm then repeats. Good efficiency is achieved on a moderate number of cores, but dramatically decreases as the number of cores increases (Figure 3.7(b)).

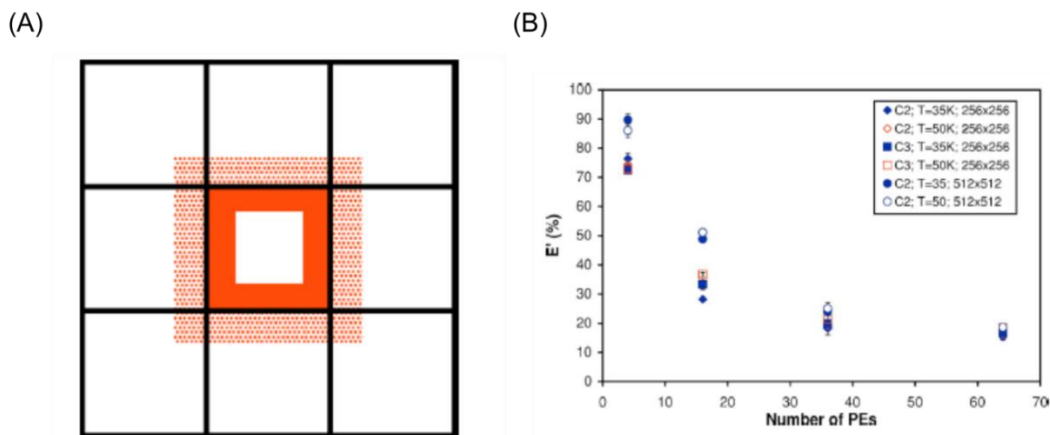


Figure 3.7. (a) Domain decomposition into nine regions, with shaded “ghost” regions and solid “skin” regions for the central domain. The ghost region of one domain is the skin region of its neighbor (b) Parallel efficiency, versus number of CPU cores (PEs), defined as the ratio of CPU time on one core for N rates divided by the CPU time on PE cores for PE×N rates., for some model diffusion systems. Taken from ref. [51].

The “net event” framework, useful where the move basis is comprised of reversible moves, lumps forward and reverse event rates into one net event [52], and has been shown to only impact the noise of the solution, not the solution itself versus a

traditional KMC. This technique is useful where there is a separation of timescales between different pairs of events. Since the sum of the rates will be dominated by the fast events in such a system, if a fast forward event and fast reverse event have the same order of magnitude, the sum of the “net” rates will be far lower than the sum of all the rates, increasing the timestep dramatically. We use this approach to model large SiGe systems in Chapter 5.

While parallelization and “net event” can achieve temporal acceleration in atomically resolved KMC models, spatial coarse-graining (CGKMC) is another approach to facilitate modeling of even longer length and time scales. In the simplest form of CGKMC, atoms are placed into cells, and cells are characterized by occupancy fraction. Possible transitions are still one particle hopping into a vacant space in an adjacent cell [53, 54]. The main assumption in coarse-graining from atomically resolved KMC to CGKMC is that the local microstructure within cell (i.e., beyond resolution of the model) equilibrate at a much faster time scale than that between hops [41]. The combination of the longer jump distance (i.e., cellular jumps) shortening rates and a reduction in the number of rates reduces the sum of the rates, increasing the average timestep. This approach has been adapted by Castrillo and co-workers [38], who parametrized point defect diffusion rates in SiGe to drive a CGKMC model interdiffusion, and is the basis for our model that we discuss in detail in the next Chapter. In addition, Vlachos and co-workers have modeled diffusion in particles that interact via an interatomic potential using CGKMC [54], including extending the method to operate on a variable-sized cellular grid, giving higher resolution as desired, while minimizing overall computational expense [55, 56]. We use this approach in Chapter 5 to enhance resolution in SiGe.

Temporal acceleration within the CGKMC framework is also possible. Parallelization, as discussed above, could be extended to CGKMC systems to achieve further gains. In addition, τ -leaping is an approach that removes the restriction of one-move-at-a-time [57, 58]. In this method, many single-atom processes are combined together into one process. This approach is inexact, however, and the number of bundled events must be chosen such that the change in rates is small during the execution of any one bundle. However, one wants to bundle as many events as possible to maximize acceleration. There have been many attempts to optimize bundle selection [57, 59, 60].

3.3 Continuum Methods

Continuum models, based on partial differential rate equations, provide an alternative to coarse-grained kinetic Monte Carlo simulations. Although it is difficult to make rigid statements about the relative merits of continuum and coarse-grained discrete models, the phase field framework has proven to be particularly useful in the modeling of microstructure evolution in both bulk and surface settings.

The phase field methodology was initially formulated by Cahn and Hilliard [61] as an alternative to the standard ‘sharp interface’ approaches. In the traditional sharp interface setup, diffusion equations are solved in each domain, while some constitutive law is imposed at the interface (e.g., a flux balance). The presence of morphological complexity and/or abrupt gradients at the interface makes sharp interface models computationally challenging, and generally requires sophisticated numerical solutions to address [62-64]. In the phase field representation, one or more continuous ‘phase-field’ variables are defined across the entire domain, including the interface. Consequently, the

interface becomes implicitly defined by the locus of points that exhibit some (usually intermediate) value of the phase-field variable(s) [65-68].

A prototypical phase-field evolution equation for concentration C (also known as the Cahn-Hilliard equation) is given by

$$\frac{\partial C}{\partial t} = M \nabla^2 \left[\frac{\partial W(C)}{\partial C} - 2\gamma \nabla^2 C \right], \quad (3.7)$$

a diffusion equation for the mass flux, \mathbf{J} , of composition, written as

$$\mathbf{J} = -M \nabla \frac{\delta F}{\delta C} = -M \nabla \left[\frac{\partial W(C)}{\partial C} - \nabla \cdot 2\gamma \nabla C \right], \quad (3.8)$$

with F being the free energy density of the material,

$$F = W(C) + \gamma (\nabla C)^2, \quad (3.9)$$

assuming constant M and γ . The bulk energy contribution to the free energy, $W(C)$, is typically assumed to be a double-welled potential to allow the equilibrium existence of two separate phases [65]. For two phases A and B , a form of $W(C)$, for an regular solution [69], is

$$W(C) = \frac{s}{2} \left[\varepsilon_{AA} C^2 + \varepsilon_{BB} (1-C)^2 + \varepsilon_{AB} C(1-C) \right] + kT \left[C \ln C + (1-C) \ln(1-C) \right], \quad (3.10)$$

where s is the number of bonds per atoms, ε_{AA} is the bond energy of A-A, ε_{BB} is the bond energy of B-B, and ε_{AB} is the bond energy of A-B. There are other possible forms of $W(C)$, as well [65, 69]. The second term in eq. (3.9) describes the interfacial energy of the two phases: Since the term depends on the gradient of C , it is zero everywhere but the interface of the two phases (see discussion of how interface is defined by locus of points with equal concentration), and thus controls how the phase boundary moves in space.

Lou and Bassani incorporated elastic effects into the phase field framework to model precipitates in matrix over a wide range of component moduli and elastic misfit [69]. The elastic energy contribution to the free energy equation is represented by an additional term to eq. (3.7),

$$\frac{\partial C}{\partial t} = -\nabla \cdot \mathbf{J} = M \nabla^2 \left[\frac{dW(C)}{dC} - 2\gamma \nabla^2 C + \frac{\partial E(\boldsymbol{\varepsilon}_{ij}, C)}{\partial C} \right], \quad (3.11)$$

where the elastic energy density, E , is a function of composition and strain. The total strain includes contributions from transformation strain and elastic strain (via constitutive relation), and the elastic strain energy is written as

$$E(\boldsymbol{\varepsilon}_{ij}, c) = \frac{1}{2} (\boldsymbol{\varepsilon}_{ij} - \boldsymbol{\varepsilon}_{ij}^T) \tilde{\mathbf{C}}_{ijkl} (\boldsymbol{\varepsilon}_{kl} - \boldsymbol{\varepsilon}_{kl}^T), \quad (3.12)$$

where the strain without superscript T is the total strain and the strain with superscript is the transformation (misfit) strain. The effective stiffness matrix, $\tilde{\mathbf{C}}$, is a function of concentration, and is assumed to be continuously varying, with a local effective value at each material point. Using the small deformation approximation, the equilibrium equation, $\sigma_{ij,j} = 0$, is written in the form of the Navier equations

$$\left\{ \tilde{\mathbf{C}}_{ijkl} \left[\frac{1}{2} (u_{k,l} + u_{l,k}) - \boldsymbol{\varepsilon}_{kl}^T \right] \right\}_{,j} = 0, \quad (3.13)$$

where \mathbf{u} is the vector of displacements. Lou and Bassani performed simulations with periodic stress fields using this approach, and saw stress-aligned phase separation of two phases with prescribed misfit (See Figure 3.8).

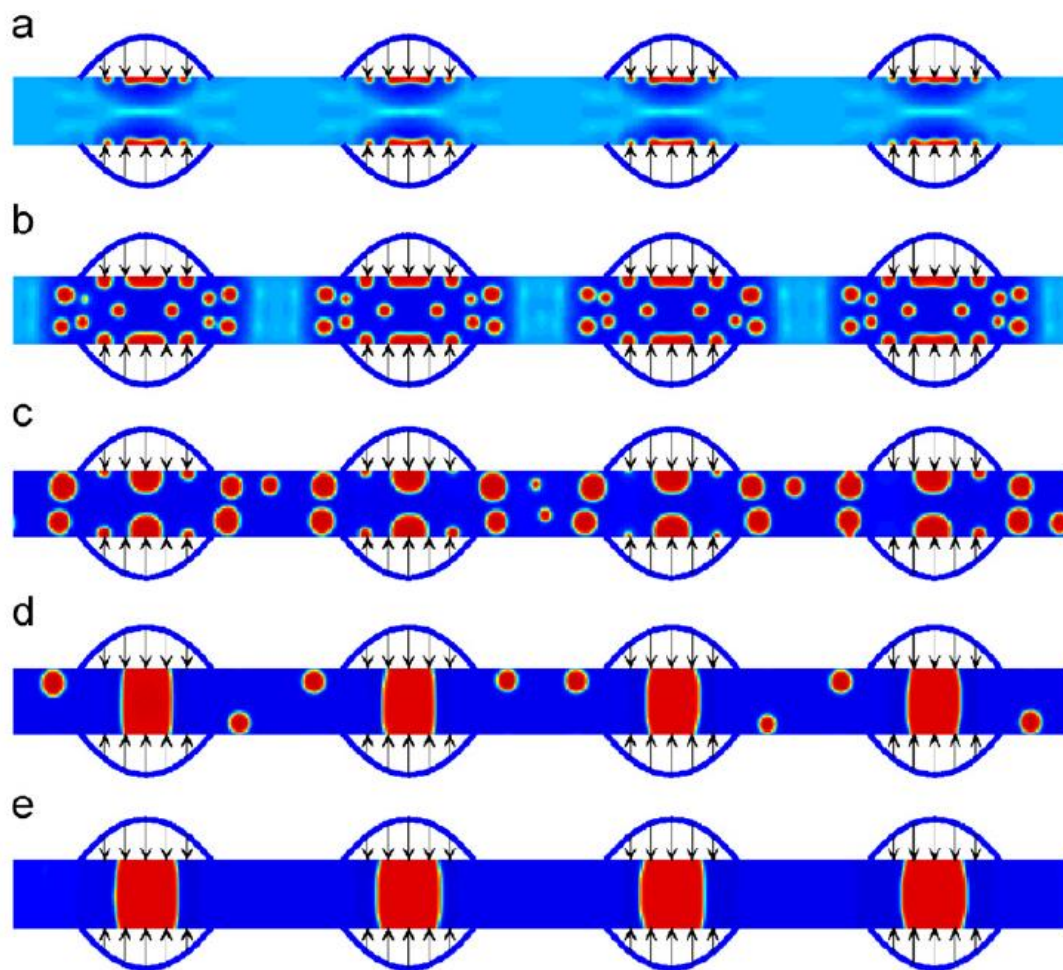


Figure 3.8. Temporal evolution of phase aggregation in the presence of periodic applied strain. The red regions are negatively (tensile) strained precipitates, which is equivalent to smaller atoms aggregating in regions of imposed compression. Taken from ref. [69].

Physically, given that there is no true phase separation in an initially homogeneous system diffusing under the influence of applied stress (i.e. there is a continuously varying compositional profile that develops over the course of an anneal, without the nucleation of precipitates), it is difficult to define distinct “phases” for a phase field model for the system considered in this thesis. Computationally, however, despite the expense in solving Navier’s equations for displacement [69], phase field approaches are far less expensive than even coarse-grained KMC approaches.

3.4 Conclusions

As discussed above, and as will be discussed in detail in the following Chapter, Castrillo and co-workers [38] have parameterized an interdiffusion CGKMC framework. Given that CGKMC is quite efficient (as discussed in the preceding section) and that the bulk of the required detailed parametric fitting has already been performed, we have chosen the Castrillo and co-workers model as the basis of our analysis. The SiGe heterosystem will be systematically investigated, using this multiscale CGKMC simulation tool.

Chapter 4. Computational Analysis of Interdiffusion in Silicon-Germanium Heterosystem for Axisymmetric and Two-Dimensional Geometries

4.1 Introduction

In Chapter 2, we described a scalable approach for robustly creating three-dimensional structures in the near-surface region of semiconductor substrates that may be useful as quantum-confined structures (QCSs). Briefly, an indenter array fabricated by etching a silicon wafer is pressed against a SiGe wafer at elevated temperature, which creates a laterally patterned stress field in the near-surface region of the wafer. The stress field creates a thermodynamic driving force for compositional redistribution of the Si and Ge atoms, whereby the larger Ge atoms tend to move away from the areas of compressive stress. Following removal of the indenter array, the SiGe wafer was found to exhibit an array of pure Si “dots” located at the regions where the indenter tips were placed.

This proof-of-concept experimental study demonstrates that stress-mediated compositional patterning is a potentially attractive (i.e., simple, scalable and robust) route to creating addressable arrays of QCSs. However, employing this approach in practice to create useful QCS configurations (e.g., with sufficiently abrupt transitions between regions of strongly differing compositions—and therefore electronic bandgaps), will require an extensive assessment of the processing parameter space, which is both heterogeneous and high-dimensional. For example, the final compositional distribution is dependent on the indenter tip shape and size, the indenter array spacing and pattern, the annealing temperature-time history, as well as the initial substrate composition and thickness. Moreover, processing constraints require that annealing temperatures and

indentation stresses be kept low enough to avoid the formation of plastic defects such as dislocations and stacking faults. Finding optimal designs for the compositional patterning approach will therefore require a large number of trials, and although a particular indenter array should be reusable, modifications of the array geometry will require a new one to be fabricated each time. Moreover, the characterization required to assess the outcome of each experiment is both time consuming and costly.

For all of the above reasons, a quantitatively predictive simulation of the stress-mediated compositional patterning process is highly desirable; this is the subject of the present Chapter. Although additional models that predict electronic band structure for the resulting compositional configurations would ultimately be required for ‘closing the design and optimization loop’, such modeling is outside the scope of the present work. The compositional evolution model is based on a coarse-grained lattice kinetic Monte Carlo simulation, in which the semiconductor domain is subdivided into a rigid lattice of cubic sub-volumes of a fixed size. Atomic exchanges between neighboring Si and Ge atoms are used to evolve the system configuration in time; rates for these events are derived based on local values of the elastic stress, composition, and temperature. The coarse-graining enables the consideration of length and timescales that correspond directly to experimental conditions with reasonable computational expense. Next, key model elements, physical assumptions, and parameter values are introduced. The model is then used to assess how various parameters impact the compositional redistribution upon the action of indentation; in some cases, these predictions are compared to experimental observations. Finally, sensitivity analysis is presented for some of the important parameters.

4.2 Model for Atomic Diffusion in SiGe

Diffusion of Si and Ge atoms in SiGe is mediated by native point defects (vacancies (V) and interstitials (I)) in one or more charge states. Consequently, atomic diffusion in SiGe is intimately coupled to point defect diffusivities and concentrations, both of which are strong functions of temperature, composition, and lattice strain.

As discussed in Chapter 3, Castrillo and co-workers [38] have parameterized a defect-mediated interdiffusion model in SiGe as a function of composition and temperature. Here, in the interest of clarity, we summarize the model.

In an unstrained, compositionally uniform SiGe wafer at equilibrium, the concentration for a neutral defect, A , is characterized by the Arrhenius relationship,

$$C_{A^0} = C_{0A^0} \exp\left(-\frac{E_{fA^0}}{kT}\right), \quad (4.1)$$

where both the prefactor and barrier are function of composition. The diffusivity of a neutral defect also obeys Arrhenius behavior,

$$D_{A^0} = D_{0A^0} \exp\left(-\frac{E_{mA^0}}{kT}\right). \quad (4.2)$$

The concentration of charged defects depend on the position of the electronic charge relative to the Fermi level, e_F , which is computed as follows: First, the band gap energy, E_g , of the material is taken to be the minimum of the value computed using the X-like minimum of the conduction band (CB), E_g^X , and the L-like minimum of the CB, E_g^L (The X and L band gap energies are computed using two different wave vectors [70]). Both values scale with temperature as

$$\frac{E_g(T)}{E_g(0)} = 1 - \frac{FT^2}{T+B}. \quad (4.3)$$

Second, the effective densities-of-states (EDOS) for the X and L minima are assumed to be $N_c^X = N_c(\text{Si})$ and $N_c^L = N_c(\text{Ge})$, respectively, and are assumed to not be functions of composition in the SiGe alloy. The EDOS for the valence band, N_v , is a function of composition. All three EDOS scale with temperature as $T^{3/2}$. The total EDOS of the CB is computed as

$$N_c = \begin{cases} N_c^L + N_c^X \exp\left(\frac{-(E_g^X - E_g^L)}{kT}\right), & E_g^X > E_g^L \\ N_c^X + N_c^L \exp\left(\frac{-(E_g^L - E_g^X)}{kT}\right), & E_g^L > E_g^X \end{cases} \quad (4.4)$$

Finally, the Fermi level, e_F , is computed as [71]

$$e_F = \frac{E_g}{2} + \frac{kT}{2} \ln\left(\frac{N_v}{N_c}\right). \quad (4.5)$$

The concentrations of charged defects depend on e_F as

$$\frac{C_{A^{j+1}}}{C_{A^j}} = \exp\left(\frac{e_{A(j,j+1)} - e_F}{kT}\right), \quad (4.6)$$

where j is the charge index of the defect. The diffusivities of charged defects also are assumed to obey Arrhenius relationships, i.e.,

$$D_{A^j} = D_{0A^j} \exp\left(-\frac{E_{mA^j}}{kT}\right). \quad (4.7)$$

All diffusivity prefactors and migration energies are assumed to be constant with respect to composition. The total diffusive capacity of a defect is computed as the sum of the

transport capacities, $D_A C_A$, of the defect, summed over all of the charge states, and normalized by the atomic density as

$$DC_A = \frac{1}{C_a} \sum_j D_{A^j} C_{A^j}, \quad (4.8)$$

where C_a is the atomic density, ($\sim 5 \times 10^{22}$ atoms/cm³). For pure Si or Ge, the atomic self-diffusivity is written as

$$D_{self} = \sum_A f_A DC_A, \quad (4.9)$$

with f_A being the correlation factor between defect hops, taken to be 0.5 for vacancies and 0.7 for interstitials [38]. The correlation factor arises from the fact that atomic hops that occur due to a defect hopping are not truly random [72]. However, in a $\text{Si}_{1-x}\text{Ge}_x$ alloy, the diffusivities of Si and Ge are not equal. Thus, we require an additional parameter, $\alpha_A = D_{Ge}^A / D_{Si}^A$, to accommodate asymmetric diffusion. Finally, we can write the self-diffusivities of Si and Ge atoms in $\text{Si}_{1-x}\text{Ge}_x$ as

$$\begin{aligned} D_{Si} &= \frac{f_v DC_v}{1-x+x\alpha_v} + \frac{f_i DC_i}{1-x+x\alpha_i} \\ D_{Ge} &= \frac{\alpha_v f_v DC_v}{1-x+x\alpha_v} + \frac{\alpha_i f_i DC_i}{1-x+x\alpha_i} \end{aligned} \quad (4.10)$$

Table 4.1 lists the values for all the parameters discussed here; these are taken directly from ref. [38]. Note that α , the ratio of self-diffusivities, also is assumed to follow an Arrhenius relationship, i.e., $\alpha_A = \alpha_{0A} \exp(-E_{\alpha A} / k_B T)$. All prefactors are assumed to vary exponentially with composition, while all activation energies are assumed to vary linearly with composition, except for E_g^X , $e_v(-,0)$, and E_{JV^0} , which are assumed to depend quadratically on composition.

Table 4.1. Parameters used for point defect and self-diffusion in Si, Ge and Si_{1-x}Ge_x. A denotes the defect type. Taken from ref. [38].

	Si Electronic Properties	Ge Electronic Properties
$E_g^X(T=0)$	1.17 eV	0.93 eV
$d^2E_g^X/dx^2$	0.4 eV	
$E_g^L(T=0)$	2.014 eV	20.744 eV
F	$4.04 \times 10^{-4} \text{ K}^{-1}$	$46.41 \times 10^{-4} \text{ K}^{-1}$
B	636 K	235 K
$N_c(T=300\text{K})$	$3.2 \times 10^{19} \text{ cm}^{-3}$	$1.0 \times 10^{19} \text{ cm}^{-3}$
$N_v(T=300\text{K})$	$1.8 \times 10^{19} \text{ cm}^{-3}$	$5.4 \times 10^{19} \text{ cm}^{-3}$

	Si Interstitial Properties	Ge Interstitial Properties	Si Vacancy Properties	Ge Vacancy Properties
C_{0A^0}	$8 \times 10^{26} \text{ cm}^{-3}$	$8 \times 10^{26} \text{ cm}^{-3}$	$2.5 \times 10^{26} \text{ cm}^{-3}$	$7 \times 10^{27} \text{ cm}^{-3}$
E_{fA^0}	4.1 eV	3.7 eV	3.9 eV	3.05 eV
$d^2E_{fA^0}/dx^2$	-----		-1.4 eV	
$e_{A(0,+)}$	0.3 eV	0 eV	0.03 eV	0.1 eV
$e_{A(+,++)}$	0.55 eV	-0.2 eV	0.13 eV	0 eV
$e_{A(-,0)}$	1 eV	0.7 eV	0.6 eV	0.2 eV
$d^2e_{A(-,0)}/dx^2$	-----		1 eV	
$e_{A(--,-)}$	-----	-----	1.06 eV	0.4 eV
α_{0A}	1.2	1.2	5	0.55
$E_{\alpha A}$	0 eV	0 eV	0.1 eV	-0.2 eV
D_{0A^0}	0.05 cm ² /s		$1 \times 10^{-3} \text{ cm}^2/\text{s}$	
D_{0A^+}	0.05 cm ² /s		$1 \times 10^{-3} \text{ cm}^2/\text{s}$	
$D_{0A^{++}}$	0.05 cm ² /s		$1 \times 10^{-3} \text{ cm}^2/\text{s}$	
D_{0A^-}	0.05 cm ² /s		$1 \times 10^{-3} \text{ cm}^2/\text{s}$	
$D_{0A^{--}}$	-----		$1 \times 10^{-3} \text{ cm}^2/\text{s}$	
E_{mA^0}	0.8 eV		0.4 eV	
E_{mA^+}	0.8 eV		0.35 eV	
$E_{mA^{++}}$	0.8 eV		0.3 eV	
E_{mA^-}	0.8 eV		0.45 eV	
$E_{mA^{--}}$	-----		0.18 eV	

Point defect concentrations and diffusivities computed using the values in Table 4.1 are able to accurately reproduce measured atomic self-diffusivities (using eq. (4.10)) and point defect transport capacities in unstrained $\text{Si}_{1-x}\text{Ge}_x$ from the literature; Figure 4.1 shows data fits, along with representative data from the literature, for (a) Si self-diffusion and (b) Ge self-diffusion in $\text{Si}_{1-x}\text{Ge}_x$ across a wide temperature range, while (c) is a similar plot for transport capacities in Si and Ge.

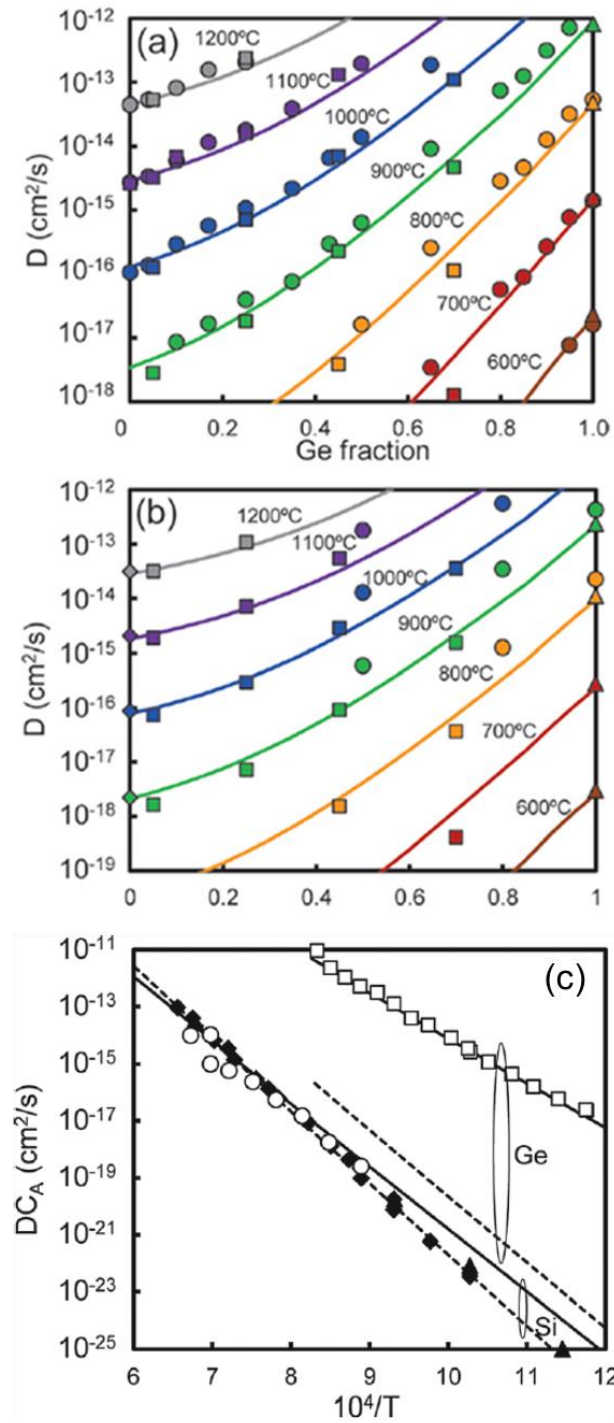


Figure 4.1. (a) Si and (b) Ge self-diffusivity at various temperatures in unstrained SiGe alloys of different compositions. (c) Transport capacities in pure, unstrained, Ge and Si as a function of inverse temperature. Solid lines and white symbols are DC_v and dashed lines and black symbols are DC_I . Symbols are literature values and lines are model fits. Taken from ref. [38].

4.2.1 Diffusion of Point Defects Under Stress

A theoretical framework for quantifying the impact of lattice stress on defect diffusion has been described by Aziz [32], in which a stress field $\boldsymbol{\sigma}$ modifies the diffusivity of point defect species A according to

$$DC_{j,A}(\boldsymbol{\sigma}) = DC_A(\mathbf{0}) \exp\left(\frac{\boldsymbol{\sigma} : \mathbf{V}_{j,A}^*}{k_B T}\right), \quad (4.11)$$

where $\mathbf{V}_{j,A}^* = \mathbf{V}_A^f + \mathbf{V}_{j,A}^m$ is the activation volume tensor for hops along direction j , with \mathbf{V}^f and \mathbf{V}^m being the formation and migration volume tensor contributions, respectively. A more detailed discussion of the Aziz framework, along with detailed calculations of the activation volume tensor, is presented in Chapter 6. Here, we only provide a brief summary and use the parameters introduced in ref. [38].

For the (001)-oriented films we consider here, and assuming that the free surface is the only source of point defects, the formation volume tensor is given by [32, 38]

$$\mathbf{V}_A^f = \begin{pmatrix} \frac{V_A^r}{3} & & \\ & \frac{V_A^r}{3} & \\ & & \frac{V_A^r}{3} \pm \Omega \end{pmatrix}, \quad (4.12)$$

where Ω is the atomic volume that corresponds to the addition(subtraction) of an atom at the (001) surface to create a vacancy(self-interstitial) in the bulk. The relaxation volume, V_A^r , represents the additional volume change due to lattice relaxation following point defect generation. Off-diagonal components of the formation volume tensor are zero due

to crystal symmetry [73]. The migration volume tensor represents the additional volume change associated with point defect migration. In the (001) direction, the migration volume is given by

$$\mathbf{V}_{001,A}^m = \begin{pmatrix} V_{\perp,A}^m & & \\ & V_{\perp,A}^m & \\ & & V_{\parallel,A}^m \end{pmatrix}, \quad (4.13)$$

where $V_{\parallel,A}^m$ and $V_{\perp,A}^m$ represent changes parallel and perpendicular, respectively, to the direction of hopping motion. Similar expressions apply for migration along the other directions. The following parameter values for the activation volumes, which are used as base case values in the present study [38]:

$$\begin{aligned} \left(\frac{V_I^r}{3} + V_{\parallel,I}^m \right) &= 0.5\Omega \\ \left(\frac{V_I^r}{3} + V_{\perp,I}^m \right) &= 0.3\Omega \\ \left(\frac{V_V^r}{3} + V_{\parallel,V}^m \right) &= -0.35\Omega \\ \left(\frac{V_V^r}{3} + V_{\perp,V}^m \right) &= -0.35\Omega \end{aligned} \quad (4.14)$$

It should be noted that, generally, values for the various components of the activation volume tensor are not well established in the literature [74-80]; sensitivity of the model predictions to these parameters is discussed briefly in Section 4.4, and a detailed study of these values is presented in Chapter 6. Finally, stress may also alter the electronic band structure of the material, further modifying the diffusivities of point defects. However,

these modifications were found to be relatively minor compared to the primary impact of stress [38] and are neglected in this work.

4.3 Simulation Details

4.3.1 Lattice Kinetic Monte Carlo (LKMC) Simulation Framework

A coarse-grained LKMC [43, 81, 82] simulation was developed in which a rigid, rectangular domain is subdivided into a lattice of cubic cells, each measuring L_{cell} in length and containing n_{tot} (Si or Ge) atoms as shown in Figure 4.2(a). Periodic boundary conditions were applied in the lateral directions (x and y) while no-flux boundary conditions were applied in the directions normal to the substrate surface (z). The microscopic distribution of atoms in each cell is known to correspond to an ideal solid solution for most temperatures of interest, i.e., for a given composition, Si and Ge atoms are mixed randomly [83]. In other words, the mixing enthalpy of a mixture of Si and Ge atoms is zero, and the energetics associated with atomic exchanges do not vary with changes in microscopic configuration at a fixed overall composition. Consequently, only the overall composition in each cell was required to specify the state of the coarse-grained system; see Figure 4.2(b).

Point defects within each cell are treated implicitly, and here are assumed to be always present in their equilibrium concentrations for given local composition, stress, and temperature. This is in contrast to the model in ref. [38], in which the point defect distribution is updated explicitly on the basis of diffusional fluxes across the entire domain. The assumption of quasi-equilibrium point defect distributions for the process of

interest in this thesis may be validated by considering that point defect equilibration proceeds via interaction with the nearby film surface that acts as a sink and source for point defects. For distances on the order of 10 microns, point defect diffusion timescales are of order 100 milliseconds, which, as will be demonstrated later in the discussion of the model predictions, is much faster than the timescales associated with compositional redistribution throughout the film. Of course, highly non-equilibrium processing, such as ion-implantation, would require accounting of non-equilibrium point defect distributions [38]; such situations are not considered here.

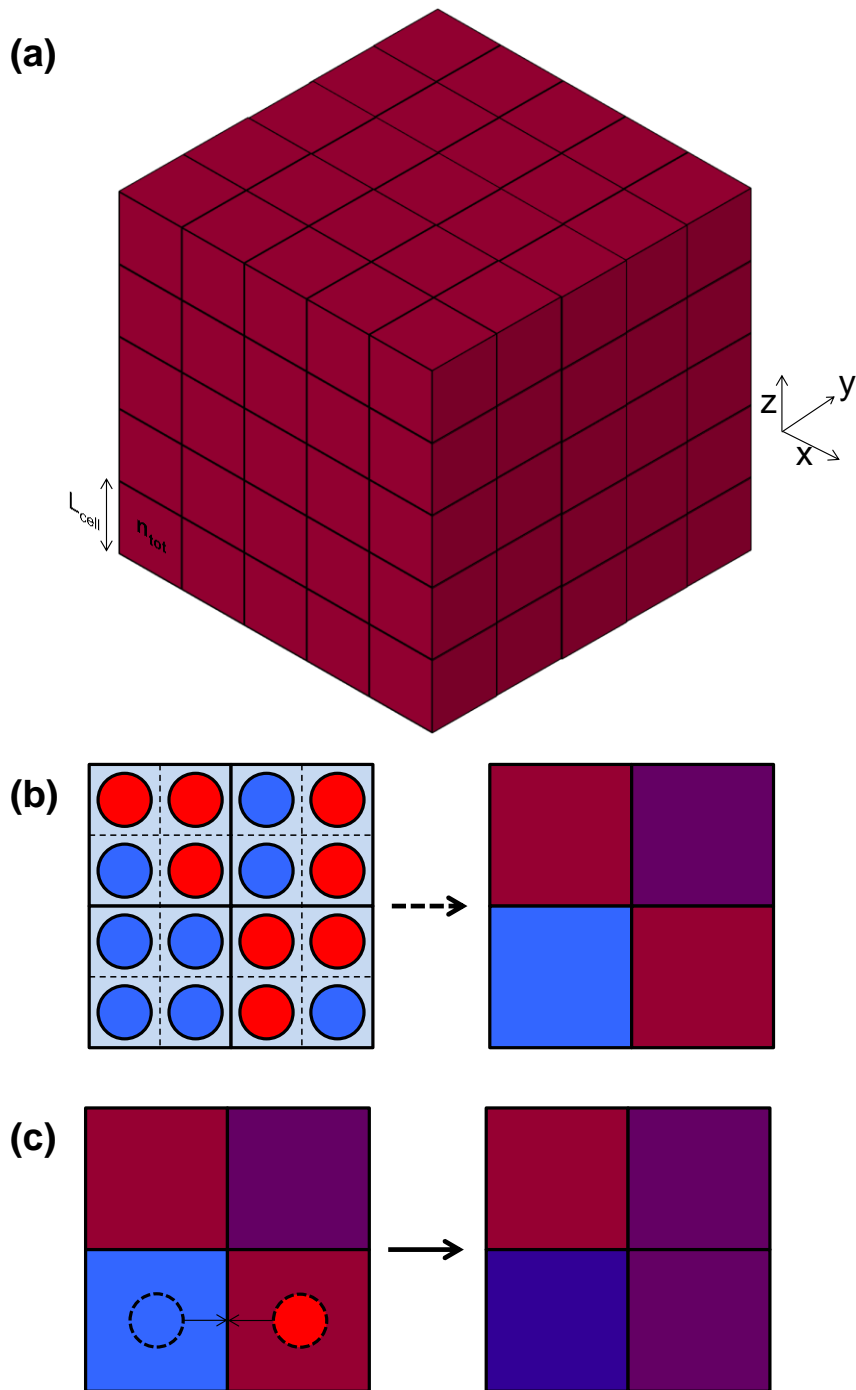


Figure 4.2. (a) Schematic of LKMC domain comprised of cubic cells measuring L_{cell} in length and containing n_{tot} Si and/or Ge atoms (b) Schematic of coarse-graining atomic configurations in cells. Red atoms represent Si and blue atoms represent Ge (c) Schematic of LKMC switch move. In the depicted exchange, a Ge atom is moving from the lower left to the lower right and an Si atom is moving from the lower right to the lower left.

The LKMC configuration state is evolved by a sequence of single Si-Ge ‘switch’ moves across two adjacent cells; see Figure 4.2(c). We employ the ‘Next Reaction’ algorithm (NRM) [84], which was developed as an efficient alternative to the standard method described in Chapter 3: Rather than selecting an event time and choosing an event after each time step, the i th event’s “wait time,” τ_i , is generated for each event

$$\tau_i = -\frac{\ln(u)}{r_i}, \quad (4.15)$$

where u is a uniformly distributed random number on $[0,1]$ and r_i is the event rate. The absolute time an event takes place is

$$t_i = t + \tau_i, \quad (4.16)$$

where t is the current simulation clock time when τ_i is generated. The list of t_i s for each event is what is tracked during the simulation. The event with the shortest t_i is selected, and the clock is updated to t_i . The compositions in the two participating cells are updated after every move, and all affected rates are updated. The advantage of this approach is that only events that are affected by the selected event need to be updated after each time step; the other t_i s are unchanged. Thus, for large systems, there is a significant computational advantage to this algorithm.

The main computational expense in NRM is the sorting required to always know the event with the next t_i , even though most possible events have the same t_i after a particular event takes place. To optimize the sorting overhead, we use a skip list [85], which is a stochastic sorting algorithm that has, on average, $O(\ln(n))$ insertion, deletion and query complexity.

Large numbers of the individual point defect hopping processes shown in Figure 3.1 eventually lead to Si-Ge intermixing, or interdiffusion, which may be conceptualized as exchanges between neighboring lattice atoms. In a $\text{Si}_{1-x}\text{Ge}_x$ bulk alloy, the probability of a particular mobile point defect species, $A=I,V$, moving an Si or Ge atom, respectively, is given by [38]

$$\begin{aligned} P_{Si}^A &= f_A \frac{(1-x)}{(1-x) + x\alpha_A} \\ P_{Ge}^A &= f_A \frac{x\alpha_A}{(1-x) + x\alpha_A} \end{aligned} \quad (4.17)$$

with $\alpha_A(x,T) \equiv D_{Ge}^A(x) / D_{Si}^A(x)$ as described in Section 4.2. The rates at which Si and Ge atoms are exchanged between two adjacent cells, ‘1’ and ‘2’, may be derived on the basis of the probabilities given in eq. (4.17), i.e.,

$$\begin{aligned} r_{Ge_1 \rightarrow Si_2} &= \frac{n_{\text{tot}}}{L_{\text{cell}}^2} \sum_{A=I,V} \left(\frac{P_{Ge_1}^A}{f_A} \left(1 - \frac{P_{Ge_2}^A}{f_A} \right) f_A D_A \frac{C_A}{C_a} \right) \\ r_{Si_1 \rightarrow Ge_2} &= \frac{n_{\text{tot}}}{L_{\text{cell}}^2} \sum_{A=I,V} \left(\frac{P_{Ge_2}^A}{f_A} \left(1 - \frac{P_{Ge_1}^A}{f_A} \right) f_A D_A \frac{C_A}{C_a} \right) \end{aligned} \quad (4.18)$$

The rate expressions in eqs. (4.18) describe an exchange of a Ge atom in cell ‘1’ with an Si atom in cell ‘2’ (top) or a Si atom in cell ‘1’ with a Ge in cell ‘2’ (bottom). The prefactors account for the total number of atoms in each cell, n_{tot} , and the distance over which the exchange is made, L_{cell} . Point defect diffusivities and concentrations are calculated based on the average composition and stress of the two cells participating in the exchange. Note that the regression procedure described in ref. [38] ensures that the self-diffusivities and point defect transport capacities employed in the present LKMC

simulations implicitly account for the effects of a variety of atomistic details including local atomic strains, electronic structure, etc. In other words, while these details are not explicitly relevant in the present application, their impacts on point defect energies and mobilities are included to the extent that the model predicts the correct self-diffusivities and transport capacities as a function of composition and temperature.

4.3.2 Rate Modifications Due to Stress and Compositional Gradients

As formulated, the rate expressions in eqs. (4.18) do not automatically account for energy changes associated with Si-Ge exchange across cells with differing compositions and stresses; this information is required to ensure that the simulation predicts the correct equilibrium state. Following ref. [38], energy changes are accounted for by modifying the self-diffusivity ratios, $\alpha_A(x, T)$, for each defect species to include the energy difference, ΔE , between moving a Ge atom and moving an Si atom in cell i , i.e.,

$$\alpha_A^{inh,i}(x_i, T) = \alpha_A^i(x_i, T) \exp\left(-\frac{\Delta E_i}{k_B T}\right). \quad (4.19)$$

To derive the form of this energy difference, note first that $\alpha_A^i(x_i, T)$ is an Arrhenius expression (see Section 4.2)

$$\alpha_A^i \equiv \frac{D_{Ge_i}^A}{D_{Si_i}^A} = \alpha_{0A}^i \exp(-E_{\alpha A}^i / k_B T), \quad (4.20)$$

which can be written as

$$\alpha_A^i = \frac{c \exp(-\beta d)}{f \exp(-\beta g)}, \quad (4.21)$$

with $\beta \equiv (k_B T)^{-1}$. Consider the case of a vacancy moving from cell 2 to cell 1. If a Ge is to move from cell 1 to cell 2 (as a coordinated move), there is an energy difference that results:

$$E_{Ge,1 \rightarrow 2} = -E_{Ge,1} + E_{Ge,2}, \quad (4.22)$$

as a Ge is removed from cell 1 (and replaced with a vacancy), and that Ge is placed in cell 2 (replacing that same vacancy). Similarly, if an Si is to move, there is an analogous expression:

$$E_{Si,1 \rightarrow 2} = -E_{Si,1} + E_{Si,2}. \quad (4.23)$$

These energy changes affect the barriers in the Arrhenius expressions for the self-diffusivities as

$$\frac{D_{Ge_1}}{D_{Si_1}} = \frac{c_1 \exp(-\beta(d_1 + E_{Ge,1 \rightarrow 2}))}{f_1 \exp(-\beta(g_1 + E_{Si,1 \rightarrow 2}))} \quad (4.24)$$

The resulting expression for alpha simplifies to:

$$\alpha_V^{inh,1} = \alpha_V^1 \exp\left(\frac{\Delta E_{Ge \rightarrow Si}^1 + \Delta E_{Si \rightarrow Ge}^2}{k_B T}\right), \quad (4.25)$$

as

$$\begin{aligned} E_{Ge,1 \rightarrow 2} - E_{Si,1 \rightarrow 2} &= (-E_{Ge,1} + E_{Ge,2}) - (-E_{Si,1} + E_{Si,2}) \\ E_{Ge,1 \rightarrow 2} - E_{Si,1 \rightarrow 2} &= \Delta E_{Ge \rightarrow Si}^1 + \Delta E_{Si \rightarrow Ge}^2 \end{aligned} \quad (4.26)$$

As we just showed, for atomic motion across two adjacent cells, this energy difference is equal to the energy difference resulting from an atomic switch across the two cells, i.e.,

$$\Delta E_1 = \Delta E_{Ge \rightarrow Si}^1(\boldsymbol{\sigma}_1, x_1) + \Delta E_{Si \rightarrow Ge}^2(\boldsymbol{\sigma}_2, x_2). \quad (4.27)$$

The energy change associated with an atomic switch across two cells was parametrized in terms of the cell stress state and cell composition. The stress state was defined in terms of the diagonal elements of the stress tensor, i.e., shear was assumed to be of secondary importance. For each instance, a periodic cubic cell containing 64 randomly distributed Si and Ge atoms arranged in a perfect diamond lattice configuration was first relaxed at a specified stress state with the conjugate gradient routine in LAMMPS [86] based on the Tersoff potential [87-89]. The identity of one randomly selected atom was then switched, the cell re-relaxed at constant volume, and the energy change recorded. It should be emphasized here that the ideal nature of the SiGe solid solution greatly simplifies these calculations because the switch energies do not depend on the microscopic configurations of the cell; this assumption was confirmed by repeating calculations for different microscopic realizations at a given overall composition for a few example cases.

We performed calculations at Ge fractions ranging from 0 to 0.9, using a stepsize of 0.1. At each composition, we performed computations at each combination of diagonal stress elements from -5 GPa to 20 GPa, with a step size of 1 GPa, a total of 12,760 computations. We then fit the energy switch data to a second order polynomial, with an R_2 of 0.994. Slices of this 4 dimensional space of energy changes corresponding to Si→Ge identity switches are shown in Figure 4.3.

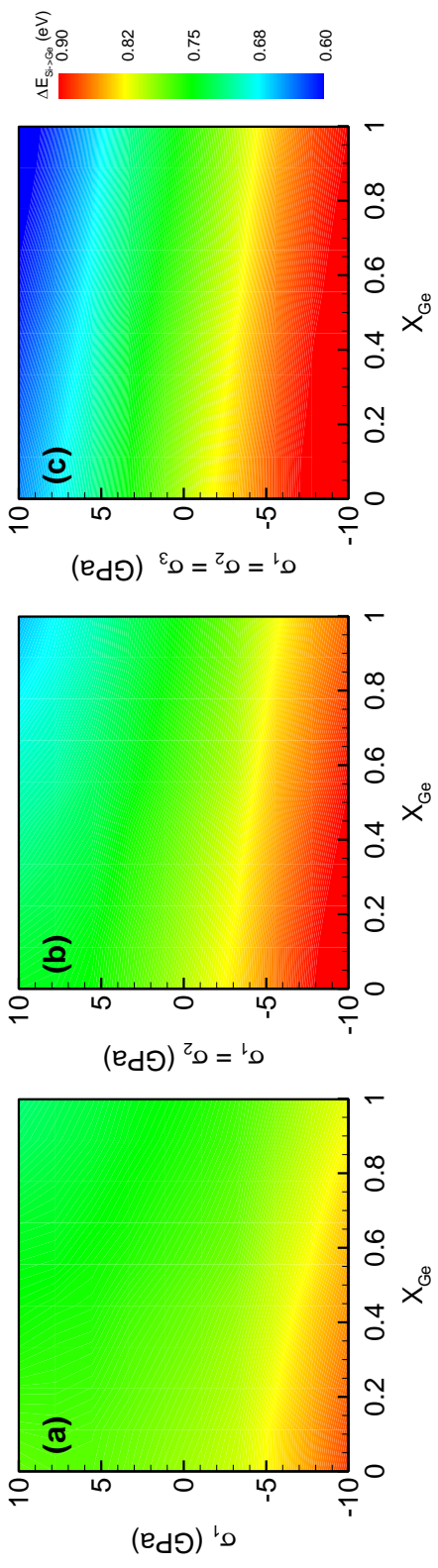


Figure 4.3. Energy change for an Si \rightarrow Ge identity flip in a 64-atom cubic Si $_x$ Ge $_{1-x}$ cell at different combinations of stress state and composition. (a) Uniaxial stress, (b) biaxial stress, and (c) hydrostatic stress. Ge \rightarrow Si identity flips lead to equal and opposite energy changes.

4.3.3 Continuum Stress Field Calculation Framework

Initial microscopic compositional fluctuations were imposed by randomly assigning identities to each (implicit) atom in every cell according to the desired overall composition. Stress fields in the SiGe film (and indenter) were computed by solving a linear elasticity contact problem with the finite element method (FEM), using the COMSOL software package [90]. Stress was generated by applying a specified body force on the indenter, pushing it into the SiGe film. For infinitely-long cylindrical ('wire') contact, a two-dimensional, a plane strain elasticity model was employed. Here, periodic boundary conditions were applied in the x -directions, the bottom z -boundary was fixed, and the top z -boundary was traction-free except in the contact region. A two-dimensional axisymmetric model was used for spherical indenters. Traction-free boundary conditions were applied at the radial edge of the domain; the z -boundary conditions are the same as those for the wire indenter case.

Without contact, computing a solution to the linear elastic stress problem involves simultaneously solving the equilibrium equations,

$$\nabla \cdot \boldsymbol{\sigma} + \mathbf{b} = \mathbf{0}, \quad (4.28)$$

with $\boldsymbol{\sigma}$ being the stress tensor and \mathbf{b} being the body force (per volume) vector, the strain-displacement relationships,

$$\boldsymbol{\varepsilon}_{Total} = \frac{1}{2} [(\nabla \mathbf{u})^T + \nabla \mathbf{u}], \quad (4.29)$$

where $\boldsymbol{\varepsilon}_{Total}$ is the strain tensor and \mathbf{u} is the vector of displacements, and the constitutive relations,

$$\boldsymbol{\sigma} = \mathbf{C} : \boldsymbol{\varepsilon}_{Elastic}, \quad (4.30)$$

where \mathbf{C} is the stiffness tensor, all subject to boundary conditions. Note that due to compositional patterning in initially homogenous $\text{Si}_{1-x}\text{Ge}_x$, $\boldsymbol{\varepsilon}_{Elastic} \neq \boldsymbol{\varepsilon}_{Total}$, yielding additional relations, $\boldsymbol{\varepsilon}_{Elastic} = \boldsymbol{\varepsilon}_{Total} - \boldsymbol{\varepsilon}_{Misfit}$, where the spatially variable $\boldsymbol{\varepsilon}_{Misfit}$ tensor is,

$$(x_{initial} - x_{local})\mathbf{I}, \quad (4.31)$$

with x being the Ge fraction [38].

We use an Augmented Lagrangian method to model contact effects, defining an additional equation, as follows:

$$P_p = \begin{cases} P - td & \text{if } d \leq 0 \\ Pe^{-\frac{td}{P}} & \text{if } d > 0 \end{cases}, \quad (4.32)$$

where P_p is the penalized contact pressure, P is the current contact pressure, d is the distance between the surfaces of contact, and t is a penalty factor that is set according to material properties. Note that t only impacts the rate of convergence, not the accuracy of the solution. The system of equations is solved iteratively, until the answer changes by less than 0.1% between successive iterations. Finally, also note that converged values of P agree with the computed value of $-\sigma_{zz}$ at the center of contact in the SiGe films, the maximum contact pressure as measured in the film [36], to within a few percent.

Several assumptions and approximations were made in the calculation of stress fields. In the majority of the reported simulation results, we assumed that Si and Ge are elastically isotropic, which, as shown by the experimentally measured cubic elastic coefficients in Table 4.2 [91], is not quite the case. As discussed in Section 4.4, this

assumption does not strongly impact the LKMC results across a wide range of applied stress, while greatly simplifying the elastic stress computations. Isotropic elastic constants, namely the Young's modulus and Poisson's ratio, were computed along the $\langle 100 \rangle$ directions for both Si and Ge (Table 1). The properties for $\text{Si}_{0.8}\text{Ge}_{0.2}$ were obtained by linear interpolation of the elastic coefficients between the Si and Ge values, and then computing the corresponding Young's modulus and Poisson's ratio. We also assumed that the elastic properties and lack of misfit of uniform $\text{Si}_{0.8}\text{Ge}_{0.2}$ are applicable to the entire domain at all times during thermal annealing. Of course, in actuality, local compositional changes during annealing would lead to misfit and changes in the local mechanical properties and therefore the applied stress field; however, we show in Section 4.4 that this simplifying assumption has little practical impact on the model predictions, which is consistent with the findings of ref. [69] for materials with lattice mismatch but minimal differences in moduli. Finally, all elastic coefficients are assumed to be independent of temperature.

Table 4.2. Elastic constants for Si, Ge and $\text{Si}_{0.8}\text{Ge}_{0.2}$. Taken from ref. [91].

Material	C₁₁ (GPa)	C₁₂ (GPa)	C₄₄ (GPa)	Young's Modulus (GPa)	Poisson's Ratio
Si	165.7	63.9	79.6	130.1	0.278
Ge	129.2	47.9	67.0	103.3	0.270
Si_{0.8}Ge_{0.2}	158.4	60.7	77.0	124.8	0.277

4.3.4 Atomistic Stress Field Comparison

In the initial formulation of our model, we attempted to solve for the stress field in the film via molecular statics calculations, simulating atomic interactions using the Tersoff interatomic potential for SiGe [87-89]. The effective mechanical properties of the harmonic indenter field (implemented using the “*fix indent*” routine in the LAMMPS software package [92]) were determined by comparing the quasi-static indentation process of a fully atomistic $\text{Si}_{0.8}\text{Ge}_{0.2}$ slab.

The elements of the atomistic stress tensor (σ) are defined as [93]

$$(\sigma_{ab}V)_i = - \left[m v_{i,a} v_{i,b} + \frac{1}{2} \sum_{n=1}^{N_2} (r_{1,a} F_{1,b} + r_{2,a} F_{2,b}) + \frac{1}{3} \sum_{n=1}^{N_3} (r_{1,a} F_{1,b} + r_{2,a} F_{2,b} + r_{3,b} F_{3,b}) \right], \quad (4.33)$$

where the subscripts “*a*” and “*b*” refer to the three Cartesian coordinate directions (*x*, *y*, *z*), v_i is the velocity of atom *i*, r_i is the position of atom *i*, and F_i is the force on atom *i* due to the type of interaction (N_2 refers to 2-body, N_3 to 3-body). Note that all velocities are zero for the quasi-static case considered here.

The idea using the atomistic stress was as follows: Once the indented (atomistic) configuration is created, atomistic stresses are computed (Figure 4.4(a)), and the stress field across the entire substrate is passed to the coarse-grained LKMC simulation. The stress in each LKMC cell is computed by averaging over all atoms that correspond to that cell (Figure 4.4(b)). The LKMC simulator evolves the system until the composition changes significantly (Figure 4.4(c)). The LKMC configuration is then used to create a consistent atomistic configuration, i.e., atomic types (Si or Ge) are randomly assigned to the last-known off-lattice atomic configuration according to the current cellular

composition. This new atomistic configuration is fed into the LAMMPS energy minimization routine and a new stress field computed holding the indenter fixed (Figure 4.4(d)). The sequence is then repeated until the simulation is terminated at a specified time. As mentioned in the preceding section, not updating the stress field during calculations will be shown to have little to no impact on the results.

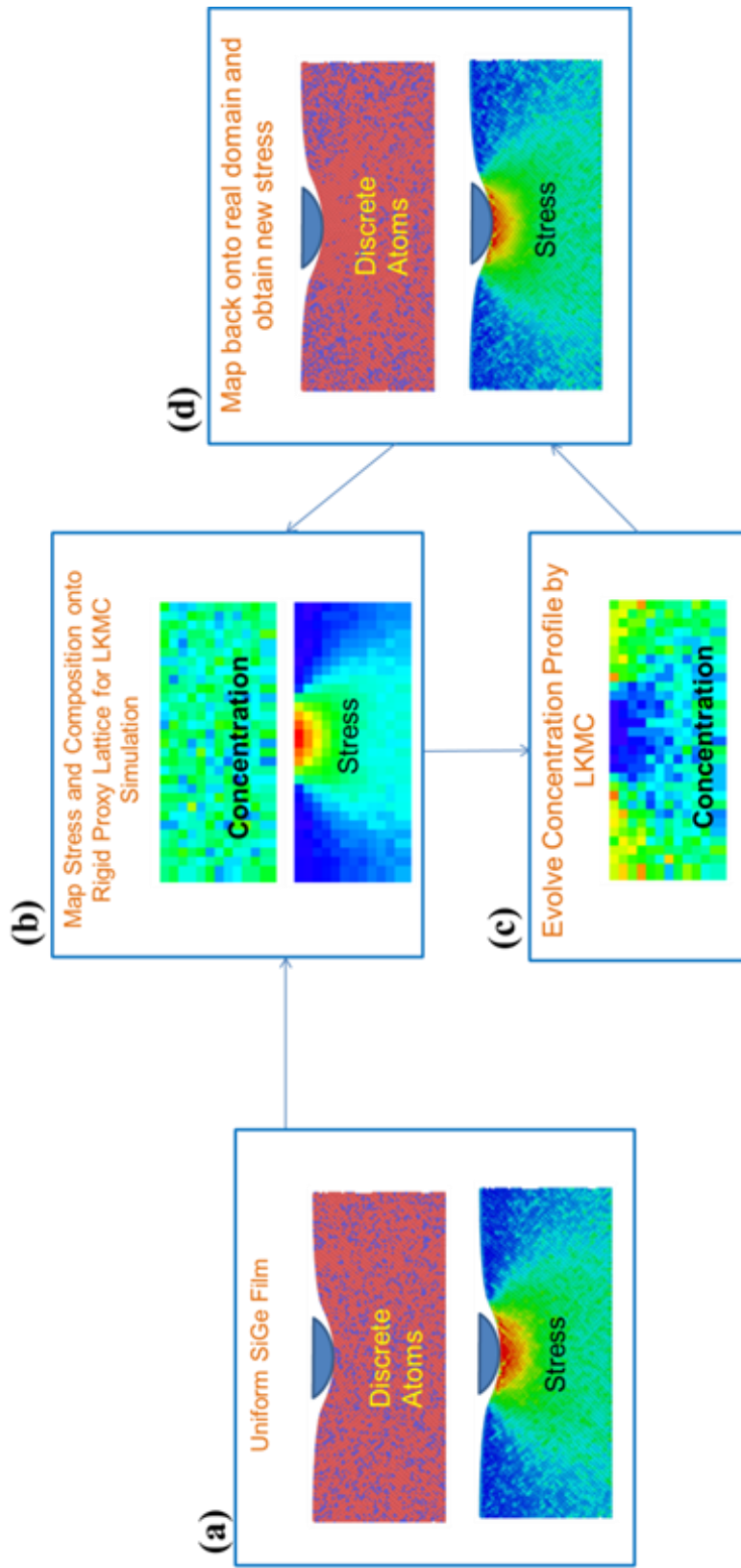


Figure 4.4. Schematic of simulator algorithm using stress field computed from molecular statics. See text for details.

The atomistic domain measured 200 nm wide in the x -direction, 100 nm high in the z -direction, and 3 nm deep in the y -direction, representing a total of $\sim 3 \times 10^6$ atoms. The domain was both subjected to periodic boundary conditions in the x and y directions, and the bottom layer of atoms in the z direction is fixed. A cylindrical ‘wire’ indenter (infinitely long, with axis in y -direction) field pushed on an atom with a force equal to

$$F(r) = -K(r - R)^2, \quad (4.34)$$

where K is the force constant (taken to be $10 \text{ eV}/\text{\AA}^3$ in this work), r is the distance from the indenter axis to the atom, and R is the radius of the indenter (25 nm for the discussion in this section). No force acts outside the radius of the indenter, i.e., $F(r > R) = 0$. The indenter field is lowered into the film less than 0.05 nm between energy minimizations, a rate at which the results obtained were not sensitive to the exact lowering rate.

The maximum contact pressure is located at the center of the contact zone, and is equivalent to $-\sigma_{zz}$ at that point. To estimate the maximum contact pressure from an indented atomistic configuration, atoms were binned into 3 nm-wide annular segments centered below the indenter axis, each of width 0.5 nm. Note that the average atomistic $-\sigma_{zz}$ in each bin is only weakly dependent on the bin dimensions. As shown in Figure 4.5, the binned atomistic $-\sigma_{zz}$ along the centerline below the contact zone varies quadratically with distance to the indenter axis. The quadratic fit (denoted by the solid line) was then used to extrapolate the contact pressure to the center of substrate-indenter contact zone (i.e., at the point of contact between the indenter and substrate), where the

maximum contact pressure is expected. The average of the extrapolation using the two annular region sizes was taken to be the maximum contact pressure value.

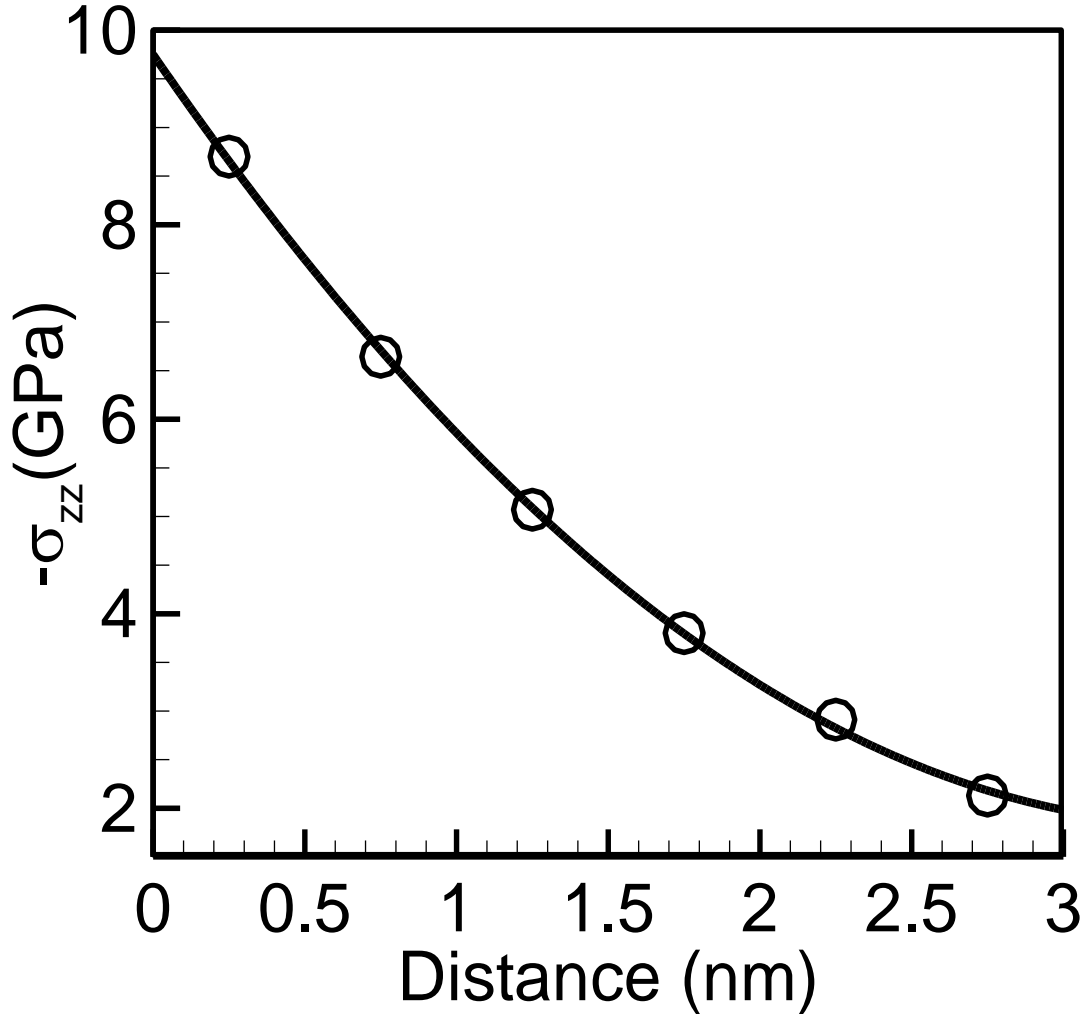


Figure 4.5. Binned atomistic pressure (circles) and quadratic fit (line, $R^2 > 0.999$) as a function of distance normal to the contact point between the 50-nm-diameter cylindrical indenter and substrate, predicted by quasi-static indentation of a $\text{Si}_{0.8}\text{Ge}_{0.2}$ slab. The annular segments used to bin the pressures are 3 nm wide (centered below the indenter) and 0.5 nm thick. The σ_{zz} profile shown here corresponds to an indenter applied with a force per length of 6.57×10^{-8} N/nm.

Maximum contact pressures obtained from indented atomistic configurations are shown as a function of applied indenter force-per-unit length in Figure 4.6 (red line). The effective indenter Young's modulus, $E_{ind} = 450$ GPa, is then extracted by matching the atomistic contact pressure data to a finite element model using the anisotropic elastic properties of the Tersoff potential (See Table 4.3; Poisson's ratio, ν , for the indenter was chosen to match Tersoff predicted properties for silicon). The finite element analysis is performed by imposing a body force on the indenter, and then solving the stress problem using plane strain analysis (i.e., infinite in the y -direction). Note that the continuum estimate for the maximum contact pressure begins to deviate from the atomistic simulation results above about 15 GPa, but show nearly perfect agreement up until that point.

Table 4.3. Elastic constants for $\text{Si}_{0.8}\text{Ge}_{0.2}$. Tersoff potential values for film and Poisson's ratio of indenter taken from ref. [94]

Material	C_{11} (GPa)	C_{12} (GPa)	C_{44} (GPa)	Young's Modulus (GPa)	Poisson's Ratio
$\text{Si}_{0.8}\text{Ge}_{0.2}$	147.4	73	69.4	99	0.33
Indenter				450	0.35

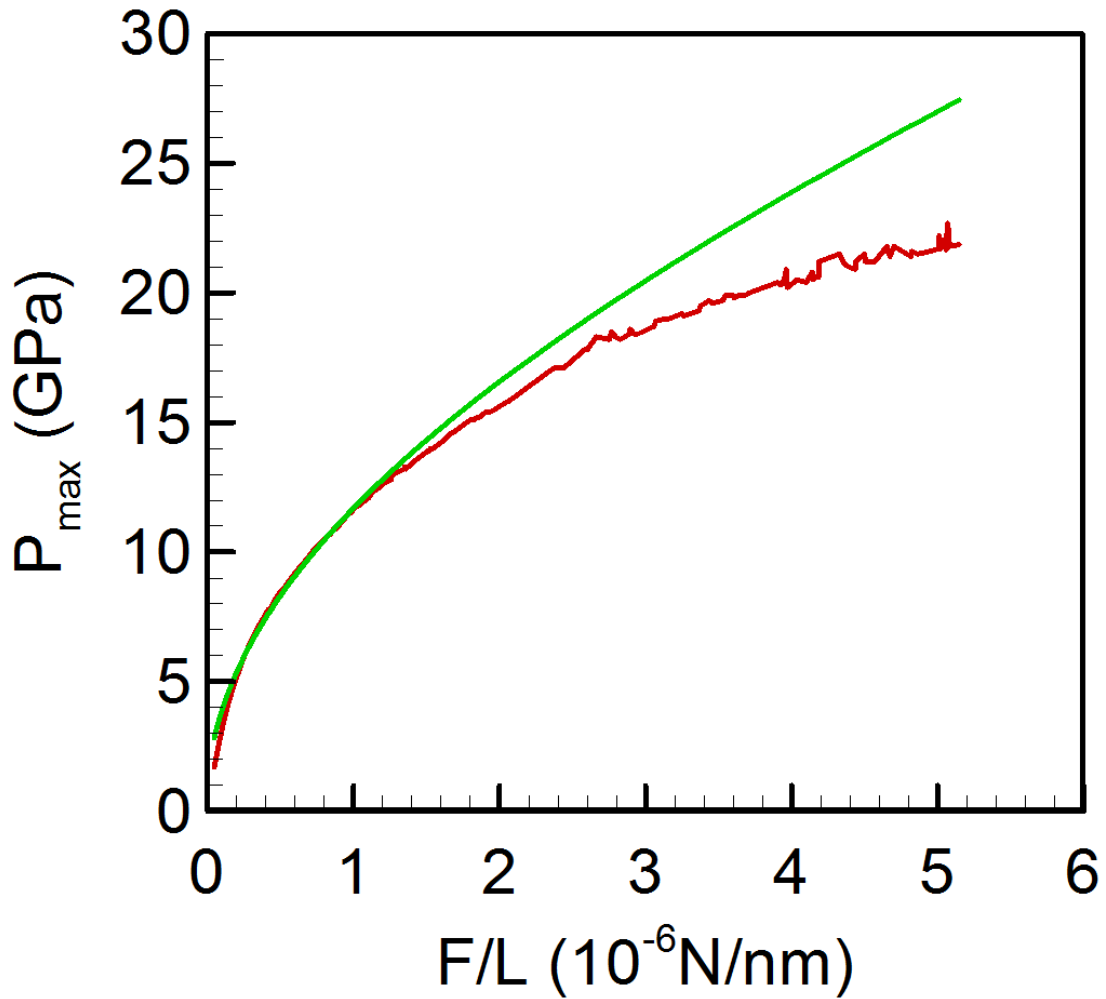


Figure 4.6. Maximum contact pressure obtained from energy minimization of an atomistic model (red line), along with the continuum analysis fit to the data (green line), for the indentation of a $\text{Si}_{0.8}\text{Ge}_{0.2}$ film using a 25 nm (radius) cylindrical indenter. See text for details.

4.4 Simulation Results

Using molecular statics calculations to calculate the stress field proved extremely computationally costly; indenting to 15 GPa of maximum contact pressure required ~1600 CPU-hours. Given the computational costs associated with solving for stress fields via molecular statics, all simulation results presented in the remainder of the thesis are based on the continuum stress field calculations described in Section 4.3.3.

Shown in Figure 4.7(a) is an example plane strain stress field (σ_{zz}) generated by an infinite cylindrical wire indenter with diameter 80 nm, assuming isotropic mechanical properties of $\text{Si}_{0.8}\text{Ge}_{0.2}$, along with the mesh used to generate the stress field (Figure 4.7(b)). Note that the stress field is mapped onto the undeformed (LKMC) domain. The $\text{Si}_{0.8}\text{Ge}_{0.2}$ film dimensions, which were also used for all LKMC wire indenter simulations, are 210.3 nm in the x -direction (corresponding to 384 $\text{Si}_{0.8}\text{Ge}_{0.2}$ unit cells with lattice parameter 0.5476681 nm [73]) and 157.7 nm in the z -direction (288 unit cells). In Figure 4.7(c), the maximum contact pressure ($-\sigma_{zz}$ at the center of the contact zone) is shown as a function of indenter force per unit length of the cylindrical indenter for three calculations. The anisotropic case is shown by the blue line, the corresponding isotropic case is shown in green, and the result of a Hertzian contact analysis is shown by the black dashed line: The Hertz model requires an effective modulus, E_r , which is defined according to the relationship

$$\frac{1}{E_r} = \frac{1-\nu_{\text{Si}}^2}{E_{\text{Si}}} + \frac{1-\nu_{\text{SiGe}}^2}{E_{\text{SiGe}}}, \quad (4.35)$$

Using the values in Table 4.2, $E_r = 69$ GPa. According to the Hertz model, given a force F , for a sphere with radius R , the maximum contact pressure, P , located at the center of the contact zone, is given by

$$P = \left(\frac{6FE_r^2}{\pi^3 R^2} \right)^{1/3}. \quad (4.36)$$

For a cylinder of length L and radius R ,

$$P = \left(\frac{FE_r}{L\pi R} \right)^{1/2}. \quad (4.37)$$

For maximum contact pressures less than about 10 GPa all three cases are in excellent quantitative agreement. Slightly larger deviations are visible as the maximum contact pressure is increased to 20 GPa, but these are generally less than about 5%, justifying the use of the isotropic elasticity assumption.

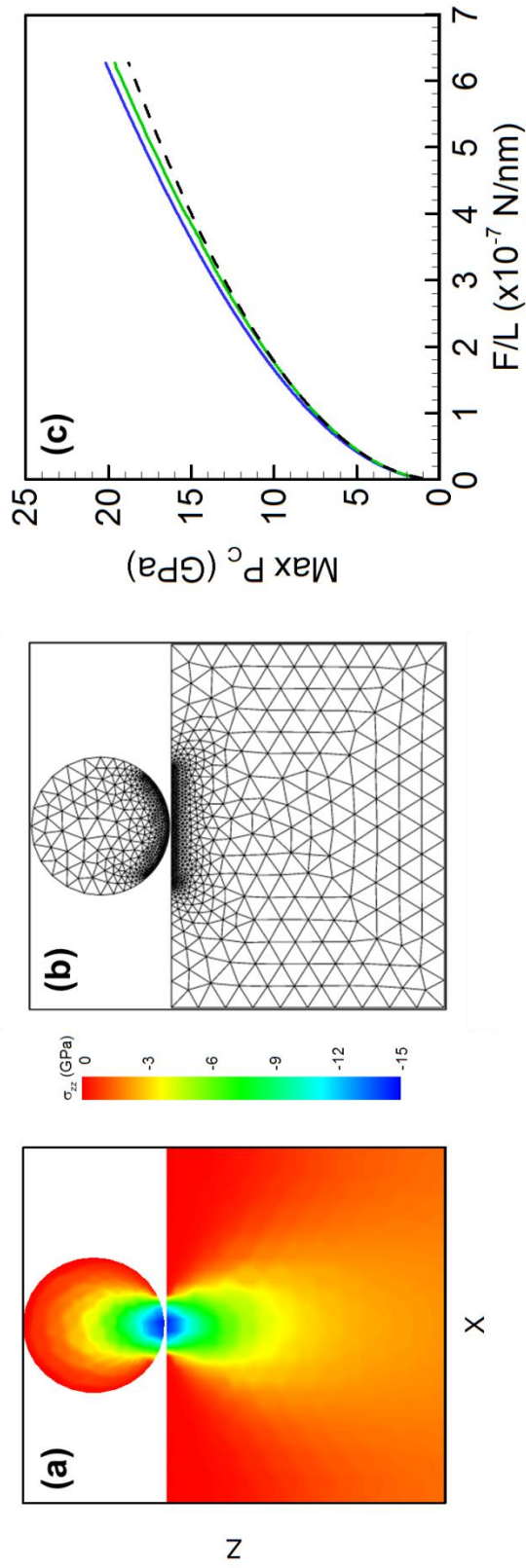


Figure 4.7. (a) Stress (σ_{zz}) in the xz -plane generated by an infinite (in y) cylindrical wire indenter of diameter 80 nm, corresponding to a maximum contact pressure of 15 GPa, mapped onto the undeformed domain. Result from plane strain calculation assuming isotropic elasticity. (b) FEM mesh used to generate the stress field in (a) (c) Indenter force versus maximum contact pressure for 80 nm-diameter, infinitely long, cylindrical indenter against $\text{Si}_{0.8}\text{Ge}_{0.2}$. Blue line – anisotropic elasticity, green line – isotropic elasticity, black dashed line – Hertz contact model.

Our first simulations were designed to mimic the experimental conditions reported in Chapter 2. Briefly, an array of spherical indenter tips (See Figure 4.8(e)), 80 nm in diameter and 200 nm apart in pitch, was indented to maximum contact pressures of 20-45 GPa at temperatures ranging from 900-1000 °C. We note here that compositional analysis was only performed for cases in which the maximum contact pressure was above ~35 GPa, which is generally higher than the situations considered here computationally. In fact, such high indenter forces are generally undesirable because of the risk of plastic deformation in the film, and because of damage to the indenter array as well as the film surface. Nonetheless, these cases were used for the imaging and compositional analysis because the surface damage served as a ‘marker’ for the indenter locations.

Shown in Figure 4.8(a,b) are Ge concentration profiles in an initially uniform $\text{Si}_{0.8}\text{Ge}_{0.2}$ domain predicted by LKMC simulation following three hours of thermal annealing at 1000 °C under the action of a spherical 80 nm-diameter indenter. For all spherical indenter simulations, we employed an LKMC domain with dimensions 210.3 nm (384 unit cells) \times 210.3 nm (384 unit cells) \times 157.7 nm (288 unit cells) in x , y , and z , respectively. Shown in snapshot (a) is the composition for the case where the maximum contact pressure is 9 GPa, while (b) corresponds to a maximum contact pressure of 35 GPa. Shown in panels (c,d) are the corresponding applied stress fields. Computed Ge concentration profiles along the x -direction are shown in Figure 4.8(f) for the top layer of LKMC cells for the two indenter cases, as well as an intermediate case where the maximum contact pressure was 21 GPa. Note that the profiles represent two periodic images of the actual LKMC domain placed side-by-side in the x -direction. Also shown in

Figure 4.8(f) are the results of compositional analysis from experiment at an estimated maximum contact pressure of 35 GPa.

Both the 21 GPa and 35 GPa simulations show essentially complete Ge depletion below the indenter, in agreement with the experimental profiles. However, discrepancies exist in the shape of depletion zone. While the 21 GPa simulation result appears to align well with the experimental profile in the center of the depletion zone, the 35 GPa case shows a wider zone of complete depletion. On the other hand, neither case shows the broad partial depletion zone exhibited in the experimental profile. There are several factors that may contribute to the discrepancy. First, the activation volume parameters discussed earlier, in section 4.2.1, which describe the dependence of diffusion rates on stress, are somewhat uncertain. Although, in principle, these parameters were validated in ref. [38] by comparison to interdiffusion experiments, the stresses considered here are far larger and uncertainty in these parameters could have more significant impact. Computational estimates of these parameters will be made in Chapter 6. Second, our assumption of a spherical indenter tip may not be accurate; it is difficult to determine the indenter tip shape from the image in Figure 4.8(e) and further analysis would be required to obtain a better representation. Next, it is possible that the high indenter forces lead to plastic deformation of the indenters, changing both the applied stress and the effective tip shape during the annealing process. Although no plastic deformation was observed by XTEM in the $\text{Si}_{0.8}\text{Ge}_{0.2}$ wafer, the large indenter force led to fusing between the indenter and $\text{Si}_{0.8}\text{Ge}_{0.2}$ substrate surface, which may be associated with some non-elastic deformation of the indenter. Again, additional analysis of the indenter array following the thermal anneal would be required to rule out this possibility. Lastly, we note that the

experimental measurements of composition are themselves subject to some uncertainty, which we estimate here to be less than about 1-2% in the reported composition, based on the EDS beam intensity calibration procedure reported in ref. [33]. Taken together, these uncertainties may suggest that a quantitatively perfect prediction of the exact shape of the depletion zone below each indenter may be an ill-posed goal, and that ‘coarser’ measures, such as the extent of depletion, and the overall collective pattern created by arrays of indenters, are better ones to target with simulations. Further experiments and corresponding simulations will be required to fully assess this issue.

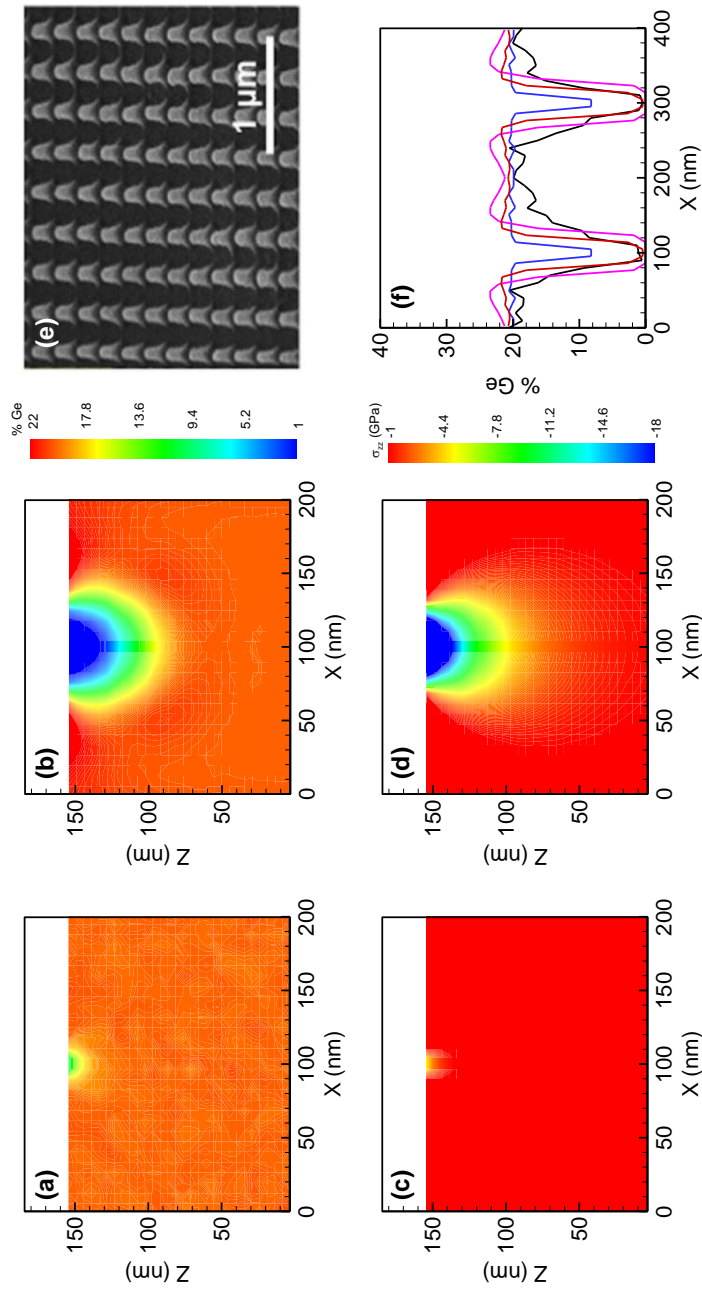


Figure 4.8. Simulated Ge concentration profiles (a,b) in an initially uniform $\text{Si}_{0.8}\text{Ge}_{0.2}$ film following 3 hours of thermal annealing at 1000 °C under stresses (c,d) induced by contact with an 80 nm-diameter spherical indenter with maximum contact pressure of 9 GPa (a,c) and 35 GPa (b,d). Note that (a)-(d) show an xz-plane of the three-dimensional simulation domain taken at the center of contact in y; this convention is used throughout the Chapter. (e) Scanning electron microscopy (SEM) image of the Si nanopillar indenter array used in the experiments reported in Chapter 2. (f) Near-surface (see text) Ge concentration as a function of x-position. Black line—experimental EDS measurement with maximum contact pressure ~ 35 GPa (based on Hertz contact model), blue line—LKMC with maximum contact pressure 9 GPa, red line—LKMC simulation with maximum contact pressure 21 GPa, purple line—LKMC with maximum contact pressure 35 GPa. All LKMC simulations performed with coarse cell size $L_{cell}=6.56$ nm. Note that the simulation profiles in (f) represent two copies of the actual simulation domain.

A more subtle discrepancy between the simulation and experimental compositional profiles in Figure 4.8(f) may be observed in the fluctuation amplitude, which is notably higher in the experimental case. The EDS technique used in Chapter 1 produces compositions that are averages over cubic domains at the surface that are estimated to be about $3\times 3\times 3\text{ nm}^3$ in size. On the other hand, the LKMC cubic cells used to generate the data in Figure 4.8 were chosen to be 6.56 nm on a side (corresponding to 12 unit cells of $\text{Si}_{0.8}\text{Ge}_{0.2}$ with lattice parameter 0.546681 nm), representing an approximately 10-fold increase in the number of atoms per averaging sub-volume. Our choice of $L_{\text{cell}}=6.56\text{ nm}$, which is used for all simulations in this Chapter, was largely predicated on computational cost; LKMC simulations with double the resolution in each dimension, i.e., $L_{\text{cell}}=3.28\text{ nm}$, take about 8 times longer to perform than those at the $L_{\text{cell}}=6.56\text{ nm}$ resolution, which was rather prohibitive for the fully three-dimensional LKMC simulations used in the spherical indenter cases. However, as shown in Figure 4.9 for a set of reference two-dimensional wire indenter simulations with different coarse cell sizes, the impact of cell size is largely restricted to the magnitude of compositional fluctuations and does not materially alter the nature of the compositional profile.

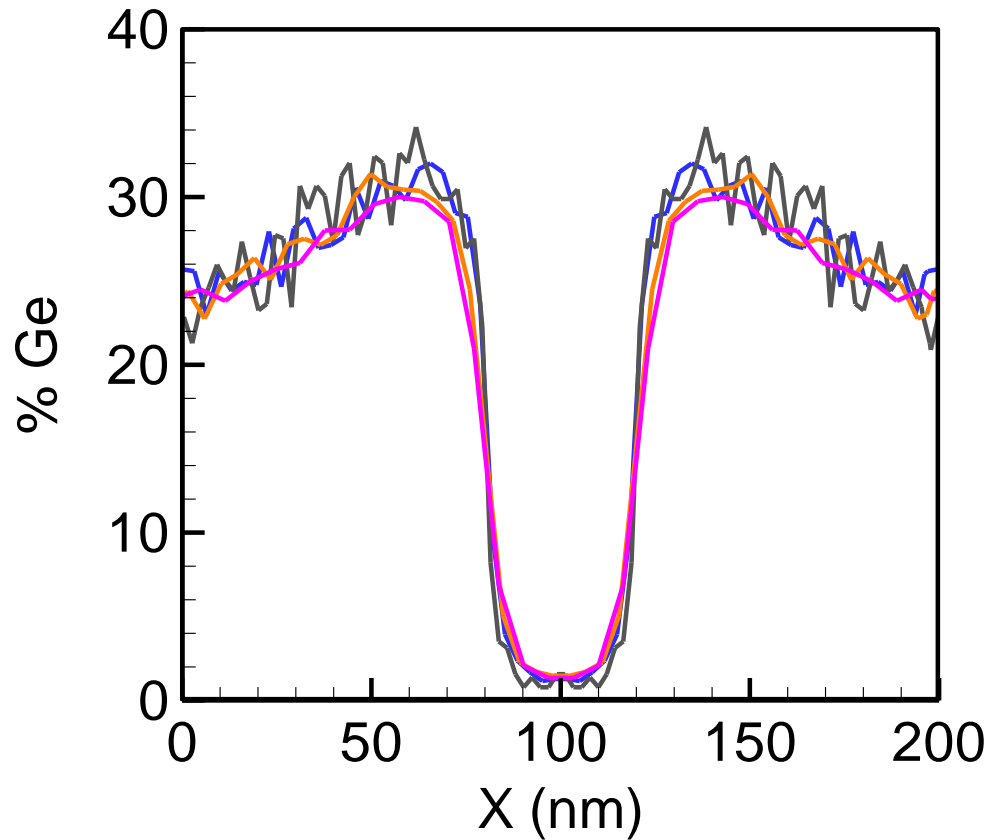


Figure 4.9. Ge concentration profiles in the top layer of coarse cells of a $\text{Si}_{0.8}\text{Ge}_{0.2}$ substrate subjected to a 80 nm-diameter cylindrical wire indenter following 3 hours of annealing at 1000 °C. The maximum contact pressure was 18 GPa. Individual profiles obtained with different LKMC coarse cell sizes: Gray— $L_{\text{cell}}=2.19$ nm (512 atoms/cell), blue— $L_{\text{cell}}=3.28$ nm (1,728 atoms/cell), orange— $L_{\text{cell}}=4.37$ nm (4,096 atoms/cell), pink— $L_{\text{cell}}=6.56$ nm (13,824 atoms/cell). Note that all wire indenter simulations are based on two-dimensional LKMC domains that are a single cell thick in the y-direction.

We also used the wire indenter case to test an important assumption that was introduced earlier, namely that the stress field does not need to be dynamically updated as the compositional redistribution takes place. Shown in Figure 4.10 are steady-state Ge concentrations (annealing time much longer than 3 hours) in the top layer of cells for the same conditions as those used to generate Figure 4.9. The black line shows the solution

using the elastic constants of the initial homogeneous $\text{Si}_{0.8}\text{Ge}_{0.2}$ material. The blue line shows the profile that results when the steady-state compositional field is used to compute consistent (spatially-varying) elastic constants and lattice mismatch and the simulation continued until steady-state. The fact that these profiles are essentially identical confirms that, at least for Si and Ge, the lattice strain and small differences in the elastic constants do not play qualitatively important roles in the compositional redistribution.

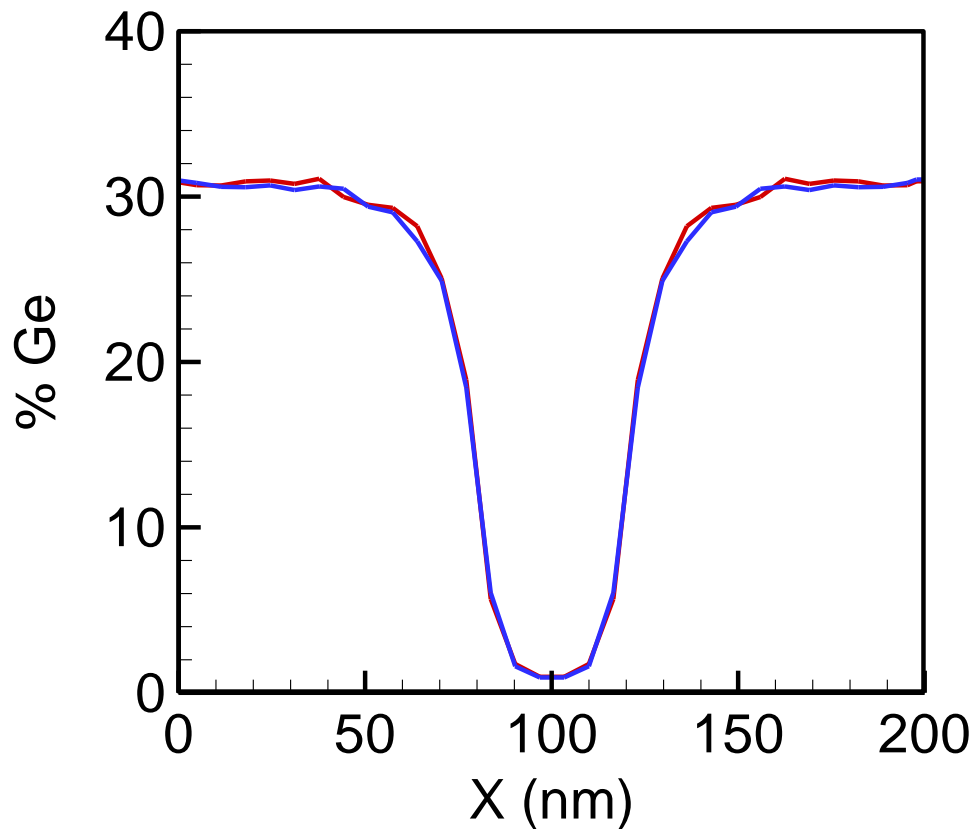


Figure 4.10. Steady-state Ge concentration profiles in top layer of LKMC cells of an initially uniform $\text{Si}_{0.8}\text{Ge}_{0.2}$ film subjected to an 80 nm-diameter wire indenter (maximum contact pressure of 18 GPa) and annealed at 1000 °C. Red line—elastic constants corresponding to initial (uniform) composition, blue line—with lattice mismatch and elastic constants corresponding to spatially-varying steady-state compositional profile.

Next, the dependence of the Ge depletion effect on the type of indenter was investigated. As shown in Figure 4.11, wire indenters lead to qualitatively different stress fields than those produced by spherical indenters. Most notably, more of the film is subjected to compression when indented using a wire indenter, making the smaller areas of zero compression in the near-surface regions adjacent to the contact zone attractors for Ge atoms, resulting in enhanced Ge concentrations above the background 20% value. Consequently, Ge profiles resulting from wire indentation show a stronger Ge concentration difference at the edge of the depletion zone, which may be useful in the context of QCS design where large concentration changes across small distances are required for confinement and isolation. Although not shown here, upon further annealing the region of enhanced Ge concentration gradually continues to broaden and eventually extends across nearly the entire near-surface region.

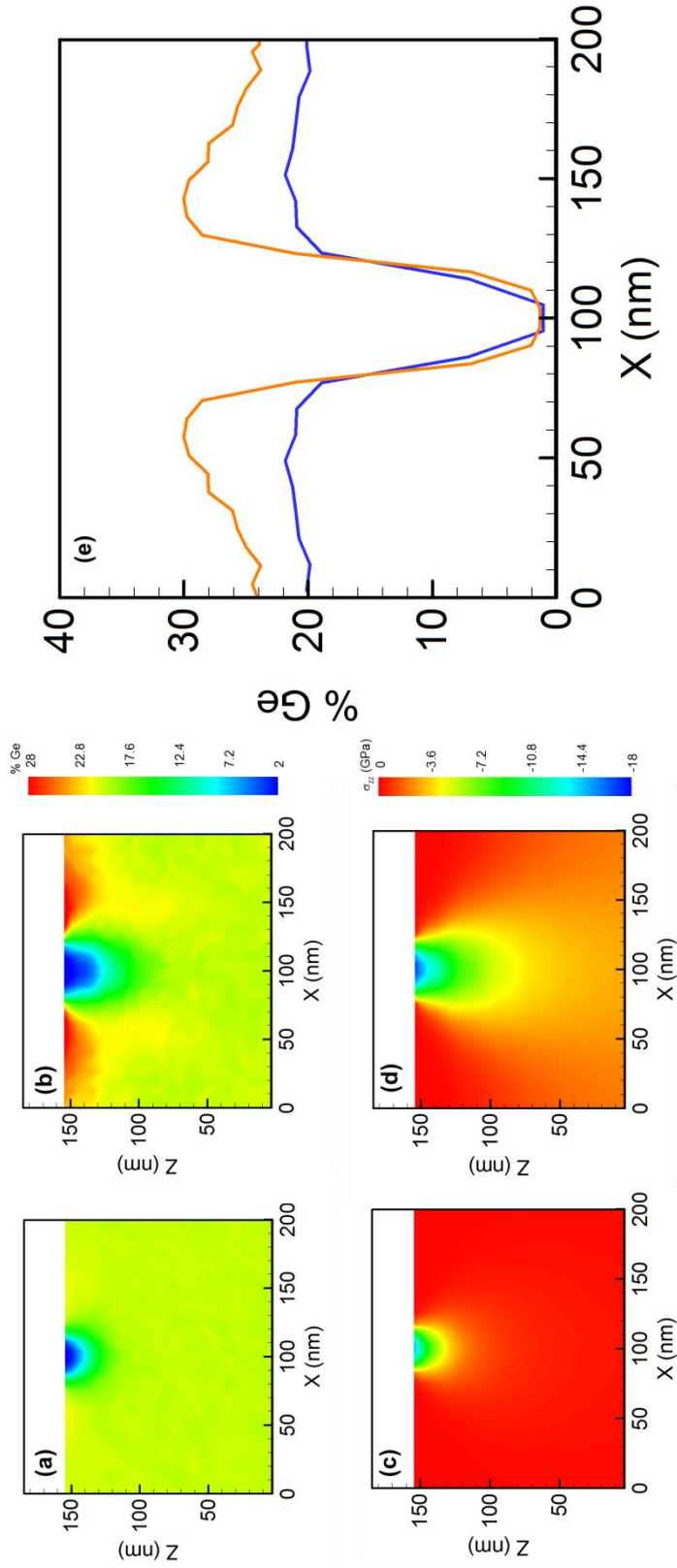


Figure 4.11. Simulated Ge concentration profiles (a,b) in an initially uniform $\text{Si}_{0.8}\text{Ge}_{0.2}$ film following 3 hours of thermal annealing at 1000 °C under stresses (c,d) induced by contact with (a) an 80 nm-diameter spherical indenter, and (b) an 80 nm-diameter wire indenter, both with maximum contact pressure of 18 GPa. (e) Compositional profiles in the top layer of cells; orange line—wire indenter, blue line—spherical indenter. As noted earlier, the spherical indenter LKMC simulation results represent an xz -slice taken from a three-dimensional domain, while the wire indenter simulations are two-dimensional.

In fact, any practical approach for QCS engineering in the present context will require the capability of enhancing Ge in localized regions. Generally speaking, ideal quantum confinement structures are comprised of sharply delineated regions of a lower bandgap material, isolated by surrounding material with a higher electronic bandgap [95]. Given that the bandgap of SiGe decreases with Ge composition [96], a QCS-relevant configuration requires a high Ge concentration region surrounded by a lower Ge concentration. The stress patterning approach described here, generally tends to push Ge atoms away because the applied stress is mostly compressive in nature. Building on the result in Figure 4.11, we simulated the Ge distribution in a system where two wire indenters were placed 105 nm apart, rather than the 210 nm pitch used in the previous simulations. As shown in Figure 4.12, this configuration (orange line) leads to well-defined regions of Ge enhancement (over 40%) separated by almost completely Ge-depleted regions by very high compositional gradients. By contrast, the 210 nm pitch configuration (blue line) only produces a peak Ge concentration of 30%, and which is non-uniform across the Ge-enhanced region. These results provide preliminary evidence for the ability of the stress-mediated patterning approach to produce technologically relevant compositional configurations. Systematic optimization of indenter configuration is tantamount to solving an inverse problem in which the indenter geometry, along with other processing parameters, are found for a given desired (and feasible) compositional configuration; this is the subject of Chapter 5.

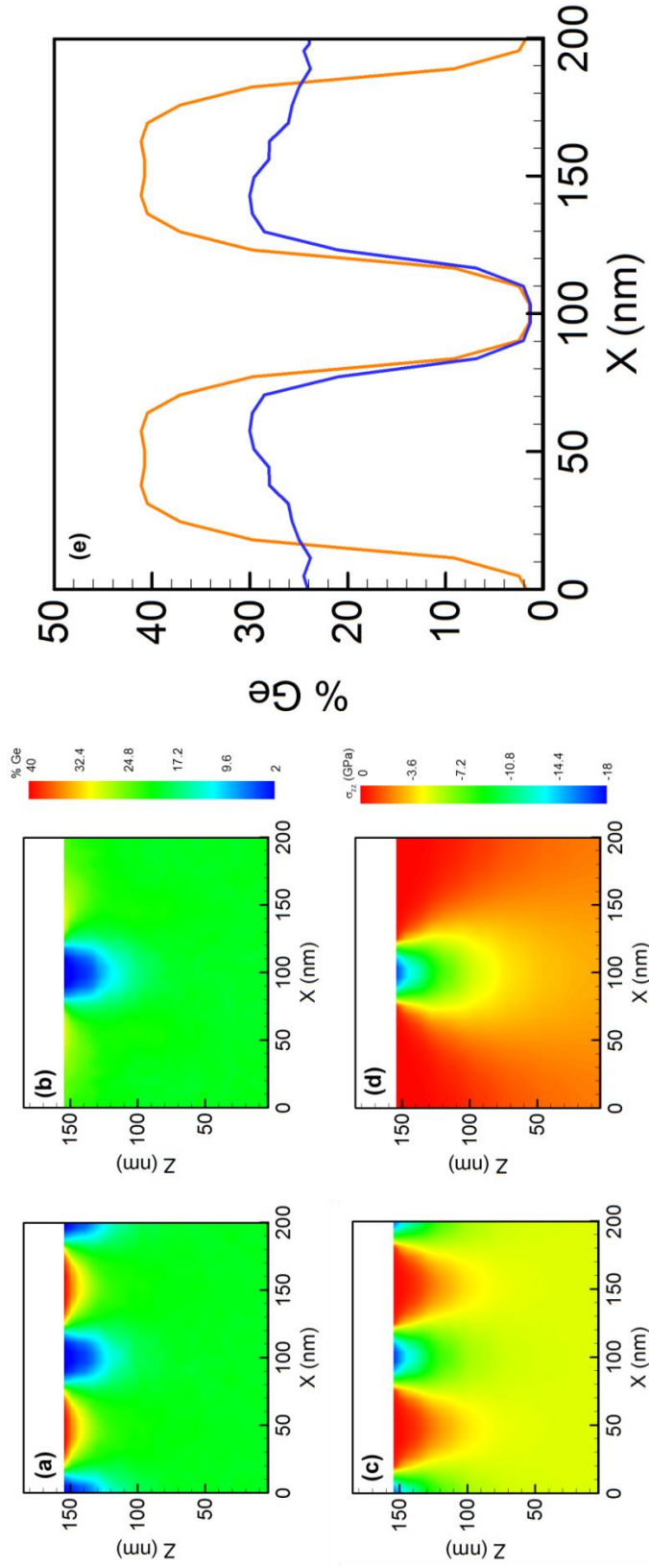


Figure 4.12. Ge concentration profiles (a,b) in an initially uniform $\text{Si}_{0.8}\text{Ge}_{0.2}$ film following 3 hours of thermal annealing at $1000\text{ }^\circ\text{C}$ under stresses (c,d) induced by contact with an 80 nm-diameter wire indenter (maximum contact pressure 18 GPa) with inter-wire spacing of (a,c) 105 nm, and (b,d) 210 nm. (e) Compositional profiles in the top layer of cells; orange line—105 nm pitch, blue line—210 nm pitch.

Finally, we address the dynamics of stress-mediated Ge redistribution. The temporal evolution of the Ge profile during thermal annealing at 1000 °C under applied stress is shown in Figure 4.13 for the case of an 80 nm-diameter spherical indenter exerting 21 GPa maximum contact pressure. As shown by the two-dimensional compositional profiles (a-d) and the near-surface compositional scans (e), three hours is sufficient for the Ge compositional distribution to reach steady state, at least in the region of strong Ge depletion. The impact of annealing temperature on the redistribution dynamics was analyzed by considering the Ge evolution due to the application on an 80 nm-diameter wire indenter (maximum contact pressure of 18 GPa). As expected, the diffusion-mediated process follows Arrhenius behavior in which the time to reach the patterned configuration shown in Figure 4.14(a), was found to obey an Arrhenius relationship of the form $t = a \exp(b/T)$. The best fit is shown in Figure 4.14(b): $a = 1.5 \times 10^{-14}$ minutes and $b = 4.7 \times 10^4$ K. In practice, increased redistribution dynamics with higher temperatures must be balanced against material softening and a higher chance for plastic defect formation. We also note that point defect diffusivity is also strongly influenced by stress as discussed in the Section 4.2.1, and the activation volume parameters reported in eqs. (4.14) also are expected to have substantial effects on the patterning timescale. A limited sensitivity analysis with respect to these parameters was performed in which all 4 parameters were scaled by a single constant ranging from 0.75-2.0. The results (not shown) indicate that while the final Ge distribution is unaffected by the activation volume scaling, the timescale for patterning is, unsurprisingly, quite

sensitive to these parameters. The large uncertainty in these parameters will be addressed in Chapter 6.

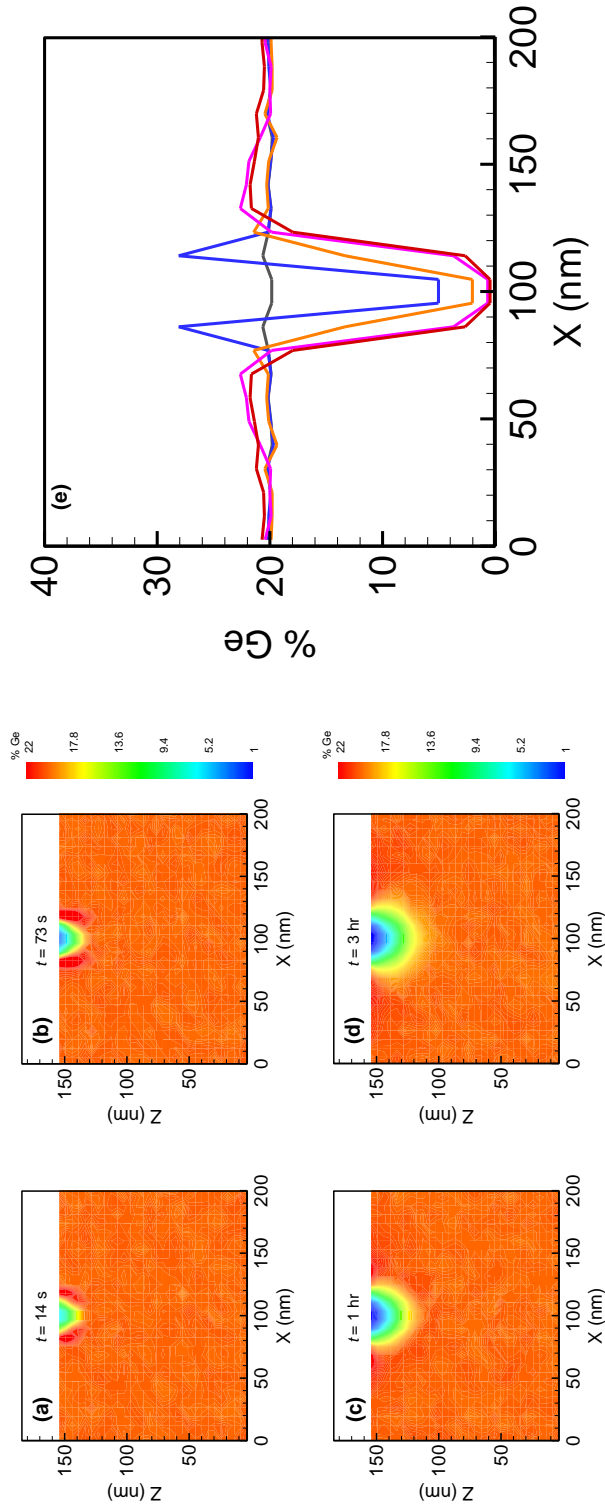


Figure 4.13. (a)-(d) Sequence of snapshots of Ge concentration fields in SiGe film during annealing at 1000 °C under a spherical indenter of diameter 80 nm and maximum contact pressure 21 GPa, (e) Ge concentration profile in top layer of LKMC cells after 0s (grey), 14s (blue), 74s (orange), 1 hr (pink) and 3 hours (red).

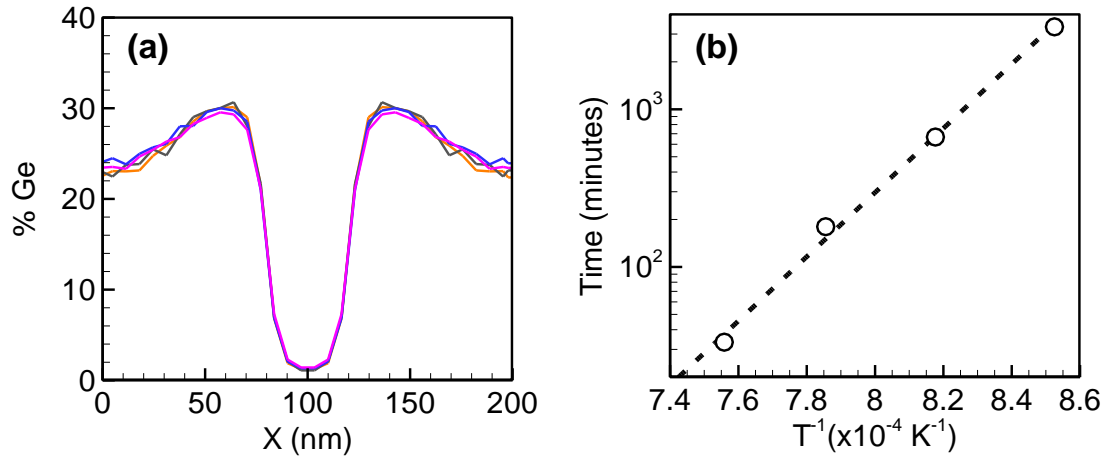


Figure 4.14. (a) Ge concentration in the top layer of LKMC cells in an initially uniform $\text{Si}_{0.8}\text{Ge}_{0.2}$ film following annealing for variable times under the action of a 80 nm-diameter wire indenter (maximum contact pressures 18 GPa). Annealing times are 30 min at 1050°C (pink), 180 min at 1000°C (blue), 700 min at 950°C, and 3300 min at 900°C. (b) Arrhenius plot of annealing time to reach set patterning extent versus inverse temperature; circles are simulation data, dashed line is the Arrhenius fit.

4.5 Conclusions

The ability to compositionally pattern large-area thin films comprised of solid-solution alloys (e.g., SiGe) using elastic fields generated by ordered arrays of nano-indenters presents an exciting opportunity to engineer laterally organized, three-dimensionally quantum-confined structures. The essential idea behind this approach is appealingly simple—the larger atomic species in the alloy will be driven away by diffusion from regions of compression immediately below the indenters, creating lateral, as well as vertical, compositional gradients. Although ‘proof-of-principle’ experimental demonstrations have been successful, it is immediately obvious that optimization of stress-driven compositional patterning requires the simultaneous consideration of

numerous process parameters and constraints. Example parameters include indenter shape, pitch and array geometry, annealing temperature-time history, and initial alloy composition, to name a few. Constraints include the formation of plastic defects such as dislocations if the stresses created by the indenters are too high. Such defects may pose irreversible sinks for point defects, hindering the patterning process. Given the challenges associated with characterization of structure and composition at the nanoscale in such materials, a predictive model for stress-driven compositional patterning is highly desirable for carrying out systematic studies.

The goals of this work are two-fold. First, it was shown that such a model can indeed be constructed, even though interdiffusion in SiGe is surprisingly complex given the strong dependence of point defect diffusion (which is the primary transport mediator) on time- and space-varying temperature, composition and stress. Second, we used the model to investigate the impact of some of the process parameters on the resulting compositional patterns. Most importantly, we were able to demonstrate that it is possible to enhance, as well as deplete, Ge concentrations. In its simplest interpretation, the stress-driven compositional patterning approach described here provides ‘one-way’ control, in which the larger Ge atoms are driven away from localized regions of high compressive stress below each indenter, leaving behind locally Si-enriched regions embedded in the SiGe background. Unfortunately, such configurations are not useful as QCSs because quantum confinement requires that the smaller bandgap region (high Ge content) be embedded in a larger bandgap environment (low Ge content). However, using wire-like indenters that are closely spaced, we found that localized regions of zero compression can be created in the near-surface region of the alloy substrate, which then attract Ge atoms

and create well-defined regions in which the Ge content is above the background alloy composition. While these results are somewhat preliminary, they do suggest that optimization of the approach could lead to very useful compositional configurations.

Chapter 5. Generating Ge Quantum Dots Using Complex Nanoindenter Geometries and Annealing Schedules

5.1 Introduction

In Chapter 2 and Chapter 4, we demonstrated that annealing a $\text{Si}_{1-x}\text{Ge}_x$ wafer subjected to spatially varying stress fields from an indenter array can lead to compositional segregation in the near-surface region of the film. To summarize, we applied an array of Si nanoindenters to an $\text{Si}_{1-x}\text{Ge}_x$ thin film, creating a periodic stress field in the near surface region of the film. Annealing the stressed film at high temperatures lead to a compositional redistribution of Si and Ge atoms commensurate with the applied stress field such that the larger Ge atoms preferentially diffused away from the regions of compression.

An inherent limitation of this approach is that we are restricted to applying compressive stress fields in the region of the film near the indenters. Since Ge is larger than Si, Ge atoms preferentially migrate away from compression, which leads to regions of enhanced Si near the center of indentation. However, from a quantum confinement perspective, we desire the opposite general configuration, i.e., localized regions of enhanced Ge concentrations embedded in a background of lower Ge content. This requirement is driven by the fact that the bandgap of SiGe decreases with Ge content because Ge has a smaller bandgap than Si [97]. Previous work in the literature observed that Si-capped, Ge QCSs that measure ~ 160 nm laterally and ~ 20 nm in height are small enough laterally to begin to exhibit in-plane confinement effects, while the size of the structures in the vertical direction leads to confinement effects an order of magnitude higher [98]. Furthermore, in bulk $\text{Si}_{1-x}\text{Ge}_x$, the band gap decreases by more than 15% as x

increases from 0 to 0.85, while it decreases roughly the same amount as x increases from 0.85 to 1 [97]. Thus, we aim to generate small (< 100 nm), nearly pure Ge features (Ge concentration in SiGe $> 85\%$) embedded in lower Ge concentration SiGe.

The focus of this Chapter is the study of the complex parameter space that defines the stress transfer process introduced in the prior Chapters. In particular, we report on the impact of geometrically complex indenter arrays, temporally variable stress fields during annealing, and substrate composition. We first present an overview of additional methodological advances required to tackle the larger simulation domains and then discuss various processing strategies for creating potentially useful compositional patterns. Finally, we conclude with potential applications for annealing under the influence of complex stress states.

5.2 Lattice Kinetic Monte Carlo (LKMC) Model

In Chapter 4, a lattice kinetic Monte Carlo (LKMC) framework was developed to describe point defect mediated interdiffusion of Si and Ge in $\text{Si}_{1-x}\text{Ge}_x$ alloys subjected to spatially varying stress fields. Point defect diffusion in unstrained SiGe is well described by a vast literature [38]. We included the impact of strain by modifying the diffusivities of defects via the formalism of Aziz [32], and we parameterized gradient effects using molecular statics calculations.

Recall that the move basis for the LKMC algorithm is an exchange of a Si atom and Ge atom between neighboring cells, the rates of which are

$$\begin{aligned}
r_{Ge_1 \rightarrow Si_2} &= \frac{n_{tot}}{L_{cell}^2} \sum_{A=I,V} \left(\frac{P_{Ge_1}^A}{f_A} \left(1 - \frac{P_{Ge_2}^i}{f_A} \right) f_A D_A \frac{C_A}{C_a} \right) \\
r_{Si_1 \rightarrow Ge_2} &= \frac{n_{tot}}{L_{cell}^2} \sum_{A=I,V} \left(\frac{P_{Ge_2}^A}{f_A} \left(1 - \frac{P_{Ge_1}^A}{f_A} \right) f_A D_A \frac{C_A}{C_a} \right),
\end{aligned} \tag{5.1}$$

where L_{cell} is the distance between the centers of the two cells (I and 2) participating in the exchange and n_{tot} is the number of atoms in each cell. The correlation factor for atomic motion resulting from defect jumps, f_I and f_V , are taken to be 0.7 and 0.5, respectively [38]. Point defect transport capacities ($D_A C_A$), normalized by the atomic site density, $C_a \sim 5 \times 10^{22} \text{ atoms/cm}^3$, were obtained from the fitting of experimental data taken at different compositions and temperatures, modified according to the local stress field [32, 38]. The probabilities of picking either Si or Ge within a cell, P^A , are functions of composition, temperature, and compositional/stress gradients between the two cells participating in the exchange. Additional details may be found in Chapter 4.

5.2.1 “Net event” LKMC Framework

In order to facilitate larger scale simulations at finer resolution, we adopt the “net rate” framework introduced by Snyder et al. [52]. This framework, in general, can be useful for any KMC simulation described using a move basis comprised of pairs of reversible reactions. Exchanges between two neighboring cells, by definition a reversible reaction pair, are considered as one “net” event:

$$r_{net,1 \leftrightarrow 2} = \left| r_{Ge_1 \rightarrow Si_2} - r_{Si_1 \rightarrow Ge_2} \right|. \tag{5.2}$$

Once a net event is selected, the direction of the exchange is determined by the sign of $r_{Ge_1 \rightarrow Si_2} - r_{Si_1 \rightarrow Ge_2}$; if $r_{Ge_1 \rightarrow Si_2} > r_{Si_1 \rightarrow Ge_2}$ a Ge from cell 1 is exchanged with an Si from cell 2, and vice versa. As shown in Figure 5.1, this approximation minimally impacts the extent of patterning, but entirely dampens the noise of the solution [52]. Figure 5.1(a) shows the steady-state compositional fluctuations in a uniform 20% Ge film without the impact of externally applied stress. In the net event case, the fluctuations are entirely dampened. To illustrate the impact of net event on a typical LKMC simulation, Figure 5.1(b) shows one of the cases from Chapter 4 with and without using the net event construct. The solution is essentially unchanged by the net event approximation. Note that impact of noise dampening is low because the relatively large cells ($6 \times 6 \times 6 \text{ nm}^3$ LKMC cells) correspond to a resolution at which fluctuations are quite small—as shown in Figure 5.1(a) the compositional fluctuations scale inversely with the number of atoms in each cell.

The magnitude of the computational gains associated with net event depend on the “stiffness” in the event rates; If there are some fast events and a large number of slow events, the sum of the rates (and, hence, the time step (see Chapter 3)) is dominated by the fast events. For the systems considered in this Chapter, the computational performance gains seen are quite substantial: the net event method requires $O(10^2)$, on average, less CPU time than the full LKMC methodology. Given that the net event solution minimally deviates from the full LKMC solution, the huge computational gains associated with net event LKMC, and the minimal impact on the noise observed at relevant cell sizes using the full model, our choice of using net event LKMC is justified for all the results presented in this Chapter.

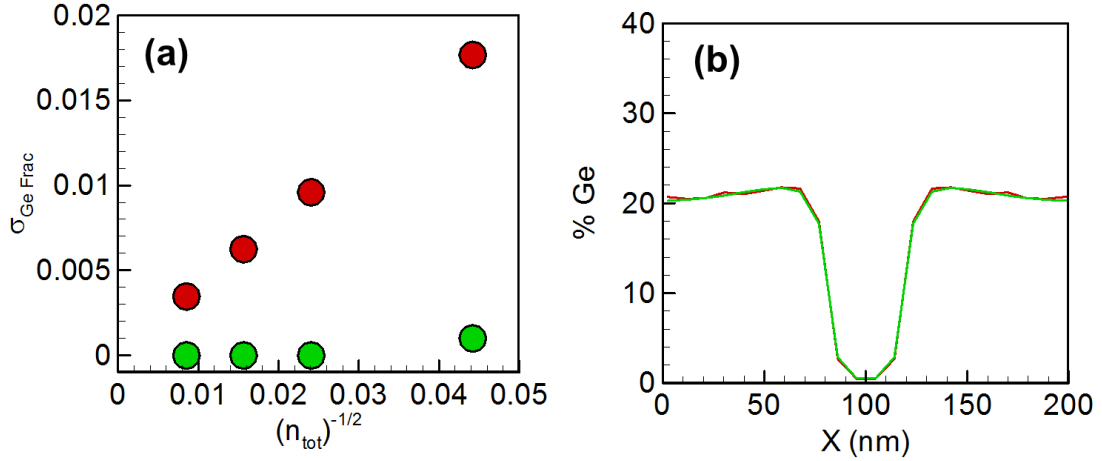


Figure 5.1. (a) Standard deviation of Ge concentration in uniform 20% Ge film with no externally applied stress field. (b) Top cell concentration profile of Ge concentration fields in SiGe film during annealing at 1000 °C under a spherical indenter of diameter 80 nm and maximum contact pressure 21 GPa (See Chapter 4). Green is net event LKMC and red is full LKMC.

5.2.2 Multiresolution LKMC

We have also extended the LKMC framework by introducing a variable grid resolution (i.e., variable cell size) capability, in order to locally increase resolution as desired without incurring the overhead of increased resolution everywhere. In regions of constant cell size, the move basis and rate expressions described in the “net rate” framework remains the same (Figure 5.2(c)). For exchanges across boundaries, as depicted in Figure 5.2(b), the four neighboring smaller cells are treated as one “composite cell.” The smaller cell within the composite cell that contains the atom participating in the exchange is chosen at random. The Vlachos group [55, 56] has derived rate expressions for LKMC operating on a variable grid, modifying the first term on the right in eqs. (5.1), as n_{tot} should be the average number of atoms in the composite cell and larger cell, and L_{cell} should be the distance between the center of the larger cell and the

center of the composite cell. The transport capacities in eqs. (5.1) are computed based on the weighted average of the composite cell and the larger cell.

A sample LKMC grid is shown in Figure 5.2(d). All LKMC domains had two layers of $L_{cell} = 3.28$ nm LKMC cells (1,728 atoms/cell) on the top surface in z , with $L_{cell} = 6.56$ nm LKMC cells (13,824 atoms/cell) beneath until the bottom surface, in an effort to enhance resolution in the near surface region. Periodic boundary conditions were imposed in the x - and y -directions, and no flux boundary conditions were imposed in the z -direction. The depth of all domains in the z -direction was 157.7 nm.

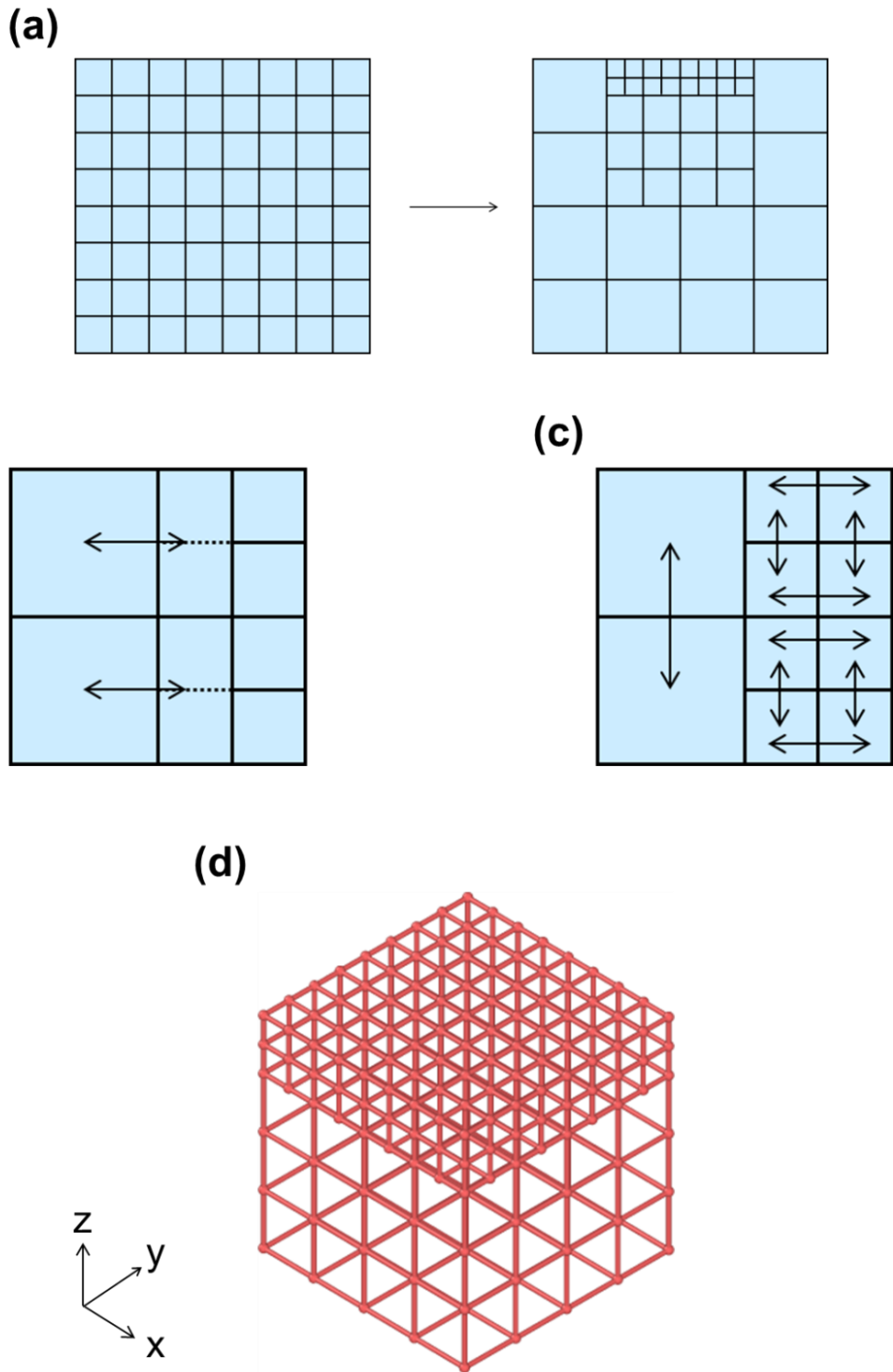


Figure 5.2. (a) schematic of changing entirely high resolution region of LKMC domain to variable resolution (b) schematic of exchanges between regions comprised of two different cell sizes (c) schematic of exchanges between equally size cells (d) sample LKMC grid. See text for details.

5.3 Continuum Stress Calculation

Stress fields in the SiGe film under the impact of indentation from an Si indenter were computed by solving a linear elasticity contact problem with the finite element method (FEM) using the COMSOL software package [90], as previously described in Chapter 4. To summarize, computing a solution to the linear elastic stress problem involves simultaneously solving the equilibrium equations,

$$\nabla \cdot \boldsymbol{\sigma} + \mathbf{b} = \mathbf{0}, \quad (5.3)$$

with $\boldsymbol{\sigma}$ being the stress tensor and \mathbf{b} being the body force (per volume) vector, the strain-displacement relationships,

$$\boldsymbol{\varepsilon}_{Total} = \frac{1}{2} [(\nabla \mathbf{u})^T + \nabla \mathbf{u}], \quad (5.4)$$

where $\boldsymbol{\varepsilon}_{Total}$ is the strain tensor and \mathbf{u} is the vector of displacements, and the constitutive relations,

$$\boldsymbol{\sigma} = \mathbf{C} : \boldsymbol{\varepsilon}_{Elastic}, \quad (5.5)$$

where \mathbf{C} is the stiffness tensor, all subject to boundary conditions. We note that due to compositional patterning in initially homogenous $\text{Si}_{1-x}\text{Ge}_x$, $\boldsymbol{\varepsilon}_{Elastic} \neq \boldsymbol{\varepsilon}_{Total}$, yielding additional relations, $\boldsymbol{\varepsilon}_{Elastic} = \boldsymbol{\varepsilon}_{Total} - \boldsymbol{\varepsilon}_{Misfit}$, where the spatially variable $\boldsymbol{\varepsilon}_{Misfit}$ tensor is,

$$(x_{initial} - x_{local}) \mathbf{I}, \quad (5.6)$$

with x being the Ge fraction [38].

Here, in order to consider non-two-dimensional and axisymmetric geometries, we solved the fully three-dimensional stress problem. A sample of the grid used to compute

stresses for all the studies in this Chapter is shown in Figure 5.3. The mesh was graded so that the resolution was increased at the top of the substrate and bottom of the indenter, i.e., in the vicinity of the contact zone. Sensitivity of the solution to the mesh is discussed in the following Section.

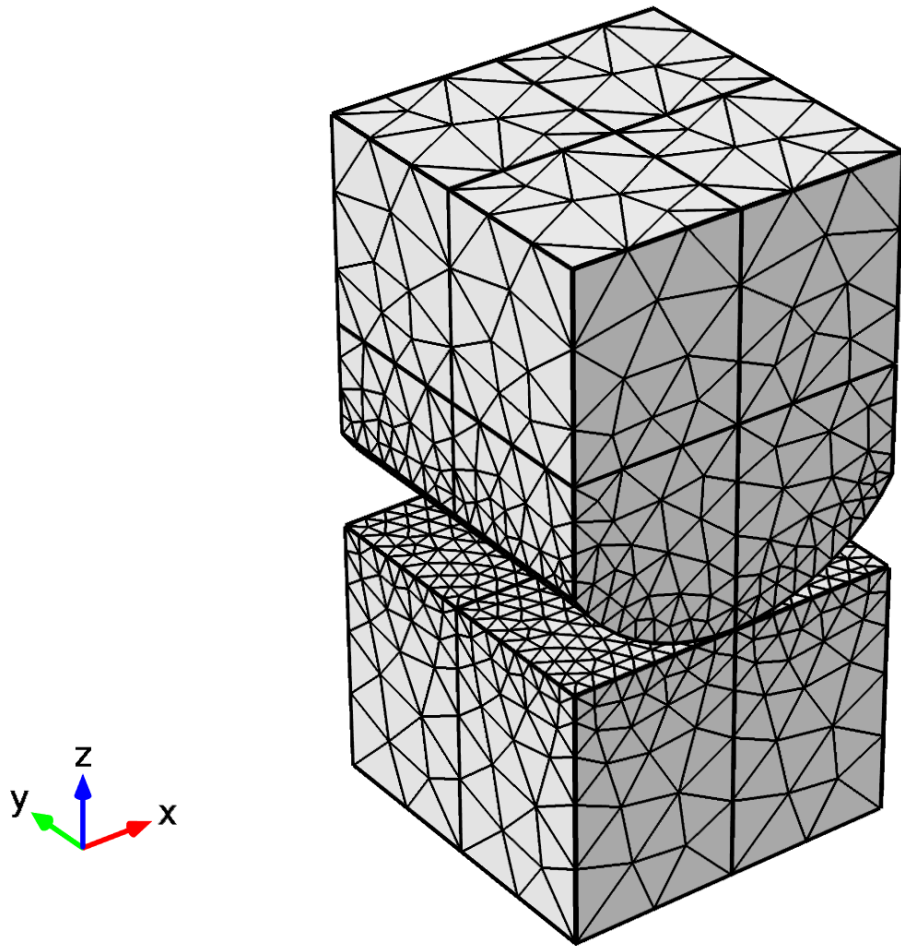


Figure 5.3. Example mesh and geometry used to solve stress problems in this Chapter.

Most of the studies presented in this Chapter were of a cubic-oriented indenter array. For these cases, in the substrate, we imposed periodic boundary conditions in lateral dimensions (x and y), the bottom z -boundary was fixed, and the top z -boundary was traction-free except in the contact region. For indenters, a specified displacement on

the top surface was applied, pushing it into the SiGe film, periodic boundary conditions were applied in x and y and traction free boundary conditions were imposed on the indenter tip, except in the contact region. Two symmetry planes were drawn through the central z axis (in x and y) of the domain in all cases to assist in convergence.

In a study on array patterns, however, we used a regular hexagonal substrate (Section 5.4.3). In these cases, the boundary conditions were identical to the cubic array, except that the periodicity was applied on the 3 pairs of opposing faces, as opposed to the x - and y - directions. In all cases, we used the full anisotropic stiffness tensor (with cubic symmetry) when solving the constitutive stress-strain relationship. The elastic constants used for Si and Ge were reported in Chapter 4, and we linearly interpolated between Si and Ge values to obtain the values for $\text{Si}_{1-x}\text{Ge}_x$. We assume that the elastic constants are invariant with respect to temperature, and we further assume that the stress solution does not need to be updated as the composition evolves, given the analysis in Chapter 4.

5.3.1 Analysis of Mesh Used During Stress Computation

The COMSOL software package was used to generate three-dimensional meshes for both the indenter and substrate, which were then used to solve the linear elasticity problem described in the beginning of Section 5.3. The mesh was graded so that the resolution was increased at the top of the substrate and bottom of the indenter, i.e., in the vicinity of the contact zone.

In Chapter 4, where only 2D stress solutions were used in all of the studies, a very fine mesh was used in all cases such that the answer was not sensitive at all to the exact

mesh resolution. In 3D, however, we were unable to use a mesh with such fine resolution near the contact zone, due to the enormous increase in computational expense in transitioning from 2D to 3D stress analysis. Thus, a very coarse mesh analysis was performed in order to estimate the optimal grid resolution required for the continuum stress calculations presented in this Chapter.

The mesh analysis was performed using an infinitely long wire indenter with a diameter of 125 nm and with indentation strength corresponding to a maximum contact pressure of 18 GPa. The substrate dimensions were set to be 210.3 nm in the x -direction, 210.3 in y -direction, and 157.7 nm in the z -direction. The stress was computed for three meshes with 19490, 37957, and 99716 degrees of freedom by indenting a small amount, increasing the indentation amount slightly, re-solving the stress problem using the solution as an initial guess, and repeating until the desired contact pressure was achieved; the substrate grids are shown in Figure 5.4, along with the zz -component of the stress fields at the top of the substrate. Corresponding run times for the stress calculations were approximately 0.5, 1.3, and 4.5 hours, respectively. Each of the three stress fields were then interpolated onto the LKMC domain. Simulations of the compositional evolution, starting with uniform $\text{Si}_{0.8}\text{Ge}_{0.2}$, were performed for a 3 hour thermal anneal at 1000°C .

Shown in Figure 5.5(a) are the concentration profiles, averaged over the y -direction, in the top layer of LKMC cells, using the interpolated stress fields generated by each of the three meshes shown in Figure 5.4. While the coarsest grid shows some minor deviations in the Ge concentration at the edges of the indentation region, the other two grids lead to compositional profiles that are in excellent agreement.

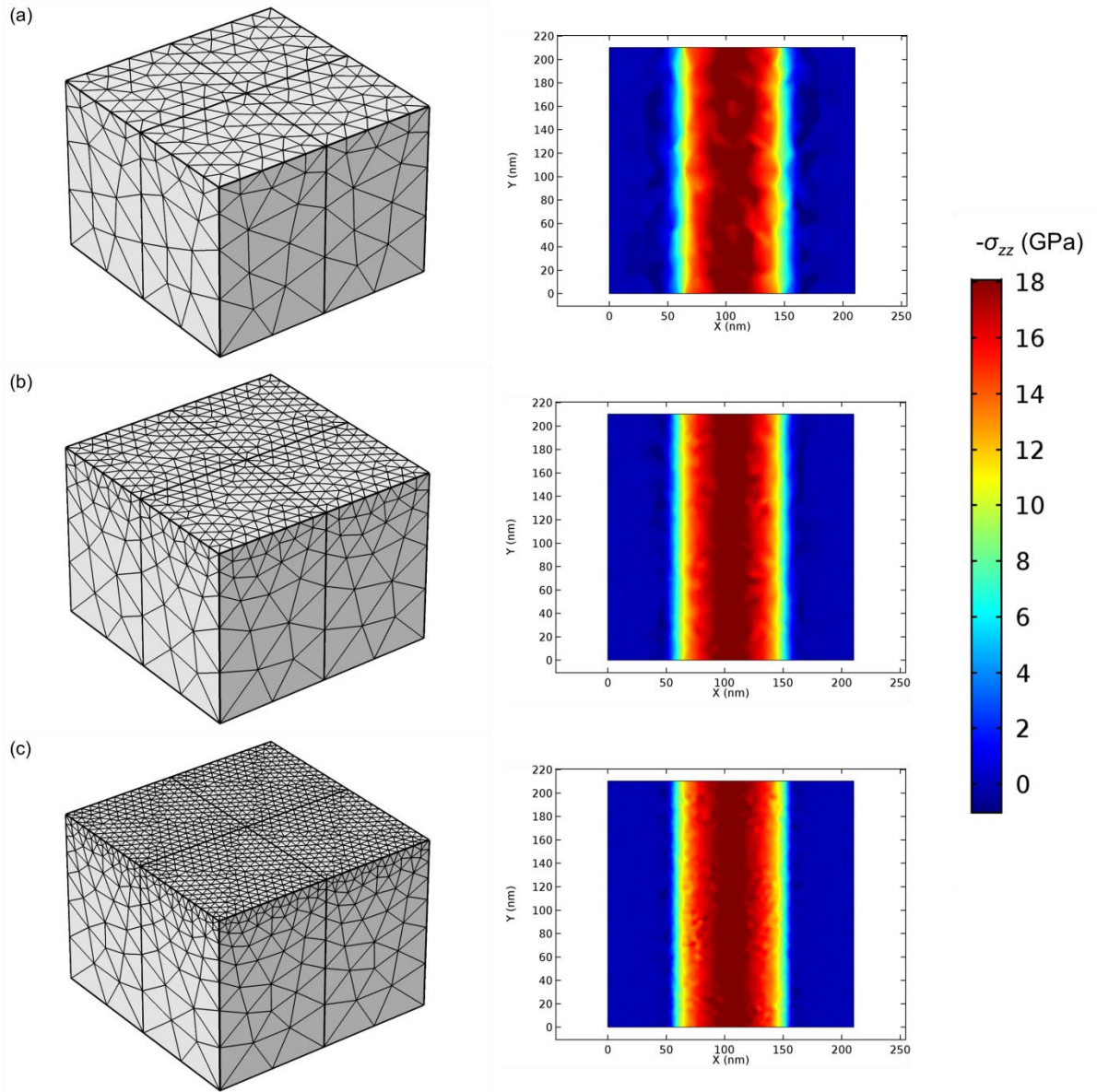


Figure 5.4. Meshes used in mesh refinement study (left), along with σ_{zz} in xy -plane at top substrate surface in z (right) for (a) coarsest mesh (b) intermediate mesh (c) finest mesh.

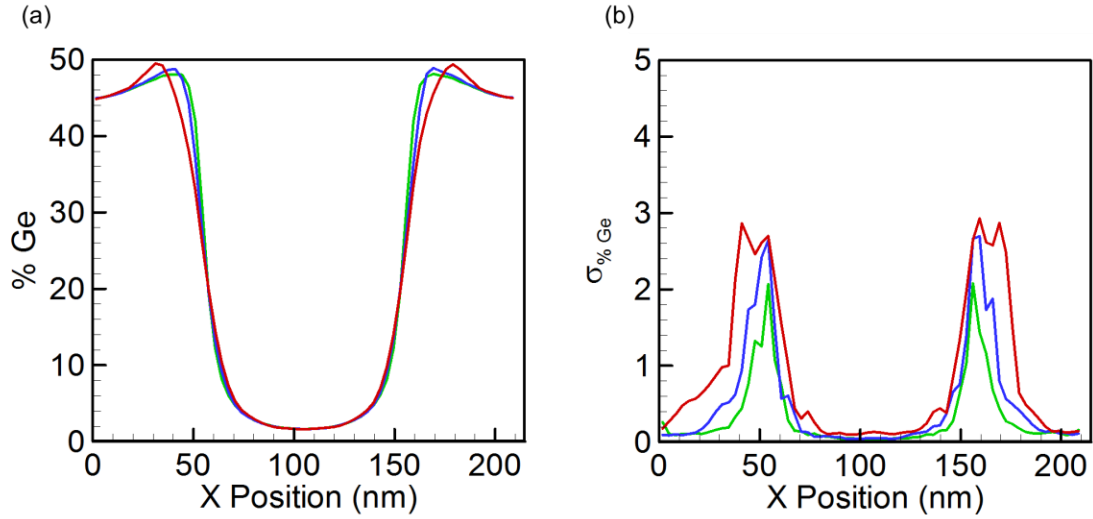


Figure 5.5. (a) Composition and (b) standard deviation in top layer of LKMC cells after 3 hours of annealing at 1000 °C after solving stress problem using mesh in Figure 5.4(a) (red), mesh in Figure 5.4(b) (blue), mesh in Figure 5.4(c) (green).

In Figure 5.5(b), the standard deviation of the concentration along the y -direction is shown for each case. Note that the wire indenter geometry should correspond to zero concentration gradients in the y -direction, and since we are using the “net event” framework, there should be essentially zero noise in the LKMC solution at the resolutions considered (see Section 5.2.1). The enhanced standard deviation near the edge of the indenters indicates some error, but in each case the distortion is quite small ($<3\%$). We also computed the L^2 -norm [99] of the concentration in the top layer of LKMC cells versus the finest solution, which yields $4 \times 10^{-4} \text{ cell}^{-1}$ for the coarsest mesh, and $2 \times 10^{-4} \text{ cell}^{-1}$ for the intermediate mesh; the error with the intermediate mesh is well below 1%. Based on these observations the intermediate mesh resolution was used to generate grids for all studies described in this Chapter.

5.4 Results and Discussion

There is a very high-dimensional parameter space associated with the patterning process described in this Chapter, along with Chapters 2 and 4. A table listing the parameters examined in this Chapter is provided in Table 5.1. The optimization of near-surface structures in SiGe given this parametric space presents a classic “inverse” problem, as the desired result is known ahead of time, but it is not obvious which set of parameters (if any) will achieve the goal. Thus, we have performed a set of simulations on a small subset of this vast parametric space. Note that there are additional relevant parameters that we did not consider, including indentation strength, annealing temperature, and anneal time, although some of these were previously considered in Chapter 4. In the interest of minimizing computational expense, for all of the studies presented in this Section, we consider substrates annealed under maximum indentation contact pressures of 18 GPa for three hours at 1000 °C. Unless otherwise stated, the figures shown in this work are of the top layer of cells in z (i.e., the top xy -plane of cells).

Table 5.1. Parametric space considered in this Chapter, with relevant subsection considered.

Parameter	Subsection
Indenter Size	5.4.1
Indenter Spacing (Pitch)	5.4.2
Indenter Array Patterns	5.4.3
Indenter Shape	5.4.4
Film Ge Concentration	5.4.5

The geometry of the indenters considered is depicted schematically in Figure 5.6. All indenters in this Section had a spherical indenter cap, defined by the radius of curvature of the cap (R_{cap}), and the indenter width (R). As shown in Figure 5.6(a), the radius of curvature can exceed the indenter radius by any amount, allowing the study of the impact of “flatness” of the cap. In addition, the inter-indenter spacing is defined as the pitch, p , as depicted in Figure 5.6(b).

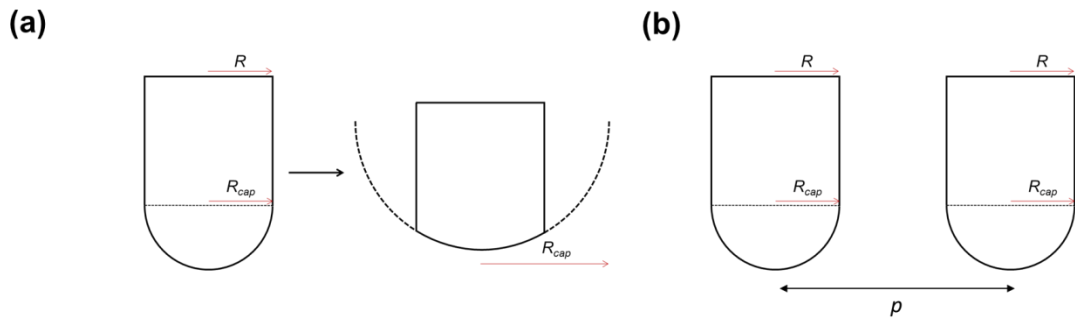


Figure 5.6. (a) Sample indenter geometries, ranging from a spherical cap (radius of curvature of cap (R_{cap}) = indenter radius (R)) to an indenter with $R_{cap} \gg R$ (b) Two indenters separated by pitch, p .

In LKMC studies on a cubic-oriented indenter array, all LKMC domains had dimensions in x and y equal to the indenter pitch. A few periodic images are included to highlight effects at the edge of the LKMC simulation box. For hexagonal oriented arrays, since our LKMC simulator operates on a cubic lattice, we ran a large indenter simulation box in LKMC that contained many images of the stress field generated. We then only consider the central section (in x and y) of the large LKMC box to remove edge effects resulting from the fact that the cubic LKMC domain is not aligned with the edge of the outermost stress field image due to the incompatibility of hexagonal and cubic lattices.

5.4.1 Indenter Size

To start, we examined the impact of indenter size for indenter tips with $R_{cap} = R$, when annealing a $\text{Si}_{0.8}\text{Ge}_{0.2}$ substrate at a cubic p of 210.3 nm. Figure 5.7 illustrates compositional profiles over a wide range of indenter radii. Bigger indenters caused wider depletion zones, and, in addition, as the indenter size increased there was a slight “piling up” of Ge in the area surrounding the impact zones [100]. This pileup is a result of increasing the relative volumes of the domain that are under compression, which leads to a smaller volume of uncompressed regions for Ge to preferentially diffuse towards. This effect is something we tried to exploit in subsequent studies presented later in this Section.

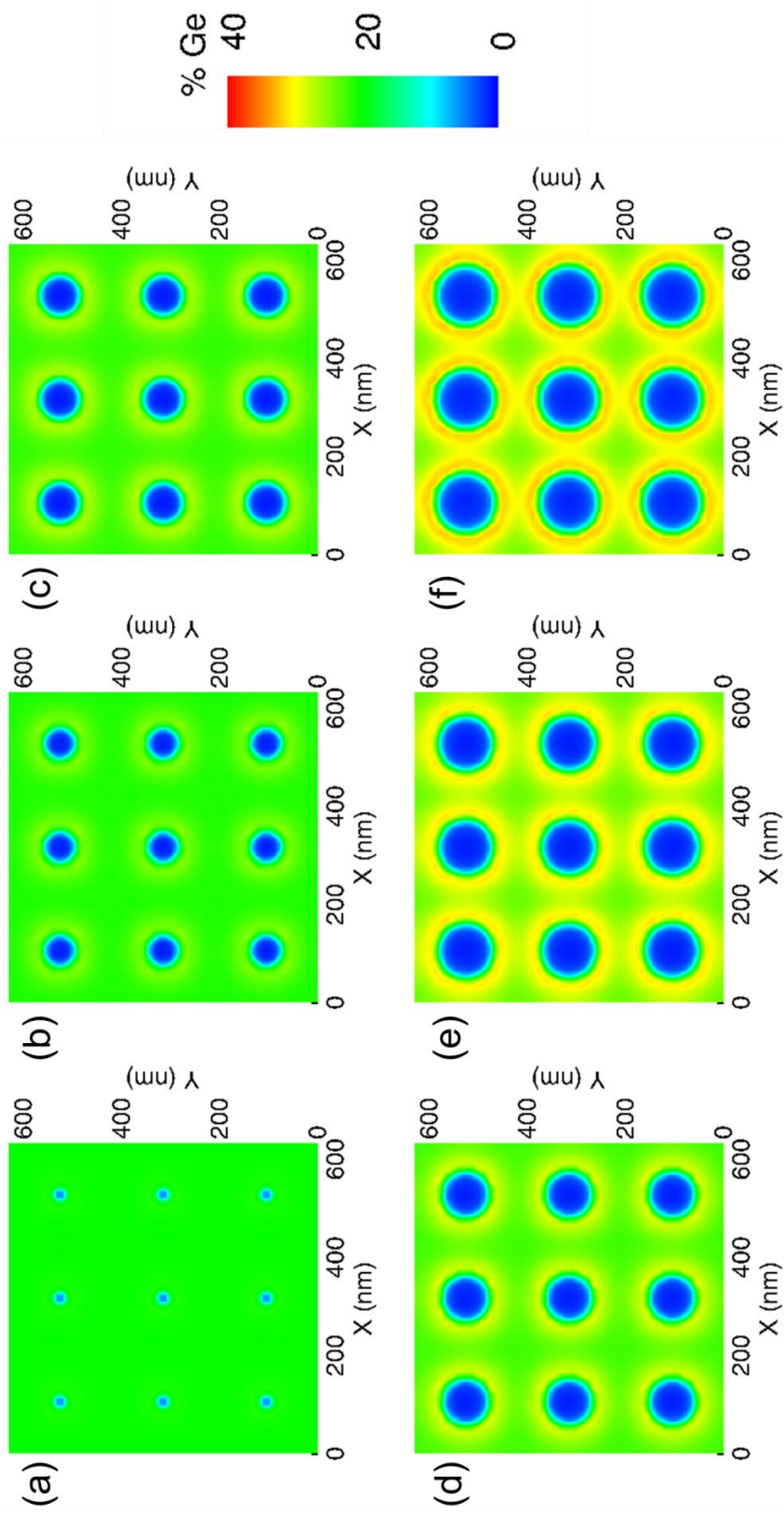


Figure 5.7. Compositional profiles after thermal annealing of a $\text{Si}_{0.8}\text{Ge}_{0.2}$ substrate under the action using a spherical indenter tip measuring (in R_{cap} and R) (a) 25 nm (b) 100 nm (c) 125 nm (d) 150 nm (e) 175 nm (f) 200 nm, at a cubic p of 210.3 nm.

5.4.2 Indenter Spacing (Pitch)

Since the pitch relative to indenter size impacts the amount of Ge pileup in the areas surrounding the depletion zone, we next studied the effects of pitch at a given spherical indenter size ($R_{cap} = R = 125$ nm), annealing a $\text{Si}_{0.8}\text{Ge}_{0.2}$ substrate. Figure 5.8 shows the compositional and stress fields for two pitches. Similar to the effects of increasing indenter size at a given pitch, narrowing the pitch at a given indenter size clearly gets closer to our goal of applying compressive stress everywhere, except for isolated regions, leading to much higher Ge build-up in the regions between indenters that are unstressed.

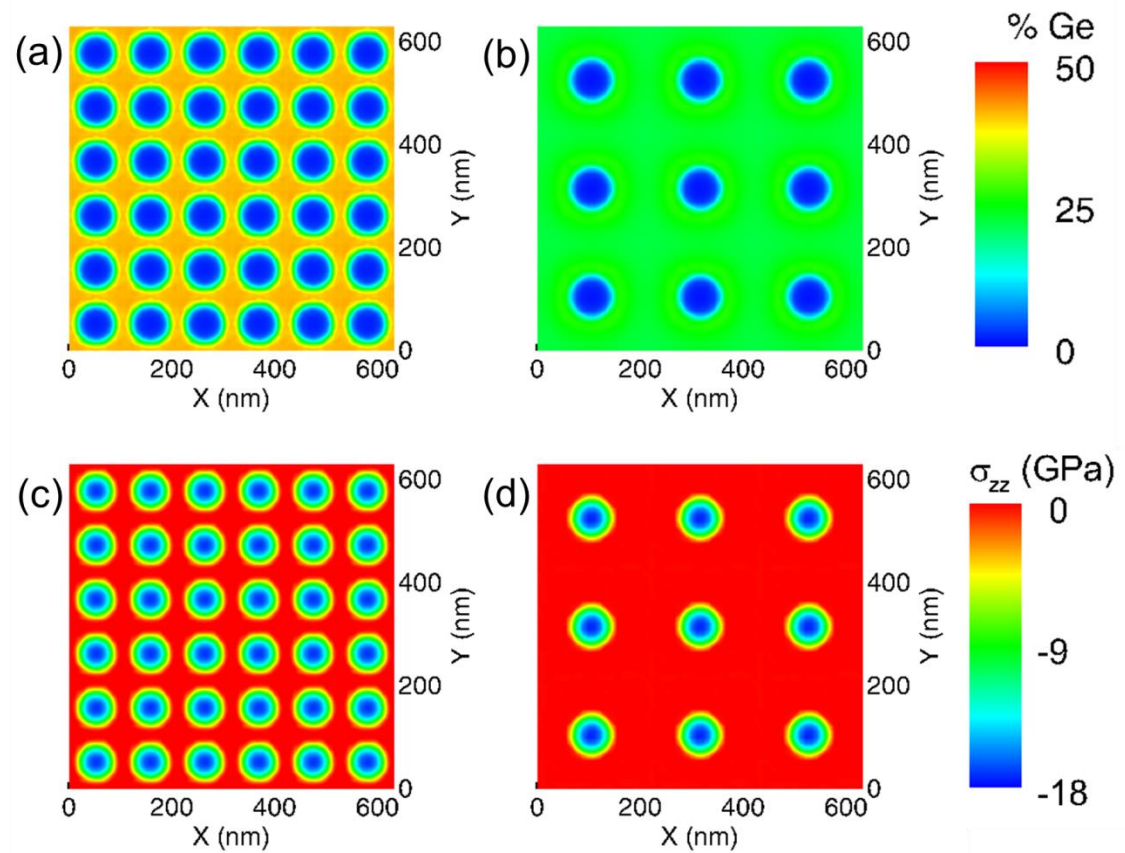


Figure 5.8. Compositional (a-b) and stress (c-d) profiles after thermal annealing of a $\text{Si}_{0.8}\text{Ge}_{0.2}$ substrate at $1000\text{ }^\circ\text{C}$ using a spherical indenter tip with $R_{cap} = R = 125\text{ nm}$ at a cubic p of (a,c) 105.2 nm (b,d) 210.3 nm .

5.4.3 Indenter Array Patterns

While the pitch and size of the indenter clearly are key factors that govern the extent of Ge enhancement in the near surface region of the film, we next studied the array geometry to see effects, if any, on the resulting compositional distribution upon thermal annealing. We altered the geometry of the indenter array from cubic to hexagonal, indenting a $\text{Si}_{0.8}\text{Ge}_{0.2}$ substrate with indenter geometry of $R_{cap} = R = 125\text{ nm}$ at a p of 210.3 nm . The resulting stress field and substrate composition after annealing are

illustrated in Figure 5.9. The effect of the array geometry was not very pronounced, with minimal compositional differences at the pitch considered, although it is possible the effect could be more important at different indenter spacing.

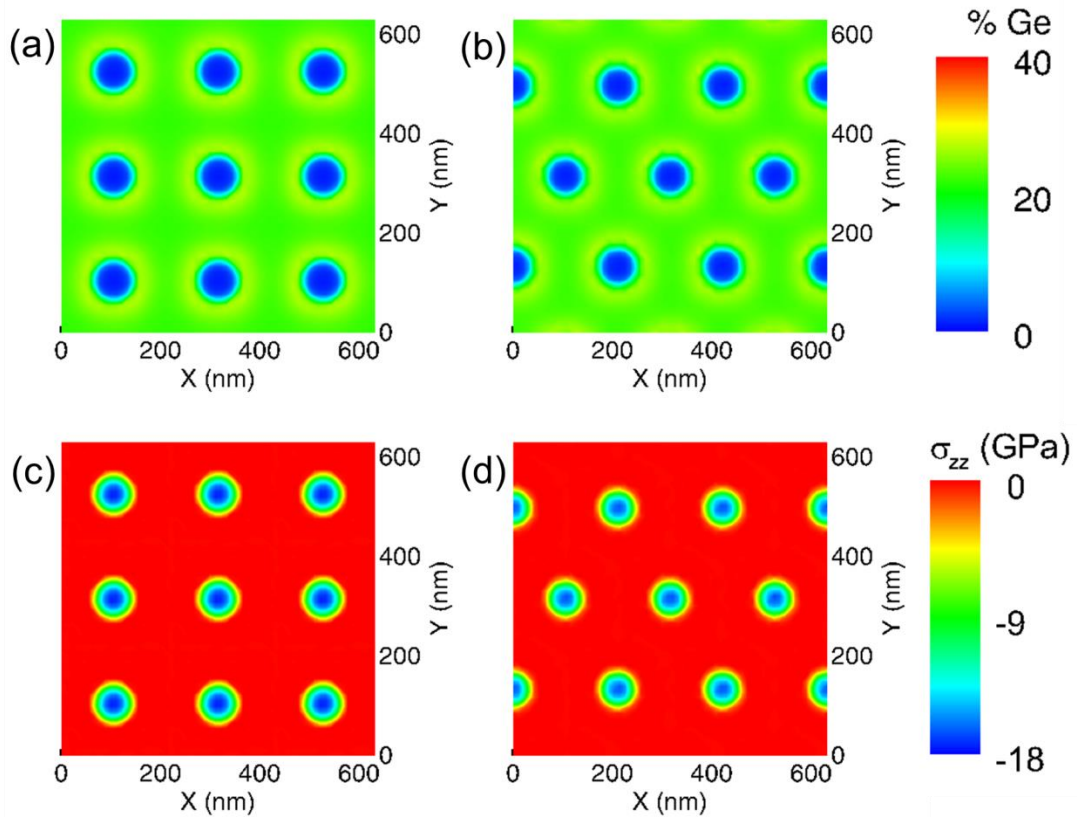


Figure 5.9. Compositional (a-b) and stress (c-d) profiles after thermal annealing of a $\text{Si}_{0.8}\text{Ge}_{0.2}$ substrate at $1000\text{ }^\circ\text{C}$ using a spherical indenter tip with $R_{cap} = R = 125\text{ nm}$ at a p of 210.3 nm with an (a,c) cubic indenter array (b,d) hexagonal indenter array.

5.4.4 Indenter Shape

We next ran a sequence of simulations of annealing an initially uniform $\text{Si}_{0.8}\text{Ge}_{0.2}$ substrate at a cubic p of 210.3 nm using an indenter with varying R_{cap} at a fixed width ($R = 125\text{ nm}$). Shown in Figure 5.10 are the stress fields generated in this set of simulations. What is immediately apparent is that there is a sharp interface between a small,

uncompressed region, and the majority of the domain, which is under compression, that becomes more pronounced as R_{cap} increases. This effect is virtually the reverse of using a fully spherical cap, which, at moderate pressures, imposes a highly focused stress field on a small area of contact on the surface, while leaving much of the near-surface region under no stress.

Figure 5.11 shows the compositional profiles in all cases. By using such flat tipped indenters, we can clearly generate at least two-dimensionally confined quantum wires. However, Figure 5.12 shows the z dependence of stress and composition for the $r = 1000$ nm and $r = 2000$ nm case, and it is obvious that three dimensionally confined, perfectly ordered, Ge quantum dots (QDs) have been generated, with lateral dimensions < 50 nm and vertical dimensions < 20 nm.

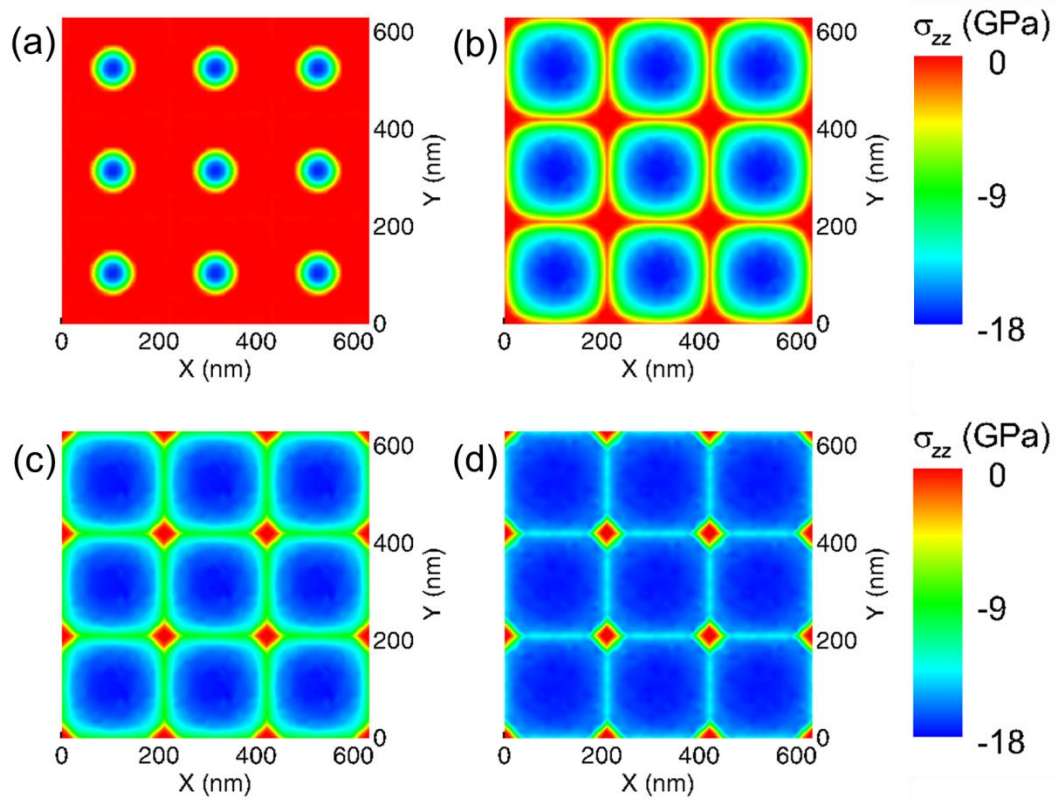


Figure 5.10. Stress field during thermal annealing of a $\text{Si}_{0.8}\text{Ge}_{0.2}$ substrate under the action of an indenter with $R = 125$ nm at a cubic p of 210.3 nm for 3 hours at 1000 °C for (a) $R_{cap} = 125$ nm (b) $R_{cap} = 500$ nm (c) $R_{cap} = 1000$ nm (d) $R_{cap} = 2000$ nm.

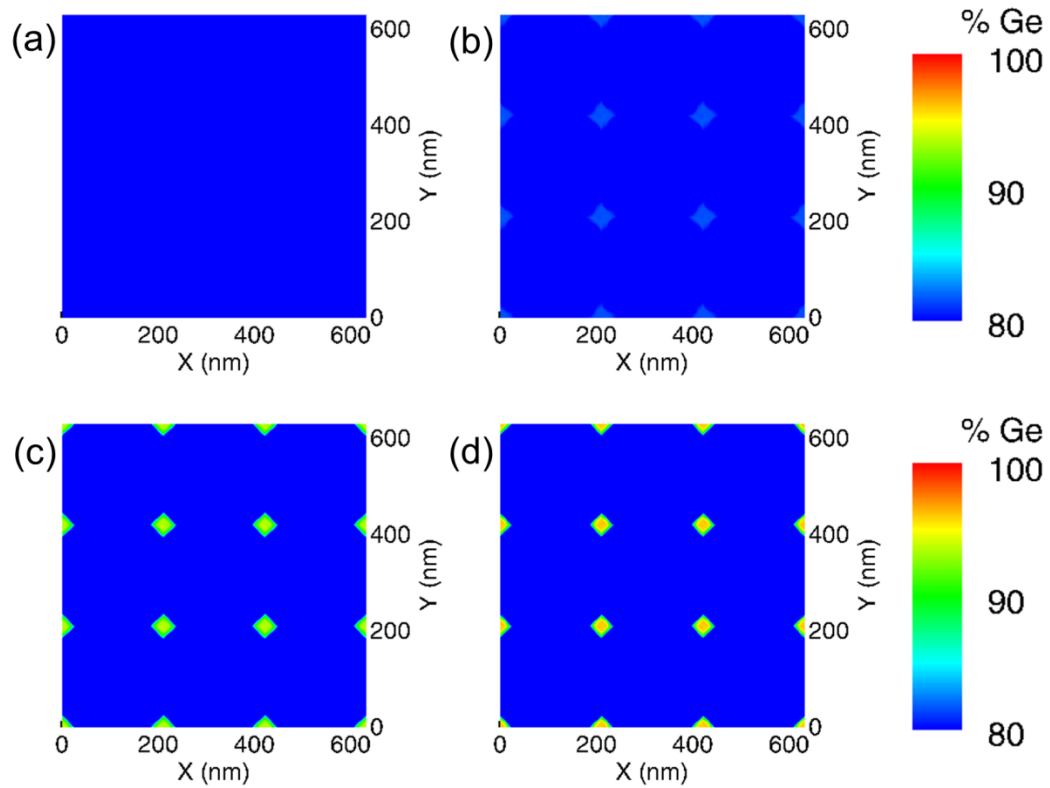


Figure 5.11. Compositional profile after thermal annealing of a $\text{Si}_{0.8}\text{Ge}_{0.2}$ substrate under the action an indenter with $R = 125$ nm at a cubic p of 210.3 nm for 3 hours at 1000 °C for (a) $R_{cap} = 125$ nm (b) $R_{cap} = 500$ nm (c) $R_{cap} = 1000$ nm (d) $R_{cap} = 2000$ nm.

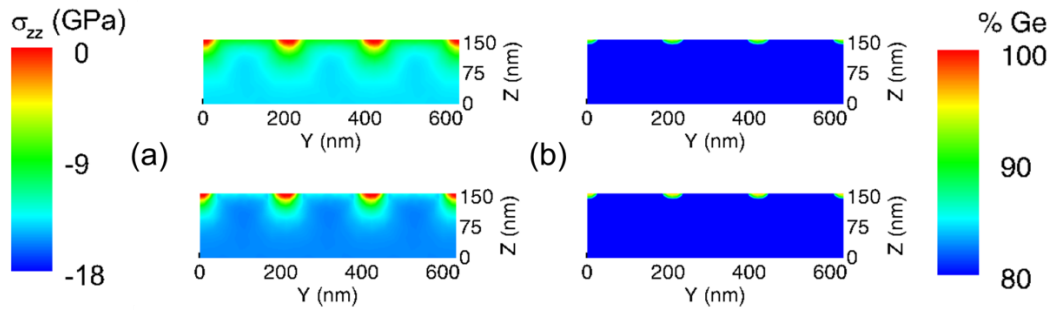


Figure 5.12. Stress field (a) and compositional profile (b) in yz -plane at $x = 210.3$ nm for (top) $R_{cap} = 1000$ nm (bottom) $R_{cap} = 2000$ nm after thermal annealing of a $\text{Si}_{0.8}\text{Ge}_{0.2}$ substrate under the action of an indenter with $R = 125$ nm at a cubic p of 210.3 nm.

5.4.5 Film Ge Concentration

Finally, using an indenter tip with $R_{cap} = R = 125$ nm at a cubic p of 210.3 nm, we looked at the impact of substrate composition on the profiles. Figure 5.13 shows the resulting stress field and composition after annealing the substrates. One would expect the amount of Ge segregation near the surface to increase with increasing background Ge in the initially uniform film, and this is indeed the case. A more surprising result, however, is that the amount of Ge depletion in the contact zone appears to be relatively fixed at nearly 100% over a wide range from 0-50% Ge initial substrate composition. This result could have important implications for compositional contrast in the resulting near-surface structures in these cases. However, given the dramatic increase in cost of $\text{Si}_{1-x}\text{Ge}_x$ with Ge composition, we would prefer to use substrates with lower amounts of Ge, which is one primary reason we chose $\text{Si}_{0.8}\text{Ge}_{0.2}$ for most of the studies presented in this Chapter.

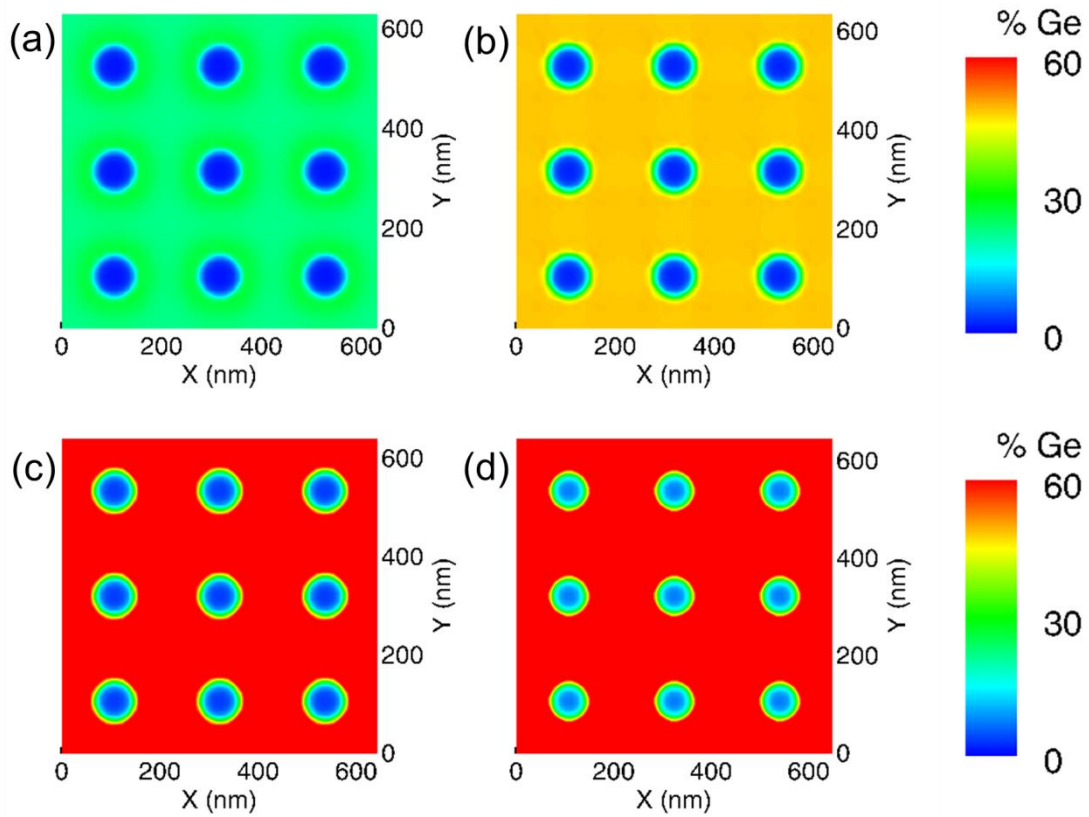


Figure 5.13. Compositional profiles after thermal annealing of a $\text{Si}_{1-x}\text{Ge}_x$ substrate under the action of a spherical indenter tip with $R_{cap} = R = 125$ nm at a cubic p of 210.3 nm, with the substrate compositions of (a) 20% Ge (b) 40% Ge (c) 60% Ge (d) 80% Ge.

5.5 Variable Stress Anneals

Temporal variation in stress and temperature during a thermal anneal comprises another section of the parametric space that governs the patterning process. While full consideration of this area is left to future work, we ran an example variable stress anneal to demonstrate the viability of this concept: We subjected a $\text{Si}_{0.8}\text{Ge}_{0.2}$ film to a cylindrical indenter with its axis the y -direction during an anneal for 3 hours at 1000 °C. We then rotated the stress field to make its axis in the x -direction (as in all of the other results in

this Chapter, we did not re-compute a stress field, as our previous analysis showed that the impact of the indenter is far greater than the contribution from internal mismatch stresses or the change in moduli [100] (see Chapter 4)), and then continued the anneal. Figure 5.14 and Figure 5.15 show the results of this study. There is a period (at approximately one minute) that there was greater than 60% Ge in the near surface region of the film, but it was very short. The precision in timing required will make annealing experimentally very difficult. In addition, although not shown on the color scale which was chosen to enhance patterning features in every image, the maximum composition in the near surface region of the film is roughly 75% Ge in the brief moment of extreme compositional enhancement after the rotation of the indenter array, a result which shows promise for the viability of the variable stress approach. A detailed parametric scan will be difficult to conduct, however, as the annealing schedule can vary over a wide range of times before and after the stress field is changed.

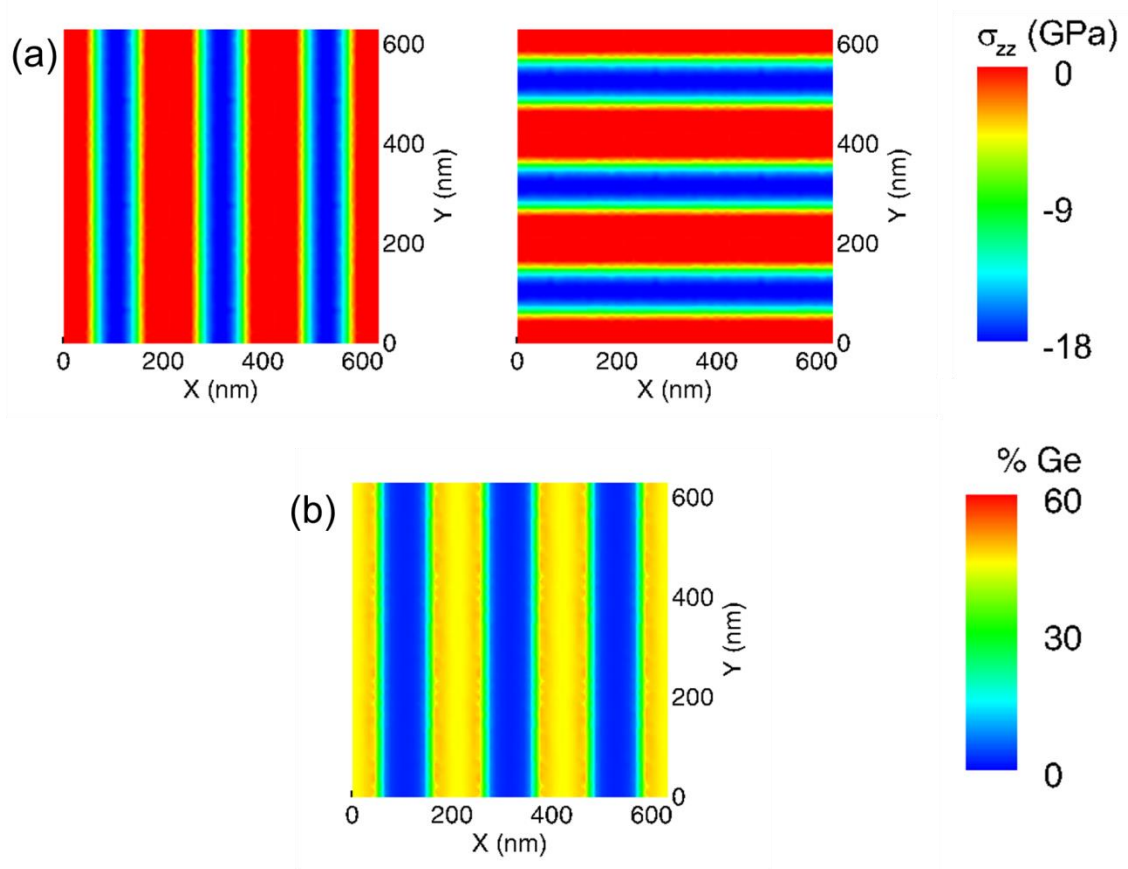


Figure 5.14. (a) Stress before (left) and after (right) rotation of cylindrical indenter after 3 hours of thermal annealing of a $\text{Si}_{0.8}\text{Ge}_{0.2}$ substrate annealed at $1000\text{ }^\circ\text{C}$ (b) compositional profile at time of rotation.

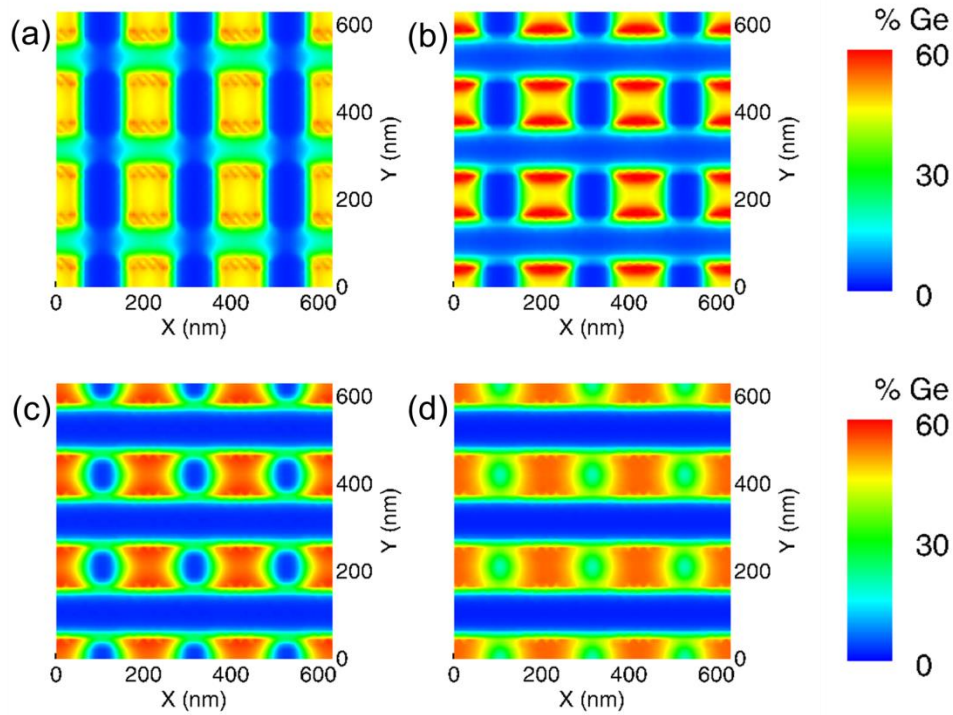


Figure 5.15. Compositional profiles after rotating indenter field and continuing the thermal anneal at 1000 °C for (a) 1 minute (b) 10 minutes (c) 1 hour (d) 3 hours.

5.6 Conclusions

In this chapter, we performed a targeted parametric scan of the high-dimensional space of indenter pitches, geometries, and film compositions for patterning QCSs in $\text{Si}_{1-x}\text{Ge}_x$ thin films via nanoindentation. By choosing the appropriate indenter pitch and geometry, even in a film as low as 20% Ge, we were able to generate periodic, three-dimensional, Ge-rich regions in the near-surface region of an initially uniform film. These Ge-rich regions meet the requirements set out in the literature for potential use as addressable QDs in future technologies.

We recognize that we just considered a small subspace of the vast parametric space describing the compositional redistribution process. A full systematic optimization of all of the parameters involved in the patterning process could potentially discover alternative combinations of parameters that are capable of producing Ge QDs, perhaps using even lower composition Ge films than the standard 20% Ge considered here.

In addition, we demonstrated the feasibility of temporally varying the stress field during a thermal anneal, as we were able to generate significantly different patterns after changing the stress field orientation. This fact, along with the possibility of altering the temperature during an anneal, provides an additional large segment of the parametric space to explore. We leave a full parametric analysis of the entire parameter space to future work.

Chapter 6. Analysis of Point Defect Diffusion In Stressed Si and Ge

6.1 Introduction

As clearly evident in the previous Chapters, atomic diffusion is at the heart of the stress transfer process, as well as much of the processing that takes place in the fabrication of microelectronic and optoelectronic devices. For example, short-range atomic diffusion is critical in the electrical activation of implanted dopants (e.g., B or P), but must be controlled carefully to ensure that it does not lead to undesirable long-range spreading of the dopant profile [101, 102].

In crystalline semiconductors, such as Si, Ge, and the various III-V materials (e.g., GaAs and InAs), this diffusion is mediated principally by point defects, namely interstitials and vacancies, that exist in one or more electrical charge states. The role of point defects in the evolution of microstructure in crystalline semiconductors is multifaceted. In addition to being the mediators of atomic mobility as described in the previous Chapters, they are also directly responsible for the formation of various types of crystallographic defects that can play important roles in device performance. In the well-established case of Si bulk crystal growth, for example, the aggregation of large numbers of vacancies leads to the formation of nanoscopic voids [103], while an excess of self-interstitials generates a multitude of defect structures ranging from small, three-dimensional clusters [104] to large, tangled networks of dislocations [105]. However, such aggregation processes require significant supersaturations of point defects and are generally not relevant for the situations considered in this thesis and here we focus on their role as atomic diffusion mediators.

The capacity for point defects to move atoms across the bulk of a material depends on their intrinsic diffusivity as well as their concentrations. In Chapters 4 and 5, it was assumed that point defects always exist in their (spatially and temporally varying) locally equilibrium concentrations. It is well established that both the diffusivity and equilibrium concentration, and hence the total transport capacity (see Chapter 4), of each point defect species depends approximately exponentially on temperature. This is particularly true for Si, where numerous experimental [106-108] and theoretical [109, 110] studies have focused on estimating the temperature dependence of self-interstitial and vacancy diffusivities and equilibrium concentrations.

On the other hand, the impact of lattice stress on point defect transport and thermodynamics is much less well established. The importance of stress in the types of processes relevant to this thesis is of course obvious—stress is intentionally applied to diffusively drive a system towards some desired configuration. But the role of stress in modulating point defect properties is also increasingly appreciated in other settings. For example, stress arising from temperature gradients is always present during crystal growth of Si from the melt, e.g., by the Czochralski or floating-zone methods [111]. Ion-implantation of dopants into semiconductor wafers also potentially produces large amounts lattice stress that evolves as the wafer is annealed [112]. In the case of Si crystal growth, thermal stresses are now known to influence the subtle balance between self-interstitial and vacancy populations and can alter the dominant point defect species, and therefore the type of defect aggregate, remaining in the crystal after it is grown and cooled. Some recent theoretical studies based on electronic structure calculations have therefore focused on computing the dependence of point defect formation energies (and

therefore equilibrium concentrations) on various types of stress states [78, 113]. Much less attention has been given to the impact of stress on point defect diffusivities and even less is known about the impact of stress on point defect properties in pure Ge and SiGe alloys.

In Chapters 4 and 5, we adopted the parameter values suggested in ref. [38] to describe the impact of stress on point defect properties in the SiGe alloy system. In some sense, these parameter values may be considered as being ‘internally consistent’ with the other model parameters in ref. [38] in that the interdiffusion model results were validated against experimental data. However, there remains much ambiguity regarding the robustness of the assumed values, their relationship to other literature estimates, and sensitivity of the model to them. In this Chapter, we employ a series of well-known empirical potentials for Si and Ge to study the impact of stress on point defect transport and equilibrium properties. The calculations are based on a theoretical formalism put forward by Aziz [32, 73], which is described in detail in Section 6.2. The predictions obtained with the various empirical potentials first are compared to each other and then to existing literature values in Section 6.4. Finally, conclusions and outlook are presented in Section 6.5.

6.2 Theoretical Formalism for Stress Impact on Point Defect Thermophysical Properties

In this section, we describe the formalism that underpins the calculations presented in this Chapter. As noted in the Introduction, the theory presented here follows

closely the exposition of Aziz in ref. [73]. The formation of a point defect is generally associated with the concomitant creation of lattice strain. Consider the process depicted in Figure 6.1(a), in which a bulk lattice atom is moved to the surface, leaving behind a vacancy. There are two volumetric changes associated with this process: (1) the new surface atom increases the volume of the material by an atomic volume (denoted by the red-shaded Ω) and (2) the lattice relaxes around the vacancy (blue). Similar arguments may be made for the case of self-interstitial formation, which is shown in Figure 6.1(b). Here, a surface atom is moved into an interstitial position within the bulk, reducing the material volume by one atomic volume at the surface while also creating lattice strain around the new defect. Point defect migration also is generally associated with lattice strain. As shown in Figure 6.1(c) and (d) for vacancies and self-interstitials, respectively, lattice strain during the defect hop may be different in the directions parallel and perpendicular to the hop (purple and orange, respectively). In the following sections detailed derivations are presented for the relationship between stress and point defect formation/migration.

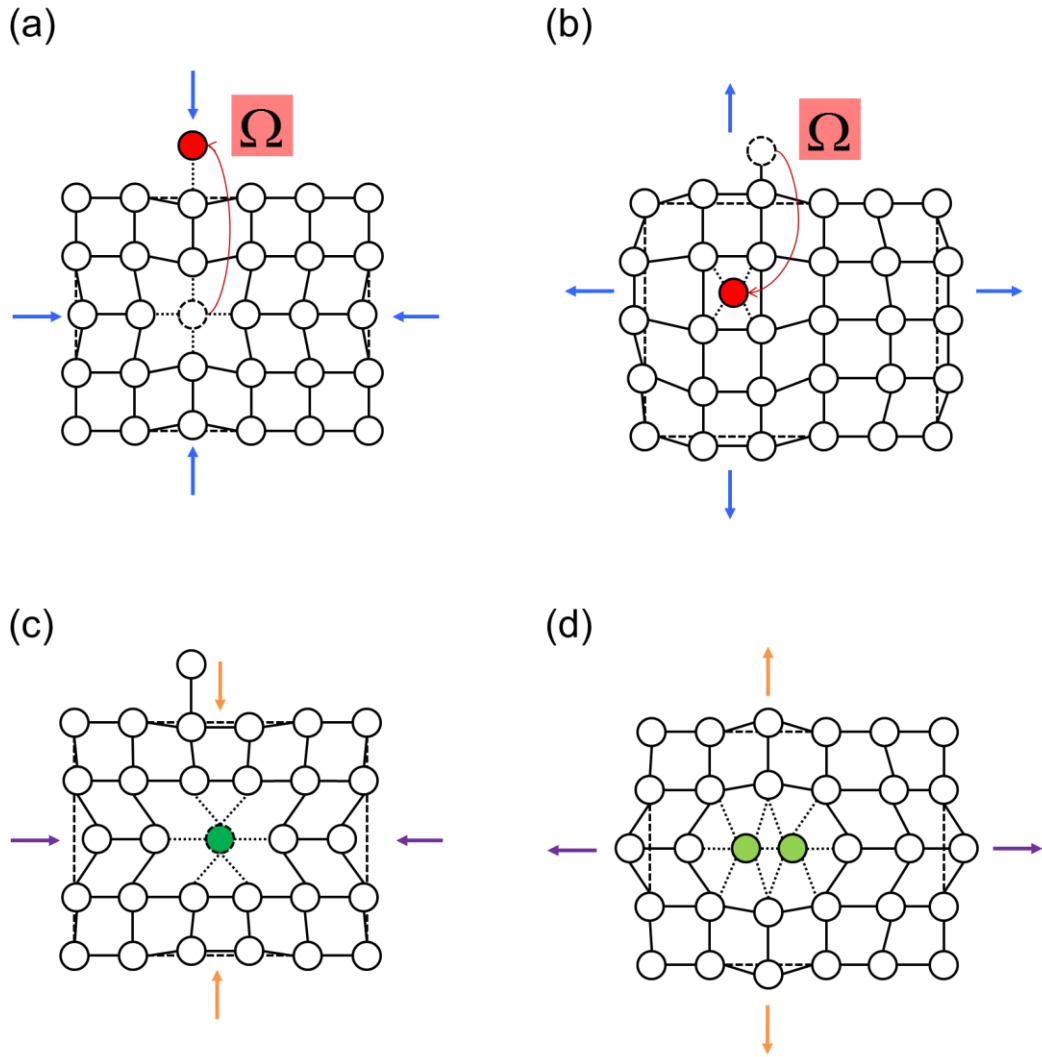


Figure 6.1. (a) Film dimension changes upon formation of vacancy (b) Film dimension changes upon formation of interstitial (c) Film dimension changes upon migration of vacancy (d) Film dimension changes upon migration of interstitial. See text for details

6.2.1 Point Defect Formation in a Stress Field

The Gibbs free energy of formation of a point defect species, G^f , is generally given by

$$G^f = U^f - TS^f - \sigma_{ij} V_{ij}^f, \quad (6.1)$$

where U^f and S^f are the formation internal energy and entropy, and $\sigma_{ij}V_{ij}^f$ is the stress-strain work associated with point defect creation. Here, and in the remainder of the Chapter, the stress-strain work term is written in the conventional implied summation form over all three Cartesian indices. In other words, the 9 V_{ij}^f and 9 σ_{ij} terms each collectively represent the elements of 2nd-order tensors. Taking derivatives of eq. (6.1) with respect to σ_{ij} gives

$$\frac{\partial G^f}{\partial \sigma_{ij}} = \frac{\partial U^f}{\partial \sigma_{ij}} - T \frac{\partial S^f}{\partial \sigma_{ij}} - V_{ij}^f - \sigma_{ij} \frac{\partial V_{ij}^f}{\partial \sigma_{ij}}. \quad (6.2)$$

The equilibrium concentration of a point defect species ($A=I,V$) is generally given by [114]

$$C_A = C_{A0} \exp\left(-\frac{G^f}{kT}\right). \quad (6.3)$$

where C_{A0} is the lattice site density and G^f includes vibrational and configurational entropic contributions [114-121]. Taking the derivative of eq. (6.3) with respect to σ_{ij}

$$-kT \frac{\partial \ln C_A}{\partial \sigma_{ij}} = \frac{\partial G^f}{\partial \sigma_{ij}}. \quad (6.4)$$

Combining eqs. (6.4) and (6.2), and using the differential of U^f , generalized for non-hydrostatic stresses,

$$dU^f = TdS^f + \sigma_{ij}dV_{ij}^f, \quad (6.5)$$

gives

$$kT \frac{\partial \ln C_A}{\partial \sigma_{ij}} = V_{ij}^f. \quad (6.6)$$

The formation volume tensor represented by the elements V_{ij}^f for the cases of relevance here is given by

$$\mathbf{V}^f = \begin{pmatrix} 0 & & \\ & 0 & \\ & & \pm\Omega \end{pmatrix} + \frac{V^r}{3} \begin{pmatrix} 1 & & \\ & 1 & \\ & & 1 \end{pmatrix}. \quad (6.7)$$

The first tensorial term accounts for the increase/decrease of one atomic volume at the (001) surface (the wafer surface orientation assumed throughout this thesis) due to the formation of a vacancy/self-interstitial. The second term accounts for the isotropic relaxation strain. Note that while any single defect configuration can result in off-diagonal [73] and/or different normal contributions [75, 80] to the formation volume tensor, averaging over many orientations and configurations of defects results in a diagonal formation volume tensor, with isotropic relaxation [73].

Integrating eq. (6.6), the stress dependence of point defect concentration is computed as

$$\begin{aligned} \frac{C(\boldsymbol{\sigma})}{C(\mathbf{0})} &= \exp\left(\beta \left[\int_0^{\sigma_{ij}} V_{ij}^f d\sigma_{ij} \right]\right) \\ &= \exp\left(\beta \left[\int_0^{\sigma_{33}} \pm\Omega d\sigma_{33} + \int_0^{\sigma_{11}} \frac{V^r}{3} d\sigma_{11} + \int_0^{\sigma_{22}} \frac{V^r}{3} d\sigma_{22} + \int_0^{\sigma_{33}} \frac{V^r}{3} d\sigma_{33} \right]\right), \end{aligned} \quad (6.8)$$

where $\beta \equiv (k_B T)^{-1}$, given a generalized stress tensor $\boldsymbol{\sigma} = \begin{pmatrix} \sigma_{11} & & \\ & \sigma_{22} & \\ & & \sigma_{33} \end{pmatrix}$.

6.2.2 Point Defect Diffusion in a Stress Field

Focusing now on point defect migration, consider a small region (the ‘subsystem’) surrounding a diffusing defect that is large enough to fully contain any lattice impact due to the migration of the defect, in a much larger ‘reservoir.’ According to transition state theory, the jump rate of a defect, Γ_A , depends on the minimum work, W_{min} , performed on the subsystem and reservoir by an external force, to change the subsystem from its minimum state to the saddle point configuration, i.e.,

$$\Gamma_A = \nu \exp\left(-\frac{W_{min}}{kT}\right), \quad (6.9)$$

where ν is the attempt frequency, which is assumed to be constant [73]. The minimum work may be expressed as the integral from the initial configuration, X , to the saddle-point one, X^* , of the stress-strain work, so that

$$W_{min} = V_0^{sub} \int_X^{X^*} \mathbf{T}_{ij}^{sub} d\zeta_{ij}^{sub}, \quad (6.10)$$

where V_0^{sub} is the initial volume of the subsystem, \mathbf{T}^{sub} is the Piola-Kirchhoff stress on the boundaries of the subsystem (the force divided by the original area of the subsystem), and $\zeta_{ij}^{sub} \equiv \partial u_j / \partial x_i$ is the deformation gradient in the subsystem, with \mathbf{u} being the displacement field.

As before, taking the derivative of eq. (6.9) with respect to σ_{ij} yields

$$-kT \frac{\partial \ln \Gamma_A}{\partial \sigma_{ij}} = \frac{\partial W_{min}}{\partial \sigma_{ij}}. \quad (6.11)$$

The differential of the Helmholtz free energy, F , generalized for non-hydrostatic stresses, is written as

$$dF = V_0^{mac} \sigma_{ij} d\varepsilon_{ij} + V_0^{sub} T_{ij}^{sub} d\zeta_{ij}^{sub} - SdT \quad (6.12)$$

where V_0^{mac} is the initial volume of the reservoir, and $\boldsymbol{\sigma}$ is an stress field in the reservoir, accompanied by a strain $\boldsymbol{\varepsilon}$. The differential of the dual potential of F on strain [122], $\Psi \equiv F - V_0^{mac} \sigma_{ij} \varepsilon_{ij}$, is written as

$$d\Psi = -V_0^{mac} \varepsilon_{ij} d\sigma_{ij} + V_0^{sub} T_{ij}^{sub} d\zeta_{ij}^{sub} - SdT. \quad (6.13)$$

A Maxwell relation can be derived from eq. (6.13),

$$V_0^{sub} \frac{\partial T_{ij}^{sub}}{\partial T} = -V_0^{mac} \frac{\partial \varepsilon_{ij}}{\partial \zeta_{ij}^{sub}}. \quad (6.14)$$

Plugging eqs. (6.14) and (6.10) into eq. (6.11), we obtain

$$kT \frac{\partial \ln \Gamma_A}{\partial \sigma_{ij}} = V_{ij}^m \quad (6.15)$$

where

$$V_{ij}^m \equiv V_0^{mac} \int_X^{X^*} d\varepsilon_{ij}. \quad (6.16)$$

Assuming that the defect jump distance does not change with stress, we can rewrite eqn. (6.15) as

$$kT \frac{\partial \ln D_A}{\partial \sigma_{ij}} = V_{ij}^m. \quad (6.17)$$

The migration volume tensor for hops in the (001) direction, for instance, is written as

$$\mathbf{V}_{001}^m = \begin{pmatrix} V_{\perp}^m & & \\ & V_{\perp}^m & \\ & & V_{\parallel}^m \end{pmatrix}. \quad (6.18)$$

Similar expressions can be written for hops in the (100) and (010) directions. Due to cubic symmetry, the off-diagonal components must be zero when averaging over all possible configurations [123].

Integrating eq. (6.17) gives the stress dependence of defect diffusivity,

$$\begin{aligned} \frac{D_{001}(\boldsymbol{\sigma})}{D_{001}(\mathbf{0})} &= \exp\left(\beta \left[\int_0^{\sigma_{ij}} V_{001,ij}^m d\sigma_{ij} \right]\right) \\ &= \exp\left(\beta \left[\int_0^{\sigma_{11}} V_{\perp}^m d\sigma_{11} + \int_0^{\sigma_{22}} V_{\perp}^m d\sigma_{22} + \int_0^{\sigma_{33}} V_{\parallel}^m d\sigma_{33} \right]\right), \end{aligned} \quad (6.19)$$

where $\beta \equiv (k_B T)^{-1}$, given a generalized stress tensor $\boldsymbol{\sigma} = \begin{pmatrix} \sigma_{11} & & \\ & \sigma_{22} & \\ & & \sigma_{33} \end{pmatrix}$. Similar

expressions can be derived for diffusivity in the (100) and (010) directions.

Computing diffusivities at different stress states facilitates the integration in eq.(6.19); for instance, under hydrostatic stress, $\boldsymbol{\sigma} = -P\mathbf{I}$, the trace of \mathbf{V}^m is readily computed as:

$$\int_0^{-P} (V_{\parallel}^m + 2V_{\perp}^m) dP = k_B T [\ln(D(P)) - \ln(D(0))], \quad (6.20)$$

whereas computing diffusivities under uniaxial stress, $\sigma_{33} = \sigma, \sigma_{11} = \sigma_{22} = 0$, allows the anisotropy in the migration volume tensor to be measured:

$$\begin{aligned} \int_0^{\sigma} V_{\parallel}^m d\sigma &= k_B T [\ln(D_i(\sigma)) - \ln(D_i(0))] \\ \int_0^{\sigma} V_{\perp}^m d\sigma &= k_B T [\ln(D_j(\sigma)) - \ln(D_j(0))] \end{aligned}, \quad (6.21)$$

where i is the (001) direction and j is either the (100) or (010) directions.

6.3 Computational Details

Molecular statics simulations were performed to compute relaxation volumes. The relaxation volume, V^r , was computed by calculating the volume difference between relaxed configurations with and without a point defect, at various stress states. The defect configuration was chosen to correspond to the ground state (minimum energy configuration). The ground state configuration was found by performing molecular dynamics simulations with periodic quenches. The relaxations were performed via molecular statics energy minimization at a specified stress state, using the conjugate gradient method with an energy tolerance of 1×10^{-14} for changes between successive iterations [86]. The lattice site volume, Ω , was nearly constant across all stress ranges and potentials, and, for simplicity, was assumed to be 20 \AA^3 for Si and 22 \AA^3 for Ge.

Migration volume tensor components were estimated with molecular dynamics simulations in the *NST* ensemble based on the Nose-Hoover barostat and thermostat in the LAMMPS package [86]. A 1 fs timestep was used for all calculations, and trajectories were generated over 10 ns, with configurations stored every 10 ps. In this setup, the mean-squared displacement (MSD) of all of the atoms is equal to the mean-squared displacement of the defect (as the MSD of a perfect crystal is negligible). MSD was computed as a function of lag time, ranging from 2 ns to 8 ns. Nine independent trajectories were averaged in all calculations. Note that the diffusivity of a defect in a given direction is $\frac{1}{2}$ the slope of MSD versus lag time in that direction. All simulations were performed using a perfect simulation box containing 216 atoms, with defect systems measuring 215 atoms (vacancy) or 217 atoms (interstitial). This size was chosen in accordance with previous studies [77, 78] to eliminate system size effects.

Several popular empirical potentials were studied. For Si, these included the Tersoff interatomic potential (T3) [88], the Erhart-Albe reparameterization of the Tersoff potential (T-EA) [124], the Environment-Dependent Interatomic Potential (EDIP) [125], the Stillinger-Weber interatomic potential (SW) [126], and the modified embedded atom method (MEAM) [127]. For Ge, the T3 potential was used [88].

6.4 Results

6.4.1 Quantitative Analysis of Formation Volume Tensor

To measure the impact of stress on concentration, we fit the relaxation volumes for a given defect and a given potential model obtained at different uniaxial stress values to a polynomial, and then integrated the expression to obtain, per eq. (6.8),

$$\int_0^\sigma \frac{V^r}{3} d\sigma, \quad (6.22)$$

where σ is the value of uniaxial stress. The actual relaxation volume values are listed in Appendix 1. The resulting expressions of the fits of eq. (6.22) are listed in Table 6.1 for all potentials and defect types. The derivatives of the polynomial fits with respect to stress in Table 6.1 therefore directly provide $V^r / 3$. We use the polynomial fits in Table 6.1 for all results in this Chapter.

Table 6.1. Defect concentration stress dependence, computed via molecular statics simulations. The equation model is $a\sigma^4 + b\sigma^3 + c\sigma^2 + d\sigma + e$, with σ in GPa. Note that e always is zero. See text for details on computation.

Potential (Type)	$\int_0^\sigma \frac{V^r}{3} d\sigma$ (eV)			
	a	b	c	d
T3 (Si) (I)	-2.26×10^{-7}	-7.26×10^{-6}	6.16×10^{-5}	3.44×10^{-2}
T-EA (I)	-1.40×10^{-7}	-3.92×10^{-6}	-1.50×10^{-4}	5.36×10^{-2}
EDIP (I) (Top is $\sigma > 0$, Bottom is $\sigma < 0$)	6.04×10^{-6}	-1.02×10^{-4}	3.56×10^{-4}	5.90×10^{-2}
	1.32×10^{-5}	2.69×10^{-4}	2.18×10^{-3}	5.83×10^{-2}
SW (I)	-6.18×10^{-7}	-1.21×10^{-6}	4.46×10^{-4}	5.52×10^{-2}
MEAM (I)	4.59×10^{-6}	2.27×10^{-5}	-6.29×10^{-4}	6.65×10^{-2}
T3 (Ge) (I)	-3.94×10^{-7}	-1.81×10^{-5}	2.72×10^{-4}	7.04×10^{-2}
T3 (Si) (V) (Top is $\sigma > 0$, Bottom is $\sigma < 0$)	1.16×10^{-7}	-2.00×10^{-5}	-8.29×10^{-5}	-5.38×10^{-2}
	-5.03×10^{-6}	-1.18×10^{-4}	-6.66×10^{-5}	-5.37×10^{-2}
T-EA (V)	-3.60×10^{-7}	3.03×10^{-6}	-4.66×10^{-4}	-1.32×10^{-2}
EDIP (V)	-3.76×10^{-7}	8.31×10^{-6}	-4.51×10^{-4}	1.83×10^{-2}
SW (V)	2.02×10^{-7}	-1.51×10^{-5}	2.92×10^{-4}	-7.01×10^{-2}
MEAM (V)	-1.14×10^{-6}	1.37×10^{-5}	-5.99×10^{-5}	-3.32×10^{-2}
T3 (Ge) (V)	-4.13×10^{-7}	-2.07×10^{-6}	6.77×10^{-4}	-6.08×10^{-2}

Shown in Table 6.2 are several literature estimates for the trace of the formation volume tensor, $tr(\mathbf{V}^r)$ for Si self-interstitials and vacancies. With the exception of ref. [78], all of these studies estimated $tr(\mathbf{V}^r)$ at zero stress. In ref. [78], $tr(\mathbf{V}^r)$ was computed across a range of hydrostatic pressures. Note that the single empirical potential literature estimate (EDIP) strongly deviates from the consensus value of about -19 \AA^3 (vacancies) and 14 \AA^3 (interstitials) for the quantum mechanical calculations.

A comparison between the present empirical potential calculations and the literature estimates is shown in Figure 6.2. The dashed black line shows the average value of the quantum mechanical literature values, while the solid black line shows the pressure-dependent results obtained in ref. [78]. The various colored lines represent the present results. The different potentials give very different predictions for both defect species, highlighting the challenge for empirical potentials to capture lattice relaxations around point defects. In fact, most potentials appear to predict the wrong sign for $tr(\mathbf{V}^f)$ as compared to the consensus quantum mechanical estimate for vacancies. It is impossible to unequivocally assign a single potential model as ‘best’, although the T3 potential appears to give a reasonable picture for both point defect species.

Table 6.2. Traces of relaxation volume tensor for Si as previously reported in the literature. All values correspond to zero hydrostatic pressure.

$tr(\mathbf{V}_I^r)(\text{\AA}^3)$	$tr(\mathbf{V}_V^r)(\text{\AA}^3)$	Method	Source
28.7	8.8	EDIP	[74]
18.17	-19.58	Tight-Binding MD	[79]
12.0006	-21.7638	DFT	[75]
	-15.5	DFT	[77]
11.292	-24.105	DFT	[78]
	-22	DFT	[80]
	-12.2	Hartree-Fock	[128]

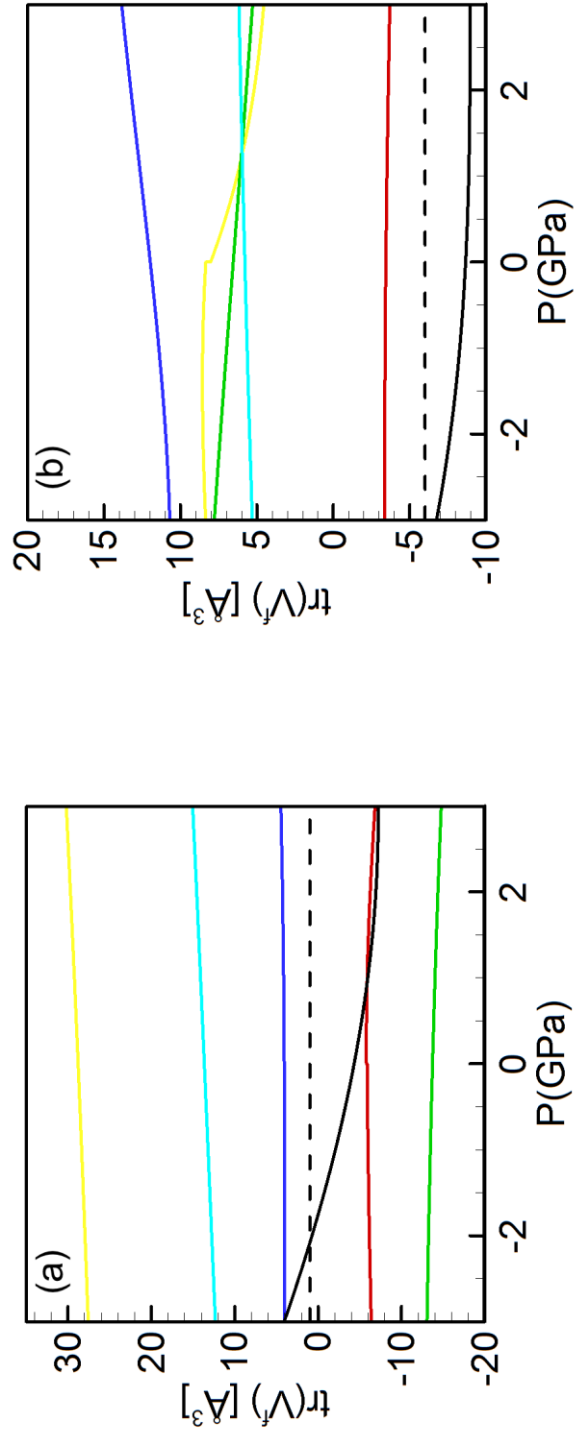


Figure 6.2. $tr(\mathbf{V}^f) = V^r \pm \Omega$ (positive for vacancies) for (a) Si vacancies and (b) Si interstitials. Red = T3, yellow = EDIP, green = SW, light blue = T-EA, dark blue = MEAM, black dashed line = average of literature values, black solid line = fit to data from ref. [78].

6.4.2 Quantitative Analysis of Migration Volume Tensor

While all relaxation volumes were computed at zero temperature, migration volumes were calculated based on atomic diffusion at finite temperature. It is a well-known fact that some empirical potentials predict melting temperatures that are very different from the experimental value (~ 1683 K). In order to make a consistent comparison across potentials, all temperatures reported here were scaled to the melting temperature for each potential. The temperature ranges considered for these calculations (Table 6.3) were rather narrow due to the difficulty associated with obtaining sufficient atomic diffusion at lower temperatures.

Shown in Table 6.4 are polynomial fits for integrals of the migration volumes as functions of the stress parallel and perpendicular to the migration, computed using simulations performed at constant uniaxial stress. Appendix 1 lists all of the actual diffusion constants we computed. Note that all of the polynomial fits correspond to diffusion data at the single temperature of $0.9T_m$ for all potential models. As shown previously in eqs. (6.21), these polynomial fits may be used to directly obtain the migration volume terms by differentiation.

Table 6.3. Temperatures considered when conducting molecular dynamics, along with the melting temperatures for the potentials used in the calculation. The melting temperature found experimentally is 1683 K for silicon and 1210 K for germanium, as stated in ref. [129].

Potential	Element	T_m (K)	T (T_m)
T3	Si	2547 [129]	0.84, 0.86, 0.88
T-EA	Si	2450 [124]	0.88, 0.90, 0.92
EDIP	Si	1572 [130]	0.92, 0.95, 0.99
SW	Si	1688 [129]	0.86, 0.89, 0.92
MEAM	Si	1411 [131]	0.90
T3	Ge	2554 [129]	0.84, 0.86, 0.88

Table 6.4. Defect diffusivity stress dependence, computed via molecular dynamics simulations. The equation model is $a\sigma^4 + b\sigma^3 + c\sigma^2 + d\sigma + e$, with σ in GPa. Note that e always is zero. See text for details on computation.

Potential (Type)	$\int_0^\sigma V_{\parallel}^m d\sigma$ (eV)			
	a	b	c	d
T3 (Si) (I)	0	-5.09×10^{-4}	-3.41×10^{-3}	8.20×10^{-3}
T-EA (I)	0	-7.32×10^{-5}	-1.00×10^{-3}	1.53×10^{-3}
EDIP (I)	0	-2.26×10^{-4}	-1.76×10^{-3}	3.88×10^{-3}
SW (I)	0	-5.79×10^{-4}	-3.98×10^{-3}	-9.54×10^{-4}
MEAM (I)	0	-7.79×10^{-4}	3.06×10^{-3}	1.93×10^{-2}
T3 (Ge) (I)	0	2.02×10^{-3}	-7.69×10^{-4}	6.83×10^{-4}
T3 (Si) (V)	0	1.24×10^{-3}	4.14×10^{-4}	-4.70×10^{-2}
T-EA (V)	0	8.65×10^{-5}	-1.40×10^{-3}	-3.06×10^{-2}
EDIP (V)	0	1.65×10^{-4}	-3.96×10^{-3}	-2.68×10^{-2}
SW (V)	0	-1.67×10^{-5}	2.19×10^{-3}	6.96×10^{-3}
MEAM (V)	0	1.47×10^{-3}	-1.89×10^{-3}	3.92×10^{-3}
T3 (Ge) (V)	0	8.00×10^{-5}	-1.46×10^{-3}	-3.65×10^{-2}

Potential (Type)	$\int_0^\sigma V_\perp^m d\sigma$ (eV)			
	<i>a</i>	<i>b</i>	<i>c</i>	<i>d</i>
T3 (Si) (I)	0	-2.51×10^{-4}	-1.98×10^{-3}	2.42×10^{-3}
T-EA (I)	0	-1.22×10^{-4}	-3.53×10^{-4}	3.03×10^{-3}
EDIP (I)	0	-2.92×10^{-4}	-1.34×10^{-3}	5.05×10^{-3}
SW (I)	0	-1.62×10^{-3}	-2.32×10^{-3}	1.54×10^{-3}
MEAM (I)	0	1.05×10^{-4}	4.19×10^{-3}	1.29×10^{-2}
T3 (Ge) (I)	0	-2.02×10^{-4}	-1.34×10^{-3}	2.18×10^{-3}
T3 (Si) (V)	0	1.59×10^{-3}	-1.40×10^{-4}	-5.56×10^{-2}
T-EA (V)	0	6.21×10^{-5}	-1.36×10^{-3}	-3.32×10^{-2}
EDIP (V)	0	5.02×10^{-4}	-3.92×10^{-3}	-3.59×10^{-2}
SW (V)	0	1.14×10^{-4}	2.26×10^{-3}	4.80×10^{-4}
MEAM (V)	0	3.81×10^{-4}	-1.53×10^{-3}	2.98×10^{-3}
T3 (Ge) (V)	0	-1.04×10^{-4}	-1.02×10^{-3}	-3.83×10^{-2}

Figure 6.3(a-b) compares the trace of the formation volume tensor values for Si vacancies and interstitials as a function of hydrostatic pressure. For interstitials, all of the potentials, except for MEAM and SW, are in good agreement, even across atom types. For vacancies, however, there is little agreement between any of the potentials. One

unexpected result is that the sign is generally negative for both defect types, indicating that the lattice relaxes inward during defect diffusion, regardless of the species. According to ref. [32] and our literature review, migration volume is very often neglected in calculations of stress-altered diffusion. However, it is clear from the magnitude of these volumes that the impact of migration volume should not be neglected in these calculations.

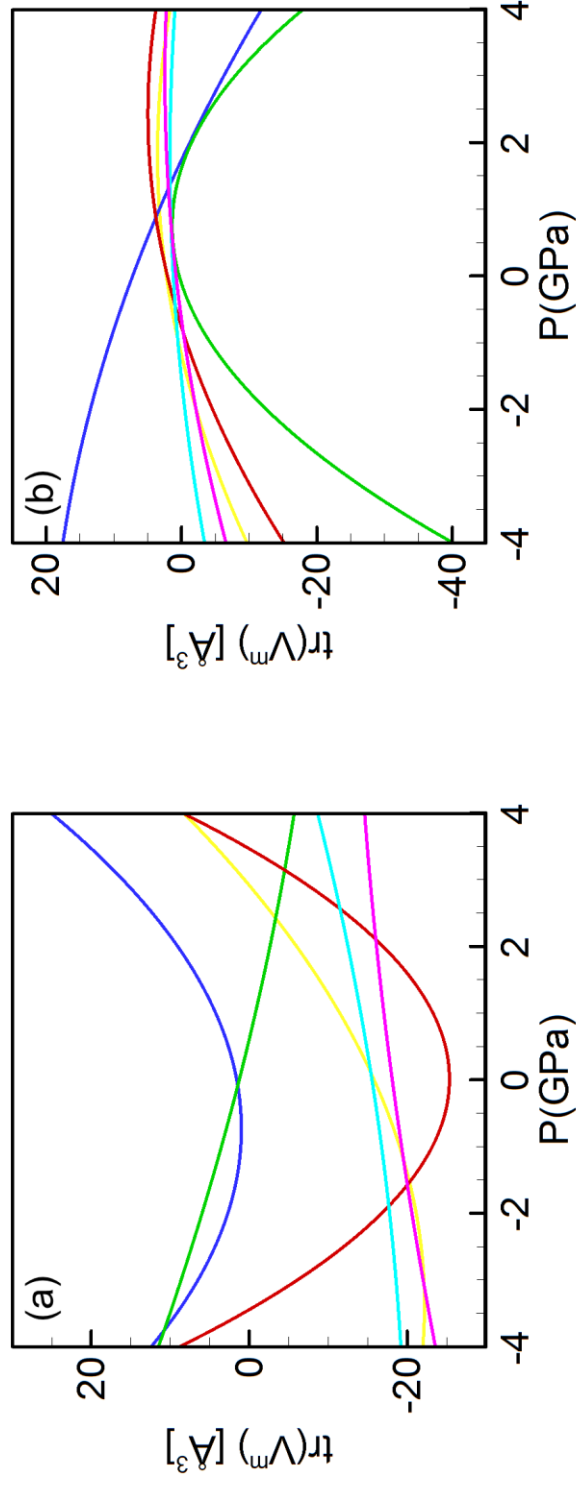


Figure 6.3. $tr(\mathbf{V}^m)$ for (a) vacancies and (b) interstitials. Red = T3 (Si), yellow = EDIP, green = SW, light blue = T-EA, dark blue = MEAM, purple = T3 (Ge).

The temperature dependence of the migration volume tensor was assessed by computing

$$\frac{d(\text{tr}(\mathbf{V}^m))}{dT} \quad (6.23)$$

for the temperatures studied. The results are plotted in Figure 6.4 at 5 pressures. At pressures less than 1 GPa in magnitude, the migration volume appears to be relatively constant with temperature. However, the temperature dependence of migration volume becomes far more pronounced at higher pressures.

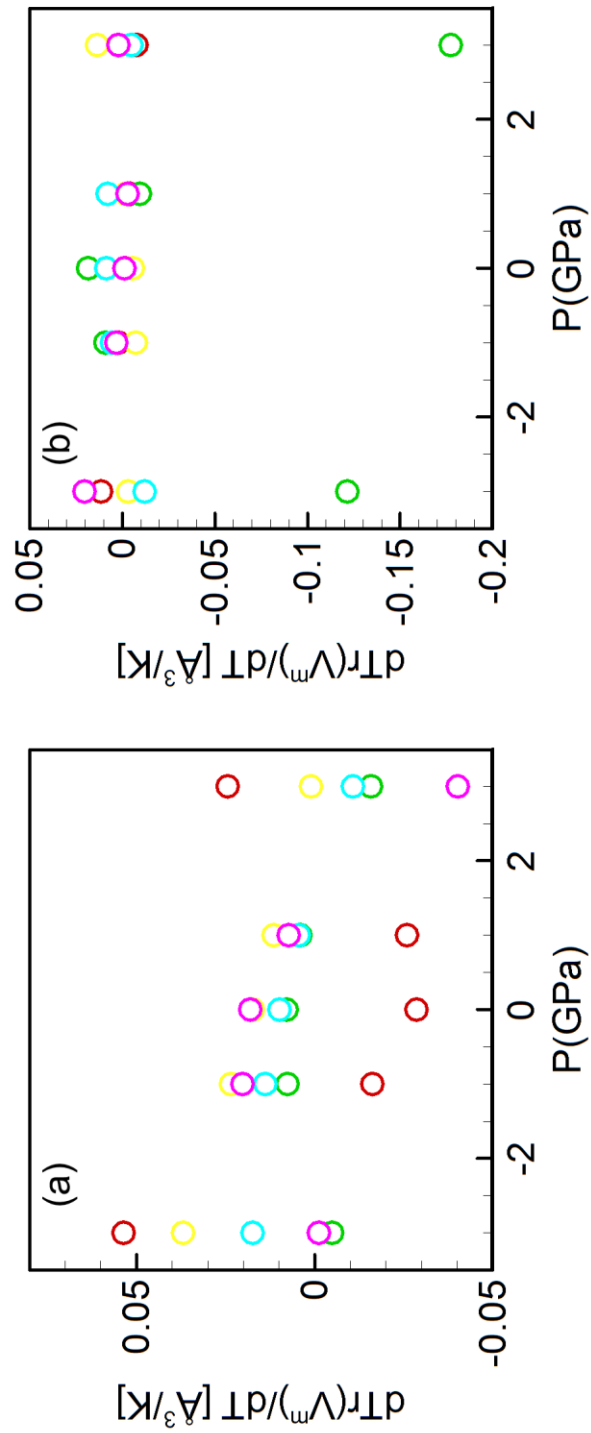


Figure 6.4. $d(\text{tr}(\mathbf{V}^m))/dT$ for (a) vacancies and (b) interstitials. Red = T3 (Si), yellow = EDIP, green = SW, light blue = T-EA, purple = T3 (Ge).

6.4.3 Impact of Different Stress States on Atomic Diffusion

The importance of the stress dependence of point defect diffusion lies in the tight coupling to atomic diffusion in solids: Point defect diffusivity is related to atomic diffusivity, D_a , through [38]

$$D_a = \sum_{A=I,V} f_A D_A \frac{C_A}{C_a}, \quad (6.24)$$

where f_A is a correlation factor for defect hops and C_a is the atomic density. This expression is a normalized “transport capacity,” as the product of diffusivity and concentration is the relevant quantity to overall atomic diffusion (see Chapter 3).

We therefore consider the product of eqs. (6.6) and (6.17), which leads to, upon integration,

$$\begin{aligned} \frac{DC_{001}(\boldsymbol{\sigma})}{DC_{001}(\mathbf{0})} &= \exp\left(\beta \left[\int_0^{\sigma_{ij}} V_{ij}^f d\sigma_{ij} + \int_0^{\sigma_{ij}} V_{001,ij}^m d\sigma_{ij} \right]\right) \\ &= \exp\left(\beta \left[\int_0^{\sigma_{33}} \pm \Omega d\sigma_{33} + \int_0^{\sigma_{11}} \frac{V^r}{3} d\sigma_{11} + \int_0^{\sigma_{22}} \frac{V^r}{3} d\sigma_{22} + \int_0^{\sigma_{33}} \frac{V^r}{3} d\sigma_{33} \right]\right), \quad (6.25) \\ &x \exp\left(\beta \left[\int_0^{\sigma_{11}} V_{\perp}^m d\sigma_{11} + \int_0^{\sigma_{22}} V_{\perp}^m d\sigma_{22} + \int_0^{\sigma_{33}} V_{\parallel}^m d\sigma_{33} \right]\right) \end{aligned}$$

for each defect type, where $\beta \equiv (k_B T)^{-1}$, given a generalized stress tensor

$$\boldsymbol{\sigma} = \begin{pmatrix} \sigma_{11} & & \\ & \sigma_{22} & \\ & & \sigma_{33} \end{pmatrix}. \text{ Similar expressions can be derived for diffusivity in the (100) and}$$

(010) directions.

Figure 6.5, Figure 6.6, and Figure 6.7 show how diffusivity is altered by stress in various stress states from values computed in this work for both silicon and germanium.

In cases where it is possible to have anisotropic diffusion (biaxial and uniaxial stress), most of the measurements of diffusivity of both interstitials and vacancies are at most weakly anisotropic. Also, it should come as no surprise that all potentials show fairly good agreement for the uniaxial case, as the site volume Ω , which is constant across potentials (and nearly the same for both Si and Ge), is far more dominant in the computed values than in the other cases.

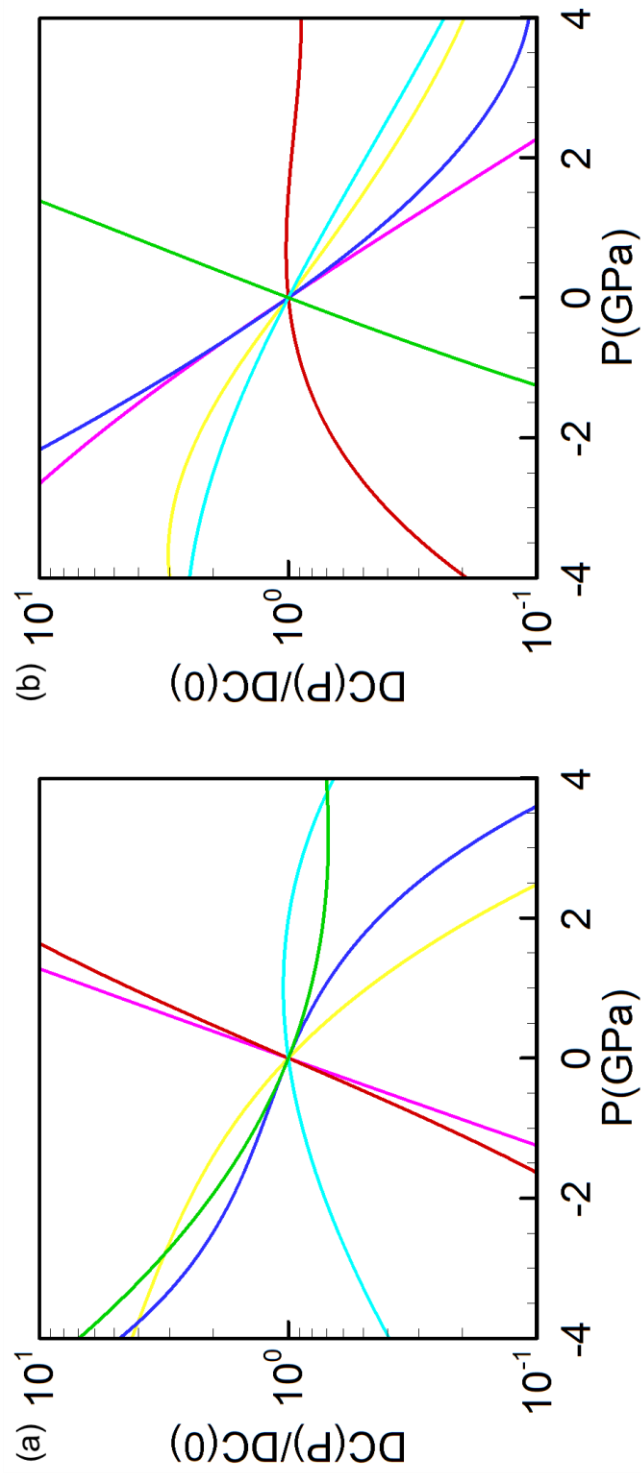


Figure 6.5. Values of $DC(P)/DC(0)$ under hydrostatic stress for (a) vacancies and (b) interstitials, for silicon and germanium as computed in this work. Red = T3(Si), purple = T3(Ge), yellow = SW, green = EDIP, light blue = T-EA, dark blue = MEAM. Diffusion is isotropic under hydrostatic stress [32].

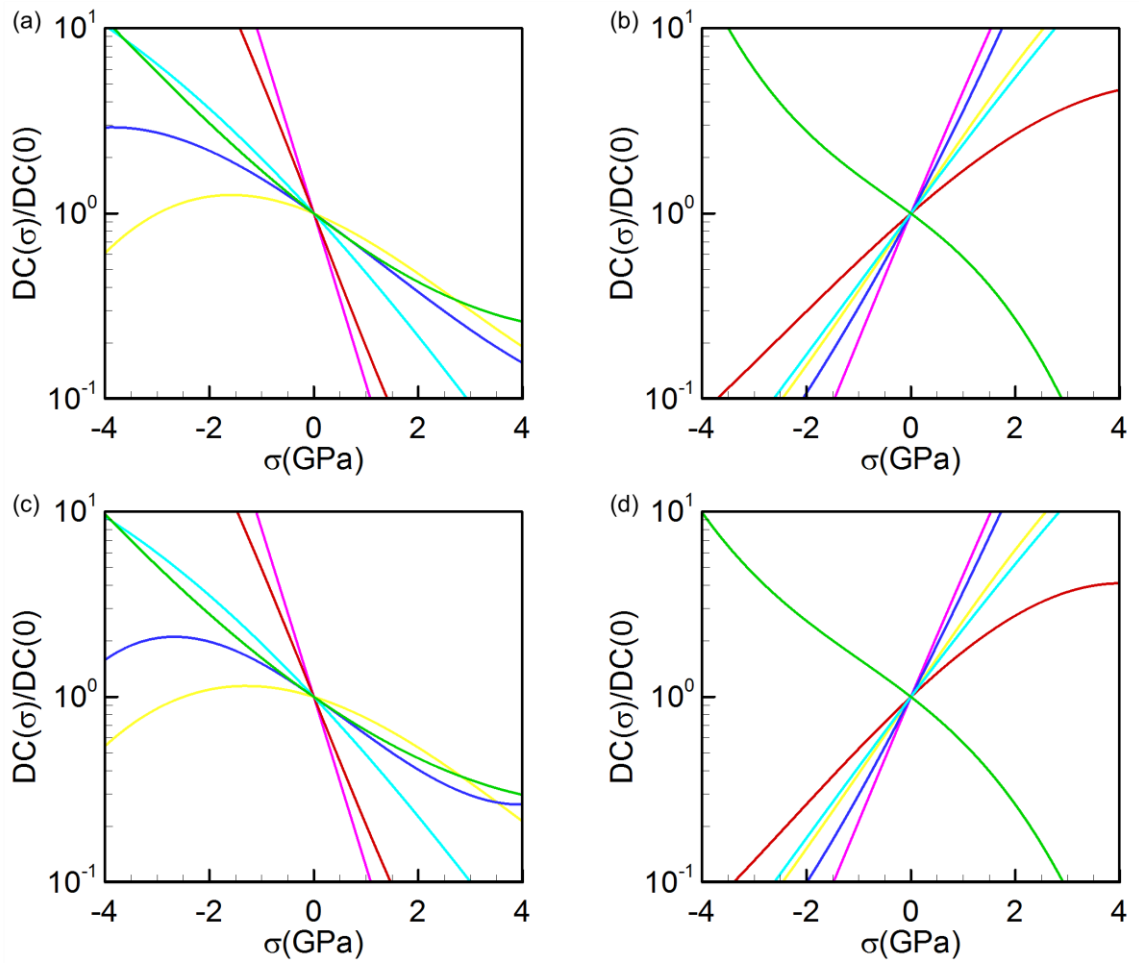


Figure 6.6. Values of $DC_{001}(\boldsymbol{\sigma})/DC(\mathbf{0})$ under biaxial stress, $\sigma_{11} = \sigma_{22} = \sigma, \sigma_{33} = 0$, for (a) vacancies and (b) interstitials, and values of $DC_{100}(\boldsymbol{\sigma})/DC(\mathbf{0}) = DC_{010}(\boldsymbol{\sigma})/DC(\mathbf{0})$ for (c) vacancies and (d) interstitials, for Si and Ge as computed in this work. Red = T3(Si), purple = T3(Ge), yellow = EDIP, green = SW, light blue = T-EA, dark blue = MEAM.

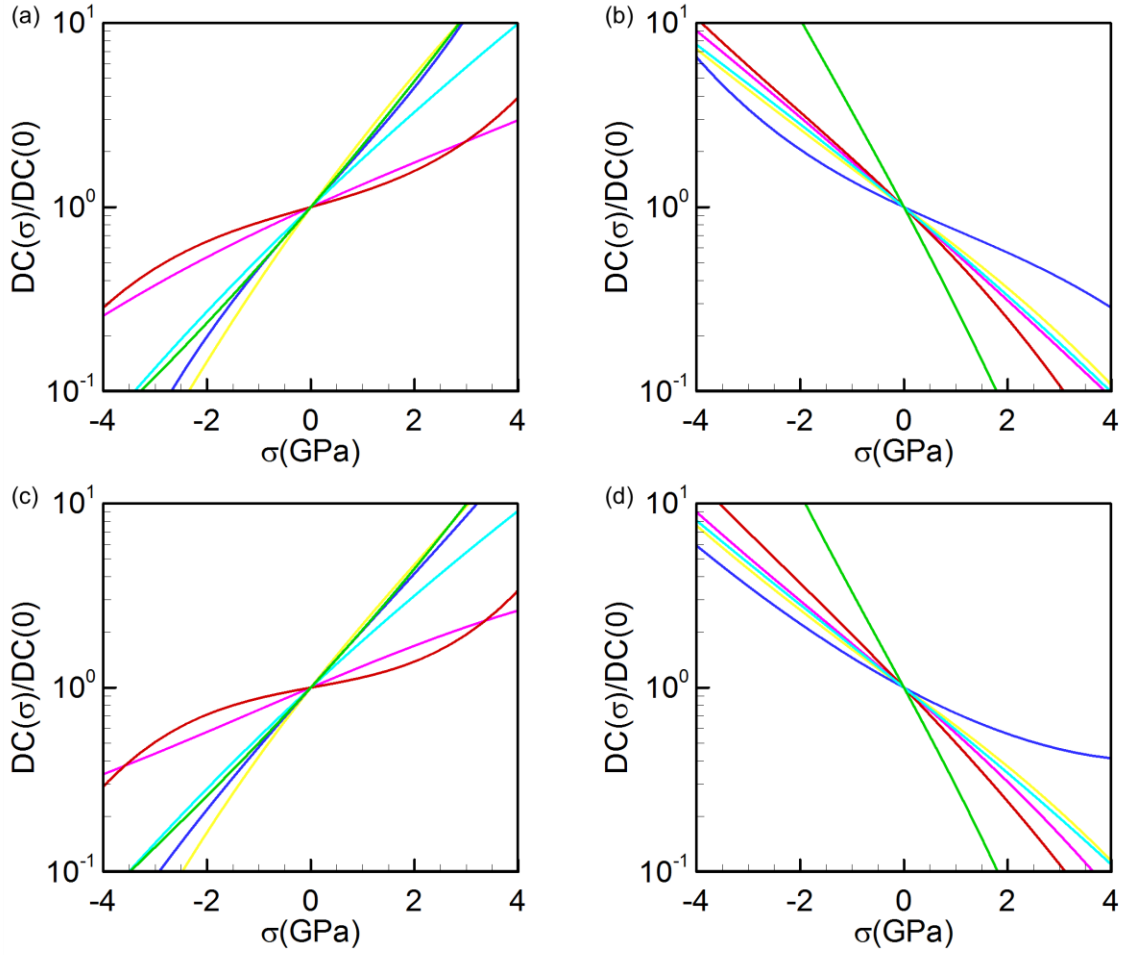


Figure 6.7. Values of $DC_{001}(\boldsymbol{\sigma})/DC(\mathbf{0})$ under uniaxial stress, $\sigma_{33} = \sigma, \sigma_{11} = \sigma_{22} = 0$, for (a) vacancies and (b) interstitials, and values of $DC_{100}(\boldsymbol{\sigma})/DC(\mathbf{0}) = DC_{010}(\boldsymbol{\sigma})/DC(\mathbf{0})$ for (c) vacancies and (d) interstitials, for Si and Ge as computed in this work. Red = T3(Si), purple is T3(Ge), yellow = EDIP, green = SW, light blue = T-EA, dark blue = MEAM.

For the case of biaxial stress, relevant in lattice mismatched film growth [38], and the only case presented where the site volume does not impact the calculations, all of the potentials except for EDIP agree that vacancy diffusion is enhanced by negative (compressive) stress and hindered by positive (tensile) stress. However, with the exception of SW, all of the potentials say the opposite for interstitial diffusion.

6.5 Conclusions

We have measured crucial parameters that quantify the impact of diffusion in Si and Ge using molecular dynamics and statics calculations with a range of popular interatomic potentials. There is, in general, widespread disagreement between the potentials. However, in some calculations, particularly in the impact of stress on atomic diffusion under uniaxial stress, all of the interatomic potentials generally agree.

It is clear, given the discrepancies in the computed values, that molecular simulations alone cannot definitively provide activation volume measurements. Some cleverly designed experiments are needed to further address this issue (see, e.g., ref. [32]). However, the computational toolkit described in this work hopefully provides a straightforward path to collaborating with and expanding upon experimental studies.

Chapter 7. Conclusions and Future Work

7.1 Summary

In this thesis, I have presented a novel approach to generating compositional patterns in the near-surface region of a thin semiconductor alloy that can potentially be useful in next-generation quantum dot (QD) technology. In Chapter 1, I describe how quantum confinement is important to a wide range of modern technologies, and how current manufacturing techniques are incapable of reliably generating QDs with the spatial and size uniformity required to enable addressability necessitated by future QD applications. I review some recent approaches to generating said addressable QDs, that try to control surface growth mechanisms in lattice mismatched semiconductors. These results, due to the highly driven nature of the nucleation processes that occur during surface growth, are generally insufficient to adequately guide the formation of uniform QDs. Another approach [29], however, using thin stressors on the surface of a binary GaAs alloy, is shown to cause the formation of relatively uniform As precipitates in matrix, aligned with the stressors. While promising, the nucleation process that governs the precipitate formation is nevertheless inherently stochastic, as in the other demonstrations described above. However, this result is the primary motivation for this thesis.

In Chapter 2, I present a recent experimental demonstration that shows that applying a spatially varying stress field in a SiGe film via nanoindentation, followed by a period of annealing at elevated temperatures, leads to larger Ge atoms preferentially diffusing away from the regions of high compressive stress, leaving behind areas of elevated Si concentration. The patterned regions of variable composition, resulting from

diffusion and not nucleation, are therefore not subject to the limitations in previous demonstrations. While these experiments are exciting proof of our main hypothesis that compositional redistribution will result from the diffusion of lattice mismatched atoms in the presence of spatially variable stress, conducting and analyzing these experiments at many different conditions will be extremely difficult and costly. Thus, developing a computational model to direct experiments to the appropriate conditions to generate desirable compositional patterns is the main purpose of this thesis.

In Chapter 3, I review the available computational techniques and approaches that could potentially be useful in such a computational model. The length and time scales considered experimentally that I want to simulate in the model I eventually develop are far too long for methods that fully resolve all atomic details in the film (i.e., quantum mechanical and molecular dynamics techniques). More coarse-grained approaches, using lattice kinetic Monte Carlo (LKMC) or phase field methodology, are capable of modeling the required length and time scales at desirable resolution. In addition, because I am considering the SiGe heterosystem in this thesis, LKMC is the immediate and obvious choice of methodology to use in the model, due to the previous parameterization in the literature of a LKMC model to describe interdiffusion in biaxially strained SiGe/Si heterojunctions [38]. While most of the parametric space was determined by fitting relevant quantities to experimental measurements, one crucial subset of parameters, the so-called “activation volumes” that determine how diffusivity changes with stress, are not very well-known from either theory or experiments [32]. These parameters determine the overall timescale for interdiffusive processes. In Chapter 6, I list the discrepancies in previous calculations in the literature, and illustrate, via molecular statics and dynamics

calculations, a lack of agreement among a wide range of interatomic potentials that are usually far more accurate and consistent when used to compute material properties.

Chapter 4 of this thesis details the interdiffusion model mentioned above, and to extend the model to consider interdiffusion in arbitrary stress states. Using molecular statics calculations, I am able to parametrize the relative diffusivities of the larger Ge and smaller Si atoms away from areas of compressive stress. In addition, by using continuum stress calculations validated against molecular statics indentation simulations, I am able to generate stress fields in thin SiGe films that result from simple indenter geometries (i.e., spherical and cylindrical indenter shapes). The SiGe film is divided up into cells, with the state of each cell defined by composition and stress level within the cell. Diffusion in the film is achieved by performing atomic exchanges between neighboring cells. LKMC simulations of annealing are conducted at a small set of different contact pressures, indenter pitches, and temperatures. These preliminary simulations illustrate how annealing at different regions of the parametric space comprised of indenter pitch, shape, contact pressure, and much more, lead to vastly different resulting compositional patterns in the near-surface region of the film.

Chapter 5 of this thesis explores more of the parametric space governing the compositional redistribution process. By performing target scans of indenter pitch, shape, and array geometry, I am able to generate near-surface regions of nearly pure Ge in a low concentration (20% Ge) SiGe film. This result, while confirming that a wide range of near-surface compositional patterns is obtainable via nanoindentation by tuning the indenter geometry, also is very desirable from a device perspective: Because of the

electronic properties of Si and Ge, quantum confined Ge structures in SiGe are useful, while quantum confined Si structures in SiGe are not.

7.2 Future Work

7.2.1 Optimization of Vast Parametric Space Relevant to Compositional Redistribution

The large parametric space governing the compositional redistribution process explored in Chapters 4 and 5 is far too large to explore via brute force, as the simulations (comprised of computing a stress field and annealing via LKMC) are too expensive to perform ad infinitum. Thus, a targeted optimization approach is required.

One such “coarse-grained optimization” approach relies on the assumption that the high-dimensional, complex parametric space is effectively a simpler one, if we only knew the right way to look at our computational data; that a small number (say a few dozen) features of the complete parametric space really matter; and that we can usefully model the landscape in these important degrees of freedom by a smoother, well-behaved effective landscape. If the search problem is thus effectively simple, then we ‘only’ have to uncover this simplicity: find the right (nonlinear combinations of) search variables that matter; smoothen the gradients in these important directions – and then, traditional optimization techniques could be employed.

Computational experiments would be performed using the simulator presented in this thesis, and the data from them would be processed to detect, on-the-fly, what the right few search directions are, and to estimate on-the-fly the effective (smoothened,

‘trend’) gradients of the objective function in these variables. The algorithmic approach would involve (a) performing several (and parallel) short bursts of traditional local optimization searches, i.e., a few steps of an algorithm like the conjugate gradient method, around a trial set of parameters; (b) processing the high-dimensional brief local paths of these computations through nonlinear data mining techniques to extract the local effective reduced dimensionality of the searches – and the local reduced observables (the right few meaningful search directions that matter); (c) armed with this information, estimating the coarse grained, effective gradients of the reduced landscape in these data-driven variables; and (d) performing a coarse gradient-based descent step in this smoothed, effective landscape, and iterating. By working in few (data-driven) effective search directions, and by now taking much longer (again data-driven, effective, smoothed) descent steps, we are effectively solving a reduced optimization problem without explicitly deriving it first. This coarse-grained optimization can be thought of as a part of the equation-free framework developed by Kevrekidis and co-workers for effective modeling of complex, multiscale systems [132, 133].

7.2.2 Alternative Pathways to Ge Quantum Confined Structure Generation

As an alternative to using the compositional patterns that result from the nanoindentation procedure described in this thesis as QDs, it could be possible to use residual stress fields that result from the said compositional variations generated during indentation to direct Stranski-Krastanov (SK) growth during subsequent epitaxial deposition of Ge on the substrate (see Chapter 1 for more details about epitaxial growth mechanisms). Figure 7.1 shows the residual stress field present in one patterned substrate,

after the indenter is removed. While the stress normal to the traction-free surface (the z -direction) is zero (as expected), there is significant modulation in the other two normal stress components, particularly parallel to the indenter axis (there is ~ 800 MPa of tension in the y -direction in the depletion zone and ~ 600 MPa of compression in the y -direction where there is compositional buildup). The magnitude of these stresses is substantial, and the stresses themselves are spatially varying, in accordance with the compositional patterns created via annealing under the action of the indenter.

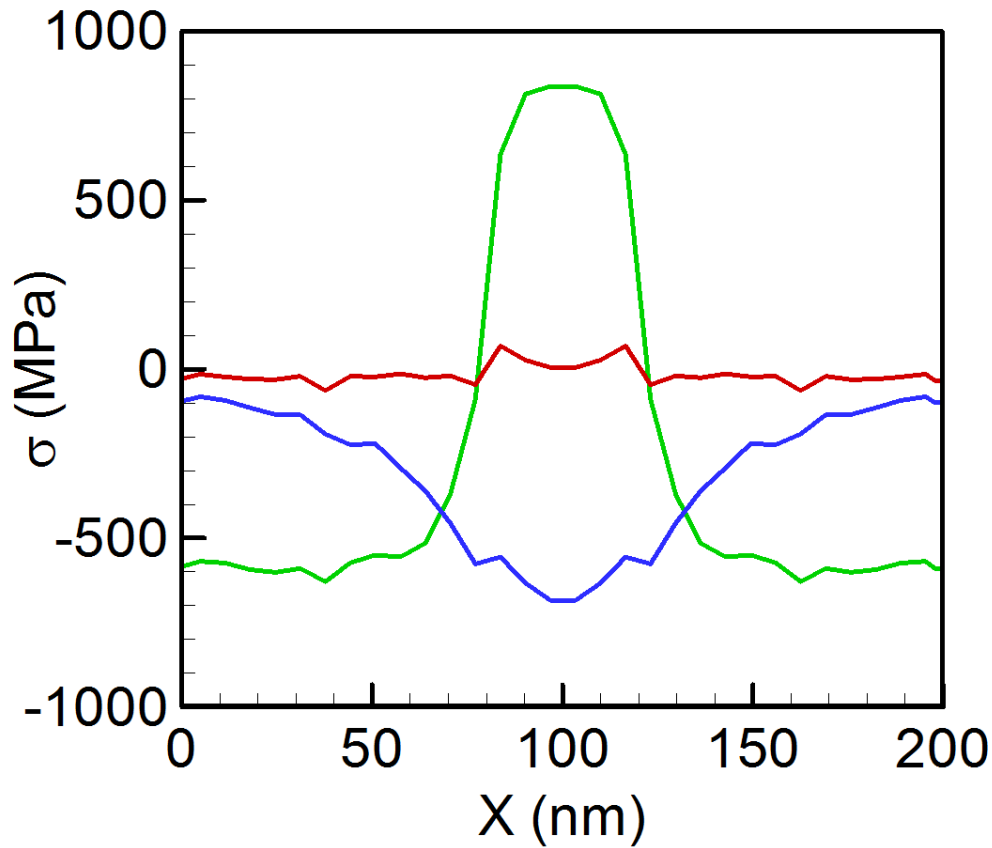


Figure 7.1. Residual hydrostatic stress components along the top layer of LKMC cells following removal of the indenter for the 80 nm-diameter wire indenter (maximum contact pressure of 18 GPa) and annealed at 1000 °C in Chapter 4: red line – σ_{zz} , blue line – σ_{xx} , and green line – σ_{yy} .

There are many approaches to simulate atomic deposition, ranging from continuum methods [134-136], to kinetic Monte Carlo (KMC) [50, 137-139], to direct molecular dynamics (MD) [140, 141]. As discussed in Chapter 3, KMC is most suitable, as it is inherently difficult to capture details of a continuously varying compositional field using continuum approaches, and MD is limited to short length and time scales. There are two possible KMC approaches that could be used: First, adatoms could be added to/hop on a lattice with rates from a pre-generated model [44], e.g. by counting the number of neighboring atoms within a certain distance and fitting the energy for that interaction. The barrier in the hopping rate would be proportional to the sum of these energies. The computational bottleneck in this approach is in the pre-fitting function: If the number of required fitting parameters to adequately model the energy landscape is reasonable, this approach would be appropriate.

A second KMC approach, proposed by Schulze and Smereka [47, 48], measures the barrier for hops via a bond counting scheme for chemical effects and a ball-and-spring model for the elastic effects. The main difference between this approach and the first approach discussed is that the elastic model accounts for all neighbor interactions, obviating the need for potentially unwieldy fitting protocols. Clearly, the bottleneck in this approach is in computing the elastic energy barriers, which, due to the ball-and-spring construction, reduces to solving a set of linear equations for displacements of each particle. This approach is able to achieve islanding during growth, as illustrated in Figure 3.6(c).

7.2.3 Compositional Redistribution in Semiconductor Heterosystems Other Than SiGe

One of the benefits of studying the SiGe heterosystem is the availability of detailed point-defect diffusion models that can be used to develop an interdiffusion simulator, as I have done in this thesis. The principle of stress-driven compositional redistribution is not limited to the SiGe system, however. We should be able to adapt the methodology presented in this thesis to any system that features two compatible, but mismatched, crystalline materials (e.g., InGaAs/GaAs). However, given the lack of detailed, mechanistic diffusion data for most systems other than SiGe, developing a model for other systems will require taking compositional profiles from diffusion experiments conducted under different conditions, and fitting the rates that drive the LKMC simulator to the results. The diffusion profiles measured include the effects of point-defect mediated atomic hops, even if we do not know the exact mechanistic details. For example, we could use interdiffusion across the boundaries of an initially atomically sharp, quantum-well structure as a source of data to which the model will be regressed. By carefully choosing the initial conditions, it will be possible to separate the impact of composition, lattice strain, and temperature on atomic diffusion of the mobile components.

Appendix 1. Results From Activation Volume Studies

Computed Relaxation Volumes

Potential	Type	Uniaxial Stress (GPa)	V^r (Å ³)
T3(Si)	I	-8	5.2132
T3(Si)	I	-6	5.30957
T3(Si)	I	-4	5.39649
T3(Si)	I	-2	5.46834
T3(Si)	I	-1	5.49721
T3(Si)	I	0	5.52023
T3(Si)	I	8	6.15125
T3(Si)	I	6	5.48176
T3(Si)	I	4	5.53734
T3(Si)	I	2	5.54604
T3(Si)	I	1	5.5367
T3(Si)	V	-8	-10.4151
T3(Si)	V	-6	-9.78909
T3(Si)	V	-4	-9.24589
T3(Si)	V	-2	-8.77375
T3(Si)	V	-1	-8.58254
T3(Si)	V	0	-8.6229
T3(Si)	V	8	-9.41311

Potential	Type	Uniaxial Stress (GPa)	V^r (Å ³)
T3(Si)	V	6	-9.11605
T3(Si)	V	4	-8.87799
T3(Si)	V	2	-8.71372
T3(Si)	V	1	-8.66627
EDIP	I	-8	7.72751
EDIP	I	-6	7.8765
EDIP	I	-4	8.18961
EDIP	I	-2	8.46108
EDIP	I	-1	8.56982
EDIP	I	0	9.43049
EDIP	I	8	9.18104
EDIP	I	6	9.266
EDIP	I	4	9.26244
EDIP	I	2	9.58035
EDIP	I	1	9.50914
EDIP	V	-8	4.46393
EDIP	V	-6	3.98791
EDIP	V	-4	3.57998
EDIP	V	-2	3.2342
EDIP	V	-1	3.07712
EDIP	V	0	2.92858

Potential	Type	Uniaxial Stress (GPa)	$V^r (\text{\AA}^3)$
EDIP	V	8	1.90382
EDIP	V	6	2.14741
EDIP	V	4	2.39374
EDIP	V	2	2.65141
EDIP	V	1	2.78702
SW	I	-8	7.86847
SW	I	-6	8.0467
SW	I	-4	8.30503
SW	I	-2	8.58395
SW	I	-1	8.72117
SW	I	0	8.85333
SW	I	8	9.69074
SW	I	6	9.7587
SW	I	4	9.2925
SW	I	2	9.09408
SW	I	1	8.97821
SW	V	-8	-12.5284
SW	V	-6	-12.0684
SW	V	-4	-11.7301
SW	V	-2	-11.4606
SW	V	-1	-11.3462

Potential	Type	Uniaxial Stress (GPa)	V^r (\AA^3)
SW	V	0	-11.2446
SW	V	8	-10.8969
SW	V	6	-10.8982
SW	V	4	-10.9631
SW	V	2	-11.0792
SW	V	1	-11.1557
T-EA	I	-8	7.76002
T-EA	I	-6	8.04475
T-EA	I	-4	7.41462
T-EA	I	-2	8.68391
T-EA	I	-1	8.64138
T-EA	I	0	8.59532
T-EA	I	8	8.04472
T-EA	I	6	8.22051
T-EA	I	4	8.367
T-EA	I	2	8.49057
T-EA	I	1	8.54508
T-EA	V	-8	-0.71053
T-EA	V	-6	-1.1201
T-EA	V	-4	-1.48189
T-EA	V	-2	-1.81074

Potential	Type	Uniaxial Stress (GPa)	V^r (Å ³)
T-EA	V	-1	-1.96649
T-EA	V	0	-2.11815
T-EA	V	8	-3.33948
T-EA	V	6	-3.01126
T-EA	V	4	-2.70795
T-EA	V	2	-2.41395
T-EA	V	1	-2.2669
MEAM	I	-3	11.2852
MEAM	I	-2	11.0711
MEAM	I	-1	10.8657
MEAM	I	0	10.6674
MEAM	I	1	10.4738
MEAM	I	2	10.3082
MEAM	I	3	10.2364
MEAM	V	-3	-5.17623
MEAM	V	-2	-5.24322
MEAM	V	-1	-5.28639
MEAM	V	0	-5.31252
MEAM	V	1	-5.32643
MEAM	V	2	-5.33156
MEAM	V	3	-5.33096

Potential	Type	Uniaxial Stress (GPa)	$V^r (\text{\AA}^3)$
T3(Ge)	I	-3	10.9473
T3(Ge)	I	-2	11.0729
T3(Ge)	I	-1	11.1849
T3(Ge)	I	0	11.2809
T3(Ge)	I	1	11.359
T3(Ge)	I	2	11.4181
T3(Ge)	I	3	11.4575
T3(Ge)	V	-3	-10.4087
T3(Ge)	V	-2	-10.1915
T3(Ge)	V	-1	-9.97354
T3(Ge)	V	0	-9.75576
T3(Ge)	V	1	-9.53987
T3(Ge)	V	2	-9.32762
T3(Ge)	V	3	-9.12069

Computed Diffusivities

Potential	Type	T (T _m)	Uniaxial Stress (applied in (001) direction) (GPa)	$k_B T \left[\begin{array}{c} \ln(D_{001}(\sigma)) \\ -\ln(D_{001}(0)) \end{array} \right] (\text{eV})$
T3(Si)	I	0.84	4	-0.05877
T3(Si)	I	0.84	2	-0.01073

Potential	Type	T (T _m)	Uniaxial Stress (applied in (001) direction) (GPa)	$k_B T \left[\begin{array}{c} \ln(D_{001}(\sigma)) \\ -\ln(D_{001}(0)) \end{array} \right]$ (eV)
T3(Si)	I	0.84	1	0.00587
T3(Si)	I	0.84	0	0
T3(Si)	I	0.84	-1	-0.00269
T3(Si)	I	0.84	-2	-0.01448
T3(Si)	I	0.84	-4	-0.04562
T3(Si)	I	0.86	4	-0.06247
T3(Si)	I	0.86	2	-0.01697
T3(Si)	I	0.86	1	-0.00908
T3(Si)	I	0.86	0	0
T3(Si)	I	0.86	-1	-0.00696
T3(Si)	I	0.86	-2	-0.01202
T3(Si)	I	0.86	-4	-0.04696
T3(Si)	I	0.88	4	-0.05731
T3(Si)	I	0.88	2	-0.00819
T3(Si)	I	0.88	1	-0.00116
T3(Si)	I	0.88	0	0
T3(Si)	I	0.88	-1	-0.00583
T3(Si)	I	0.88	-2	-0.01927
T3(Si)	I	0.88	-4	-0.04967

Potential	Type	T (T _m)	Uniaxial Stress (applied in (001) direction) (GPa)	$k_B T \left[\begin{array}{c} \ln(D_{001}(\sigma)) \\ -\ln(D_{001}(0)) \end{array} \right]$ (eV)
T3(Si)	V	0.84	4	-0.15275
T3(Si)	V	0.84	2	-0.08017
T3(Si)	V	0.84	1	-0.03721
T3(Si)	V	0.84	0	0
T3(Si)	V	0.84	-1	0.03591
T3(Si)	V	0.84	-2	0.06896
T3(Si)	V	0.84	-4	0.10316
T3(Si)	V	0.86	4	-0.1839
T3(Si)	V	0.86	2	-0.07306
T3(Si)	V	0.86	1	-0.0364
T3(Si)	V	0.86	0	0
T3(Si)	V	0.86	-1	0.03111
T3(Si)	V	0.86	-2	0.06555
T3(Si)	V	0.86	-4	0.10596
T3(Si)	V	0.88	4	-0.14968
T3(Si)	V	0.88	2	-0.0857
T3(Si)	V	0.88	1	-0.05202
T3(Si)	V	0.88	0	0
T3(Si)	V	0.88	-1	0.03142

Potential	Type	T (T _m)	Uniaxial Stress (applied in (001) direction) (GPa)	$k_B T \left[\begin{array}{c} \ln(D_{001}(\sigma)) \\ -\ln(D_{001}(0)) \end{array} \right]$ (eV)
T3(Si)	V	0.88	-2	0.06532
T3(Si)	V	0.88	-4	0.10449
EDIP	I	0.92	4	-0.0293
EDIP	I	0.92	2	-0.00529
EDIP	I	0.92	1	0.00133
EDIP	I	0.92	0	0
EDIP	I	0.92	-1	-0.00022
EDIP	I	0.92	-2	-0.01467
EDIP	I	0.92	-4	-0.03258
EDIP	I	0.95	4	-0.03267
EDIP	I	0.95	2	-0.00434
EDIP	I	0.95	1	0.0112
EDIP	I	0.95	0	0
EDIP	I	0.95	-1	-0.00133
EDIP	I	0.95	-2	-0.00422
EDIP	I	0.95	-4	-0.0383
EDIP	I	0.99	4	-0.03935
EDIP	I	0.99	2	-0.00837
EDIP	I	0.99	1	0.00026

Potential	Type	T (T _m)	Uniaxial Stress (applied in (001) direction) (GPa)	$k_B T \left[\begin{array}{c} \ln(D_{001}(\sigma)) \\ -\ln(D_{001}(0)) \end{array} \right]$ (eV)
EDIP	I	0.99	0	0
EDIP	I	0.99	-1	-0.00803
EDIP	I	0.99	-2	-0.01049
EDIP	I	0.99	-4	-0.03211
EDIP	V	0.92	4	-0.15534
EDIP	V	0.92	2	-0.0765
EDIP	V	0.92	1	-0.02771
EDIP	V	0.92	0	0
EDIP	V	0.92	-1	0.01443
EDIP	V	0.92	-2	0.03037
EDIP	V	0.92	-4	0.02279
EDIP	V	0.95	4	-0.14549
EDIP	V	0.95	2	-0.07261
EDIP	V	0.95	1	-0.03201
EDIP	V	0.95	0	0
EDIP	V	0.95	-1	0.01443
EDIP	V	0.95	-2	0.02413
EDIP	V	0.95	-4	0.01014
EDIP	V	0.99	4	-0.11958

Potential	Type	T (T _m)	Uniaxial Stress (applied in (001) direction) (GPa)	$k_B T \left[\begin{array}{c} \ln(D_{001}(\sigma)) \\ -\ln(D_{001}(0)) \end{array} \right]$ (eV)
EDIP	V	0.99	2	-0.05861
EDIP	V	0.99	1	-0.0244
EDIP	V	0.99	0	0
EDIP	V	0.99	-1	0.02322
EDIP	V	0.99	-2	0.03008
EDIP	V	0.99	-4	0.0198
SW	I	0.86	4	-0.07778
SW	I	0.86	2	-0.03076
SW	I	0.86	1	-0.01109
SW	I	0.86	0	0
SW	I	0.86	-1	-0.00533
SW	I	0.86	-2	-0.01709
SW	I	0.86	-4	-0.00156
SW	I	0.89	4	-0.06131
SW	I	0.89	2	-0.02191
SW	I	0.89	1	-0.00698
SW	I	0.89	0	0
SW	I	0.89	-1	-0.00461
SW	I	0.89	-2	-0.00911

Potential	Type	T (T _m)	Uniaxial Stress (applied in (001) direction) (GPa)	$k_B T \left[\begin{array}{c} \ln(D_{001}(\sigma)) \\ -\ln(D_{001}(0)) \end{array} \right]$ (eV)
SW	I	0.89	-4	0.01374
SW	I	0.92	4	-0.06383
SW	I	0.92	2	-0.02537
SW	I	0.92	1	-0.00641
SW	I	0.92	0	0
SW	I	0.92	-1	-0.00199
SW	I	0.92	-2	-0.01174
SW	I	0.92	-4	0.00809
SW	V	0.86	4	0.0593
SW	V	0.86	2	0.01604
SW	V	0.86	1	0.00813
SW	V	0.86	0	0
SW	V	0.86	-1	-0.00508
SW	V	0.86	-2	-0.00329
SW	V	0.86	-4	0.00592
SW	V	0.89	4	0.06577
SW	V	0.89	2	0.0228
SW	V	0.89	1	0.01736
SW	V	0.89	0	0

Potential	Type	T (T _m)	Uniaxial Stress (applied in (001) direction) (GPa)	$k_B T \left[\begin{array}{c} \ln(D_{001}(\sigma)) \\ -\ln(D_{001}(0)) \end{array} \right]$ (eV)
SW	V	0.89	-1	-0.00032
SW	V	0.89	-2	-0.00067
SW	V	0.89	-4	0.0117
SW	V	0.92	4	0.05776
SW	V	0.92	2	0.01951
SW	V	0.92	1	0.00432
SW	V	0.92	0	0
SW	V	0.92	-1	-0.01266
SW	V	0.92	-2	-0.00952
SW	V	0.92	-4	0.00456
T-EA	I	0.88	4	-0.00484
T-EA	I	0.88	2	-0.00535
T-EA	I	0.88	1	0.00388
T-EA	I	0.88	0	0
T-EA	I	0.88	-1	-0.0013
T-EA	I	0.88	-2	-0.00646
T-EA	I	0.88	-4	-0.00987
T-EA	I	0.9	4	-0.01726
T-EA	I	0.9	2	-0.00271

Potential	Type	T (T _m)	Uniaxial Stress (applied in (001) direction) (GPa)	$k_B T \left[\begin{array}{c} \ln(D_{001}(\sigma)) \\ -\ln(D_{001}(0)) \end{array} \right]$ (eV)
T-EA	I	0.9	1	-0.00634
T-EA	I	0.9	0	0
T-EA	I	0.9	-1	-0.00319
T-EA	I	0.9	-2	-0.01143
T-EA	I	0.9	-4	-0.01972
T-EA	I	0.92	4	-0.00722
T-EA	I	0.92	2	-0.00267
T-EA	I	0.92	1	0.00249
T-EA	I	0.92	0	0
T-EA	I	0.92	-1	0.00124
T-EA	I	0.92	-2	-0.00598
T-EA	I	0.92	-4	-0.01598
T-EA	V	0.88	4	-0.1416
T-EA	V	0.88	2	-0.06301
T-EA	V	0.88	1	-0.03009
T-EA	V	0.88	0	0
T-EA	V	0.88	-1	0.02724
T-EA	V	0.88	-2	0.06181
T-EA	V	0.88	-4	0.10055

Potential	Type	T (T _m)	Uniaxial Stress (applied in (001) direction) (GPa)	$k_B T \left[\begin{array}{c} \ln(D_{001}(\sigma)) \\ -\ln(D_{001}(0)) \end{array} \right]$ (eV)
T-EA	V	0.9	4	-0.1393
T-EA	V	0.9	2	-0.07085
T-EA	V	0.9	1	-0.02746
T-EA	V	0.9	0	0
T-EA	V	0.9	-1	0.02637
T-EA	V	0.9	-2	0.05487
T-EA	V	0.9	-4	0.09429
T-EA	V	0.92	4	-0.13732
T-EA	V	0.92	2	-0.06387
T-EA	V	0.92	1	-0.02851
T-EA	V	0.92	0	0
T-EA	V	0.92	-1	0.02766
T-EA	V	0.92	-2	0.05293
T-EA	V	0.92	-4	0.0988
MEAM	I	0.9	2	0.0421
MEAM	I	0.9	1	0.01651
MEAM	I	0.9	0	0
MEAM	I	0.9	-1	-0.02055
MEAM	I	0.9	-2	-0.02267

Potential	Type	T (T _m)	Uniaxial Stress (applied in (001) direction) (GPa)	$k_B T \left[\begin{array}{c} \ln(D_{001}(\sigma)) \\ -\ln(D_{001}(0)) \end{array} \right]$ (eV)
MEAM	V	0.9	2	0.0166
MEAM	V	0.9	1	0.01257
MEAM	V	0.9	0	0
MEAM	V	0.9	-1	0.00178
MEAM	V	0.9	-2	-0.02267
T3(Ge)	I	0.84	3	-0.0135
T3(Ge)	I	0.84	2	-0.00755
T3(Ge)	I	0.84	1	0.003036
T3(Ge)	I	0.84	0	0
T3(Ge)	I	0.84	-1	0.002011
T3(Ge)	I	0.84	-2	-0.00854
T3(Ge)	I	0.84	-3	-0.01456
T3(Ge)	I	0.86	3	-0.01423
T3(Ge)	I	0.86	2	-0.00374
T3(Ge)	I	0.86	1	0.005757
T3(Ge)	I	0.86	0	0
T3(Ge)	I	0.86	-1	-0.0022
T3(Ge)	I	0.86	-2	-0.00763
T3(Ge)	I	0.86	-3	-0.01697

Potential	Type	T (T _m)	Uniaxial Stress (applied in (001) direction) (GPa)	$k_B T \left[\begin{array}{c} \ln(D_{001}(\sigma)) \\ -\ln(D_{001}(0)) \end{array} \right]$ (eV)
T3(Ge)	I	0.88	3	-0.01268
T3(Ge)	I	0.88	2	-0.0033
T3(Ge)	I	0.88	1	-0.00497
T3(Ge)	I	0.88	0	0
T3(Ge)	I	0.88	-1	-0.00323
T3(Ge)	I	0.88	-2	-0.01191
T3(Ge)	I	0.88	-3	-0.01536
T3(Ge)	V	0.84	3	-0.11933
T3(Ge)	V	0.84	2	-0.07117
T3(Ge)	V	0.84	1	-0.03556
T3(Ge)	V	0.84	0	0
T3(Ge)	V	0.84	-1	0.04544
T3(Ge)	V	0.84	-2	0.074
T3(Ge)	V	0.84	-3	0.10271
T3(Ge)	V	0.86	3	-0.11387
T3(Ge)	V	0.86	2	-0.06297
T3(Ge)	V	0.86	1	-0.03677
T3(Ge)	V	0.86	0	0
T3(Ge)	V	0.86	-1	0.04037

Potential	Type	T (T _m)	Uniaxial Stress (applied in (001) direction) (GPa)	$k_B T \left[\begin{array}{c} \ln(D_{001}(\sigma)) \\ -\ln(D_{001}(0)) \end{array} \right]$ (eV)
T3(Ge)	V	0.86	-2	0.0794
T3(Ge)	V	0.86	-3	0.10496
T3(Ge)	V	0.88	3	-0.112
T3(Ge)	V	0.88	2	-0.07454
T3(Ge)	V	0.88	1	-0.02736
T3(Ge)	V	0.88	0	0
T3(Ge)	V	0.88	-1	0.0438
T3(Ge)	V	0.88	-2	0.07213
T3(Ge)	V	0.88	-3	0.10405

Potential	Type	T (T _m)	Uniaxial Stress (applied in (001) direction) (GPa)	$k_B T \left[\begin{array}{c} \ln(D_{100/010}(\sigma)) \\ -\ln(D_{100/010}(0)) \end{array} \right]$ (eV)
T3(Si)	I	0.84	4	-0.04431
T3(Si)	I	0.84	2	-0.00504
T3(Si)	I	0.84	1	-0.00134
T3(Si)	I	0.84	0	0
T3(Si)	I	0.84	-1	-0.00313
T3(Si)	I	0.84	-2	-0.01435

Potential	Type	T (T _m)	Uniaxial Stress (applied in (001) direction) (GPa)	$k_B T \left[\begin{array}{l} \ln(D_{100/010}(\sigma)) \\ - \ln(D_{100/010}(0)) \end{array} \right]$ (eV)
T3(Si)	I	0.84	-4	-0.03237
T3(Si)	I	0.86	4	-0.04502
T3(Si)	I	0.86	2	-0.00809
T3(Si)	I	0.86	1	-0.00538
T3(Si)	I	0.86	0	0
T3(Si)	I	0.86	-1	-0.00367
T3(Si)	I	0.86	-2	-0.01453
T3(Si)	I	0.86	-4	-0.03018
T3(Si)	I	0.88	4	-0.04015
T3(Si)	I	0.88	2	-0.00741
T3(Si)	I	0.88	1	0.002025
T3(Si)	I	0.88	0	0
T3(Si)	I	0.88	-1	-0.00393
T3(Si)	I	0.88	-2	-0.01056
T3(Si)	I	0.88	-4	-0.02662
T3(Si)	V	0.84	4	-0.17072
T3(Si)	V	0.84	2	-0.09075
T3(Si)	V	0.84	1	-0.04736
T3(Si)	V	0.84	0	0

Potential	Type	T (T _m)	Uniaxial Stress (applied in (001) direction) (GPa)	$k_B T \left[\begin{array}{l} \ln(D_{100/010}(\sigma)) \\ -\ln(D_{100/010}(0)) \end{array} \right]$ (eV)
T3(Si)	V	0.84	-1	0.04505
T3(Si)	V	0.84	-2	0.07346
T3(Si)	V	0.84	-4	0.12836
T3(Si)	V	0.86	4	-0.1898
T3(Si)	V	0.86	2	-0.08556
T3(Si)	V	0.86	1	-0.03905
T3(Si)	V	0.86	0	0
T3(Si)	V	0.86	-1	0.03982
T3(Si)	V	0.86	-2	0.080445
T3(Si)	V	0.86	-4	0.131015
T3(Si)	V	0.88	4	-0.16001
T3(Si)	V	0.88	2	-0.09623
T3(Si)	V	0.88	1	-0.05521
T3(Si)	V	0.88	0	0
T3(Si)	V	0.88	-1	0.046905
T3(Si)	V	0.88	-2	0.079815
T3(Si)	V	0.88	-4	0.121445
EDIP	I	0.92	4	-0.02154
EDIP	I	0.92	2	-0.00394

Potential	Type	T (T _m)	Uniaxial Stress (applied in (001) direction) (GPa)	$k_B T \left[\begin{array}{l} \ln(D_{100/010}(\sigma)) \\ - \ln(D_{100/010}(0)) \end{array} \right]$ (eV)
EDIP	I	0.92	1	0.003375
EDIP	I	0.92	0	0
EDIP	I	0.92	-1	-0.00535
EDIP	I	0.92	-2	-0.01281
EDIP	I	0.92	-4	-0.02494
EDIP	I	0.95	4	-0.02693
EDIP	I	0.95	2	-0.00829
EDIP	I	0.95	1	-0.00539
EDIP	I	0.95	0	0
EDIP	I	0.95	-1	-0.01043
EDIP	I	0.95	-2	-0.00839
EDIP	I	0.95	-4	-0.03071
EDIP	I	0.99	4	-0.02666
EDIP	I	0.99	2	-0.00772
EDIP	I	0.99	1	-0.00419
EDIP	I	0.99	0	0
EDIP	I	0.99	-1	-0.00916
EDIP	I	0.99	-2	-0.01177
EDIP	I	0.99	-4	-0.03772

Potential	Type	T (T _m)	Uniaxial Stress (applied in (001) direction) (GPa)	$k_B T \left[\begin{array}{l} \ln(D_{100/010}(\sigma)) \\ - \ln(D_{100/010}(0)) \end{array} \right]$ (eV)
EDIP	V	0.92	4	-0.16586
EDIP	V	0.92	2	-0.08904
EDIP	V	0.92	1	-0.03159
EDIP	V	0.92	0	0
EDIP	V	0.92	-1	0.028315
EDIP	V	0.92	-2	0.038345
EDIP	V	0.92	-4	0.04443
EDIP	V	0.95	4	-0.15171
EDIP	V	0.95	2	-0.06962
EDIP	V	0.95	1	-0.03183
EDIP	V	0.95	0	0
EDIP	V	0.95	-1	0.020315
EDIP	V	0.95	-2	0.039175
EDIP	V	0.95	-4	0.039085
EDIP	V	0.99	4	-0.13866
EDIP	V	0.99	2	-0.06687
EDIP	V	0.99	1	-0.02865
EDIP	V	0.99	0	0
EDIP	V	0.99	-1	0.02542

Potential	Type	T (T _m)	Uniaxial Stress (applied in (001) direction) (GPa)	$k_B T \left[\begin{array}{l} \ln(D_{100/010}(\sigma)) \\ - \ln(D_{100/010}(0)) \end{array} \right]$ (eV)
EDIP	V	0.99	-2	0.038985
EDIP	V	0.99	-4	0.040415
SW	I	0.86	4	-0.06177
SW	I	0.86	2	-0.02482
SW	I	0.86	1	-0.00576
SW	I	0.86	0	0
SW	I	0.86	-1	-0.00305
SW	I	0.86	-2	-0.0068
SW	I	0.86	-4	0.026905
SW	I	0.89	4	-0.05122
SW	I	0.89	2	-0.01716
SW	I	0.89	1	0.000935
SW	I	0.89	0	0
SW	I	0.89	-1	-0.00034
SW	I	0.89	-2	0.00171
SW	I	0.89	-4	0.034295
SW	I	0.92	4	-0.04865
SW	I	0.92	2	-0.01757
SW	I	0.92	1	0.00216

Potential	Type	T (T _m)	Uniaxial Stress (applied in (001) direction) (GPa)	$k_B T \left[\begin{array}{l} \ln(D_{100/010}(\sigma)) \\ -\ln(D_{100/010}(0)) \end{array} \right]$ (eV)
SW	I	0.92	0	0
SW	I	0.92	-1	0.005115
SW	I	0.92	-2	0.003995
SW	I	0.92	-4	0.033295
SW	V	0.86	4	0.0389
SW	V	0.86	2	0.00621
SW	V	0.86	1	-0.00158
SW	V	0.86	0	0
SW	V	0.86	-1	-0.00175
SW	V	0.86	-2	0.00402
SW	V	0.86	-4	0.02182
SW	V	0.89	4	0.04775
SW	V	0.89	2	0.009215
SW	V	0.89	1	0.00434
SW	V	0.89	0	0
SW	V	0.89	-1	0.002225
SW	V	0.89	-2	0.006615
SW	V	0.89	-4	0.02466
SW	V	0.92	4	0.03974

Potential	Type	T (T _m)	Uniaxial Stress (applied in (001) direction) (GPa)	$k_B T \left[\begin{array}{l} \ln(D_{100/010}(\sigma)) \\ -\ln(D_{100/010}(0)) \end{array} \right]$ (eV)
SW	V	0.92	2	0.01053
SW	V	0.92	1	0.00036
SW	V	0.92	0	0
SW	V	0.92	-1	-0.00145
SW	V	0.92	-2	0.00607
SW	V	0.92	-4	0.0301
T-EA	I	0.88	4	0.00267
T-EA	I	0.88	2	0.00031
T-EA	I	0.88	1	-0.00077
T-EA	I	0.88	0	0
T-EA	I	0.88	-1	-0.00288
T-EA	I	0.88	-2	-0.00383
T-EA	I	0.88	-4	-0.0112
T-EA	I	0.9	4	-0.00052
T-EA	I	0.9	2	0.00471
T-EA	I	0.9	1	0.005515
T-EA	I	0.9	0	0
T-EA	I	0.9	-1	-0.00613
T-EA	I	0.9	-2	-0.00185

Potential	Type	T (T _m)	Uniaxial Stress (applied in (001) direction) (GPa)	$k_B T \left[\begin{array}{l} \ln(D_{100/010}(\sigma)) \\ -\ln(D_{100/010}(0)) \end{array} \right]$ (eV)
T-EA	I	0.9	-4	-0.0096
T-EA	I	0.92	4	0.003495
T-EA	I	0.92	2	0.004505
T-EA	I	0.92	1	0.00359
T-EA	I	0.92	0	0
T-EA	I	0.92	-1	-0.0045
T-EA	I	0.92	-2	-0.00117
T-EA	I	0.92	-4	-0.00633
T-EA	V	0.88	4	-0.15636
T-EA	V	0.88	2	-0.07575
T-EA	V	0.88	1	-0.04066
T-EA	V	0.88	0	0
T-EA	V	0.88	-1	0.0311
T-EA	V	0.88	-2	0.060205
T-EA	V	0.88	-4	0.107205
T-EA	V	0.9	4	-0.14897
T-EA	V	0.9	2	-0.06695
T-EA	V	0.9	1	-0.03432
T-EA	V	0.9	0	0

Potential	Type	T (T _m)	Uniaxial Stress (applied in (001) direction) (GPa)	$k_B T \left[\begin{array}{l} \ln(D_{100/010}(\sigma)) \\ - \ln(D_{100/010}(0)) \end{array} \right]$ (eV)
T-EA	V	0.9	-1	0.035265
T-EA	V	0.9	-2	0.062685
T-EA	V	0.9	-4	0.108725
T-EA	V	0.92	4	-0.13945
T-EA	V	0.92	2	-0.06745
T-EA	V	0.92	1	-0.02709
T-EA	V	0.92	0	0
T-EA	V	0.92	-1	0.03991
T-EA	V	0.92	-2	0.06589
T-EA	V	0.92	-4	0.117035
MEAM	I	0.9	2	0.035145
MEAM	I	0.9	1	0.000685
MEAM	I	0.9	0	0
MEAM	I	0.9	-1	-0.02531
MEAM	I	0.9	-2	-0.01811
MEAM	V	0.9	2	0.005815
MEAM	V	0.9	1	0.00769
MEAM	V	0.9	0	0
MEAM	V	0.9	-1	0.00097

Potential	Type	T (T _m)	Uniaxial Stress (applied in (001) direction) (GPa)	$k_B T \left[\begin{array}{l} \ln(D_{100/010}(\sigma)) \\ -\ln(D_{100/010}(0)) \end{array} \right]$ (eV)
MEAM	V	0.9	-2	-0.01219
T3(Ge)	I	0.84	3	-0.00927
T3(Ge)	I	0.84	2	-0.00146
T3(Ge)	I	0.84	1	-0.00234
T3(Ge)	I	0.84	0	0
T3(Ge)	I	0.84	-1	-0.00421
T3(Ge)	I	0.84	-2	-0.01002
T3(Ge)	I	0.84	-3	-0.01213
T3(Ge)	I	0.86	3	-0.0029
T3(Ge)	I	0.86	2	-0.00079
T3(Ge)	I	0.86	1	0.000319
T3(Ge)	I	0.86	0	0
T3(Ge)	I	0.86	-1	-0.00095
T3(Ge)	I	0.86	-2	-0.0063
T3(Ge)	I	0.86	-3	-0.01009
T3(Ge)	I	0.88	3	-0.0067
T3(Ge)	I	0.88	2	-5.9×10^{-5}
T3(Ge)	I	0.88	1	0.000384
T3(Ge)	I	0.88	0	0

Potential	Type	T (T _m)	Uniaxial Stress (applied in (001) direction) (GPa)	$k_B T \left[\begin{array}{l} \ln(D_{100/010}(\sigma)) \\ -\ln(D_{100/010}(0)) \end{array} \right]$ (eV)
T3(Ge)	I	0.88	-1	-0.00074
T3(Ge)	I	0.88	-2	-0.00675
T3(Ge)	I	0.88	-3	-0.01107
T3(Ge)	V	0.84	3	-0.1216
T3(Ge)	V	0.84	2	-0.07886
T3(Ge)	V	0.84	1	-0.03648
T3(Ge)	V	0.84	0	0
T3(Ge)	V	0.84	-1	0.050165
T3(Ge)	V	0.84	-2	0.080365
T3(Ge)	V	0.84	-3	0.112788
T3(Ge)	V	0.86	3	-0.11277
T3(Ge)	V	0.86	2	-0.06593
T3(Ge)	V	0.86	1	-0.03551
T3(Ge)	V	0.86	0	0
T3(Ge)	V	0.86	-1	0.048175
T3(Ge)	V	0.86	-2	0.091315
T3(Ge)	V	0.86	-3	0.11501
T3(Ge)	V	0.88	3	-0.1165
T3(Ge)	V	0.88	2	-0.07859

Potential	Type	T (T _m)	Uniaxial Stress (applied in (001) direction) (GPa)	$k_B T \left[\begin{array}{l} \ln(D_{100/010}(\sigma)) \\ -\ln(D_{100/010}(0)) \end{array} \right]$ (eV)
T3(Ge)	V	0.88	1	-0.03031
T3(Ge)	V	0.88	0	0
T3(Ge)	V	0.88	-1	0.044715
T3(Ge)	V	0.88	-2	0.08151
T3(Ge)	V	0.88	-3	0.11392

BIBLIOGRAPHY

1. Anderson, R.L., *Experiments on Ge-GaAs Heterojunctions*, in *Electronic Structure of Semiconductor Heterojunctions*, G. Margaritondo, Editor. 1988, Springer Netherlands: Dordrecht. p. 35-48.
2. Ohta, H., et al., *Fabrication and photoresponse of a pn-heterojunction diode composed of transparent oxide semiconductors, p-NiO and n-ZnO*. Applied Physics Letters, 2003. **83**(5): p. 1029-1031.
3. Hartmann, R., et al., *Low energy response of silicon pn-junction detector*. Nuclear Instruments and Methods in Physics Research Section A: Accelerators, Spectrometers, Detectors and Associated Equipment, 1996. **377**(2): p. 191-196.
4. Ballandras, S., et al., *Deep etch X-ray lithography using silicon-gold masks fabricated by deep etch UV lithography and electroforming*. Journal of Micromechanics and Microengineering, 1995. **5**(3): p. 203.
5. Mochizuki, Y.H., Hiroaki and Y. Misawa, *Method of diffusing aluminum into silicon substrate for manufacturing semiconductor device* 1979, Hitachi, Ltd.: United States.
6. Jeong, M., et al., *Silicon Device Scaling to the Sub-10-nm Regime*. Science, 2004. **306**(5704): p. 2057-2060.
7. Carr, D.W. and H.G. Craighead, *Fabrication of nanoelectromechanical systems in single crystal silicon using silicon on insulator substrates and electron beam lithography*. Journal of Vacuum Science & Technology B, 1997. **15**(6): p. 2760-2763.
8. Moore, G.E., *Cramming More Components Onto Integrated Circuits*. Proceedings of the IEEE, 1998. **86**(1): p. 82-85.
9. Cmglee. Available from: https://en.wikipedia.org/wiki/Semiconductor_device_fabrication#/media/File:Comparison_semiconductor_process_nodes.svg.
10. Eaglesham, D.J. and M. Cerullo, *Dislocation-free Stranski-Krastanov growth of Ge on Si(100)*. Physical Review Letters, 1990. **64**(16): p. 1943-1946.
11. Grundmann, M., et al., *Ultranarrow Luminescence Lines from Single Quantum Dots*. Physical Review Letters, 1995. **74**(20): p. 4043-4046.
12. Ross, F.M., R.M. Tromp, and M.C. Reuter, *Transition states between pyramids and domes during Ge/Si island growth*. Science, 1999. **286**(5446): p. 1931-1934.
13. Mo, Y.W., et al., *Kinetic Pathway in Stranski-Krastanov Growth of Ge on Si(001)*. Physical Review Letters, 1990. **65**(8): p. 1020-1023.
14. Zanardi, P. and F. Rossi, *Quantum information in semiconductors: Noiseless encoding in a quantum-dot array*. Physical Review Letters, 1998. **81**(21): p. 4752-4755.
15. Weinstein, Y.S., C.S. Hellberg, and J. Levy, *Quantum-dot cluster-state computing with encoded qubits*. Physical Review A, 2005. **72**(2): p. 020304.
16. Loss, D. and D.P. DiVincenzo, *Quantum computation with quantum dots*. Physical Review A, 1998. **57**(1): p. 120-126.

17. Raussendorf, R. and H.J. Briegel, *A one-way quantum computer*. Physical Review Letters, 2001. **86**(22): p. 5188-5191.
18. Ledentsov, N.N., *Quantum dot laser*. Semiconductor Science and Technology, 2011. **26**(1): p. 014001.
19. Naoto, H., et al., *Quantum Dot Infrared Photodetector Using Modulation Doped InAs Self-Assembled Quantum Dots*. Japanese Journal of Applied Physics, 1999. **38**(4S): p. 2559.
20. Nozik, A.J., *Quantum dot solar cells*. Physica E: Low-dimensional Systems and Nanostructures, 2002. **14**(1–2): p. 115-120.
21. *The Physics and Engineering of Compact Quantum Dot-based Lasers for Biophotonics*. 2014, Weinheim, Germany: Wiley-VCH.
22. Baribeau, J.M., et al., *Ge dots and nanostructures grown epitaxially on Si*. Journal of Physics: Condensed Matter, 2006. **18**(8): p. R139-R174.
23. Sakamoto, K., et al., *Alignment of Ge three-dimensional islands on faceted Si(001) surfaces*. Thin Solid Films, 1998. **321**(1–2): p. 55-59.
24. Zhang, J.J., et al., *SiGe growth on patterned Si(001) substrates: Surface evolution and evidence of modified island coarsening*. Applied Physics Letters, 2007. **91**(17): p. 173115.
25. Kamins, T.I. and R.S. Williams, *Lithographic positioning of self-assembled Ge islands on Si(001)*. Applied Physics Letters, 1997. **71**(9): p. 1201-1203.
26. Ross, F.M., et al., *In-situ observations of self-assembled island nucleation on patterned substrates*. Philosophical Magazine, 2004. **84**(25-26): p. 2687-2697.
27. Lafontaine, H., et al., *Growth of undulating Si_{0.5}Ge_{0.5} layers for photodetectors at $\lambda=1.55\ \mu\text{m}$* . Journal of Applied Physics, 1999. **86**(3): p. 1287-1291.
28. Schmidt, O.G., et al., *Long-range ordered lines of self-assembled Ge islands on a flat Si (001) surface*. Applied Physics Letters, 2000. **77**(25): p. 4139-4141.
29. Hung, C.Y., et al., *Strain directed assembly of nanoparticle arrays within a semiconductor*. Journal of Nanoparticle Research, 1999. **1**(3): p. 329-347.
30. Nieves, A.M., V. Vitek, and T. Sinno, *Monte Carlo analysis of stress-directed phase segregation in binary thin film alloys under nonisothermal annealing*. Applied Physics Letters, 2008. **93**(19): p. 191914.
31. Nieves, A.M., V. Vitek, and T. Sinno, *Atomistic analysis of phase segregation patterning in binary thin films using applied mechanical fields*. Journal of Applied Physics, 2010. **107**(5): p. 054303.
32. Aziz, M.J., *Thermodynamics of diffusion under pressure and stress: Relation to point defect mechanisms*. Applied Physics Letters, 1997. **70**(21): p. 2810-2812.
33. Ghosh, S., et al., *Stress-directed compositional patterning of SiGe substrates for lateral quantum barrier manipulation*. Applied Physics Letters, 2015. **107**(7): p. 072106.
34. Shigley, J., *Mechanical Engineering Design*. 1977, McGraw-Hill: New York, USA.
35. *Technical Data*. 2007; Available from: https://tohnichi.jp/technical/pdf/02_bolt_tightening_e.pdf.
36. Johnson, K.L., *Contact Mechanics*. 1985, Cambridge, UK: Cambridge University Press.

37. Kang, W. and M.T.A. Saif, *In Situ Study of Size and Temperature Dependent Brittle-to-Ductile Transition in Single Crystal Silicon*. Advanced Functional Materials, 2013. **23**(6): p. 713-719.
38. Castrillo, P., et al., *Physical modeling and implementation scheme of native defect diffusion and interdiffusion in SiGe heterostructures for atomistic process simulation*. Journal of Applied Physics, 2011. **109**(10): p. 103502.
39. Metropolis, N., et al., *Equation of State Calculations by Fast Computing Machines*. The Journal of Chemical Physics, 1953. **21**(6): p. 1087-1092.
40. Gillespie, D.T., *Exact stochastic simulation of coupled chemical reactions*. The Journal of Physical Chemistry, 1977. **81**(25): p. 2340-2361.
41. Chatterjee, A. and D.G. Vlachos, *An overview of spatial microscopic and accelerated kinetic Monte Carlo methods*. Journal of Computer-Aided Materials Design, 2007. **14**(2): p. 253-308.
42. Voter, A.F., *Introduction To The Kinetic Monte Carlo Method*, in *Radiation Effects in Solids*, K.E. Sickafus, E.A. Kotomin, and B.P. Uberuaga, Editors. 2007, Springer Netherlands: Dordrecht. p. 1-23.
43. Fichthorn, K.A. and W.H. Weinberg, *Theoretical foundations of dynamical Monte Carlo simulations*. Journal of Chemical Physics, 1991. **95**(2): p. 1090-1096.
44. Dai, J., et al., *On-lattice kinetic Monte Carlo simulations of point defect aggregation in entropically influenced crystalline systems*. Physical Review B, 2005. **72**(13): p. 134102.
45. Mattsson, T.R. and H. Metiu, *Kinetic Monte Carlo simulations of nucleation on a surface with periodic strain: Spatial ordering and island-size distribution*. Applied Physics Letters, 1999. **75**(7): p. 926-928.
46. Mattsson, T.R. and H. Metiu, *Nucleation and coarsening during epitaxy on a substrate subject to periodic strain: Spatial ordering and size uniformity*. Journal of Chemical Physics, 2000. **113**(22): p. 10323-10332.
47. Schulze, T.P. and P. Smereka, *An energy localization principle and its application to fast kinetic Monte Carlo simulation of heteroepitaxial growth*. Journal of the Mechanics and Physics of Solids, 2009. **57**(3): p. 521-538.
48. Schulze, T.P. and P. Smereka, *Simulation of Three-Dimensional Strained Heteroepitaxial Growth Using Kinetic Monte Carlo*. Communications in Computational Physics, 2011. **10**(5): p. 1089-1112.
49. Henkelman, G. and H. Jónsson, *A dimer method for finding saddle points on high dimensional potential surfaces using only first derivatives*. The Journal of Chemical Physics, 1999. **111**(15): p. 7010-7022.
50. Henkelman, G. and H. Jonsson, *Long time scale kinetic Monte Carlo simulations without lattice approximation and predefined event table*. Journal of Chemical Physics, 2001. **115**(21): p. 9657-9666.
51. Merrick, M. and K.A. Fichthorn, *Synchronous relaxation algorithm for parallel kinetic Monte Carlo simulations of thin film growth*. Physical Review E, 2007. **75**(1): p. 011606.
52. Snyder, M.A., A. Chatterjee, and D.G. Vlachos, *Net-event kinetic Monte Carlo for overcoming stiffness in spatially homogeneous and distributed systems*. Computers & Chemical Engineering, 2005. **29**(4): p. 701-712.

53. Katsoulakis, M.A., A.J. Majda, and D.G. Vlachos, *Coarse-grained stochastic processes for microscopic lattice systems*. Proceedings of the National Academy of Sciences, 2003. **100**(3): p. 782-787.
54. Katsoulakis, M.A. and D.G. Vlachos, *Coarse-grained stochastic processes and kinetic Monte Carlo simulators for the diffusion of interacting particles*. The Journal of Chemical Physics, 2003. **119**(18): p. 9412-9427.
55. Collins, S., M. Stamatakis, and D.G. Vlachos, *Adaptive coarse-grained Monte Carlo simulation of reaction and diffusion dynamics in heterogeneous plasma membranes*. BMC Bioinformatics, 2010. **11**(1): p. 1-13.
56. Chatterjee, A., D.G. Vlachos, and M.A. Katsoulakis, *Spatially adaptive lattice coarse-grained Monte Carlo simulations for diffusion of interacting molecules*. Journal of Chemical Physics, 2004. **121**(22): p. 11420-11431.
57. Gillespie, D.T., *Approximate accelerated stochastic simulation of chemically reacting systems*. The Journal of Chemical Physics, 2001. **115**(4): p. 1716-1733.
58. Chatterjee, A. and D.G. Vlachos, *Temporal acceleration of spatially distributed kinetic Monte Carlo simulations*. J. Comput. Phys., 2006. **211**(2): p. 596-615.
59. Chatterjee, A., D.G. Vlachos, and M.A. Katsoulakis, *Binomial distribution based τ -leap accelerated stochastic simulation*. The Journal of Chemical Physics, 2005. **122**(2): p. 024112.
60. Cao, Y., et al., *The numerical stability of leaping methods for stochastic simulation of chemically reacting systems*. The Journal of Chemical Physics, 2004. **121**(24): p. 12169-12178.
61. Cahn, J.W. and J.E. Hilliard, *Free Energy of a Nonuniform System. I. Interfacial Free Energy*. The Journal of Chemical Physics, 1958. **28**(2): p. 258-267.
62. Udaykumar, H.S., et al., *A Sharp Interface Cartesian Grid Method for Simulating Flows with Complex Moving Boundaries*. Journal of Computational Physics, 2001. **174**(1): p. 345-380.
63. Huyakorn, P.S., Y.S. Wu, and N.S. Park, *Multiphase Approach to the Numerical Solution of a Sharp Interface Saltwater Intrusion Problem*. Water Resources Research, 1996. **32**(1): p. 93-102.
64. Ye, T., W. Shyy, and J.N. Chung, *A Fixed-Grid, Sharp-Interface Method for Bubble Dynamics and Phase Change*. Journal of Computational Physics, 2001. **174**(2): p. 781-815.
65. Moelans, N., B. Blanpain, and P. Wollants, *An introduction to phase-field modeling of microstructure evolution*. Calphad, 2008. **32**(2): p. 268-294.
66. Boettinger, W.J., et al., *Phase-Field Simulation of Solidification*. Annual Review of Materials Research, 2002. **32**(1): p. 163-194.
67. Wheeler, A.A., W.J. Boettinger, and G.B. McFadden, *Phase-field model of solute trapping during solidification*. Physical Review E, 1993. **47**(3): p. 1893-1909.
68. Wang, S.-L. and R.F. Sekerka, *Computation of the dendritic operating state at large supercoolings by the phase field model*. Physical Review E, 1996. **53**(4): p. 3760-3776.
69. Lou, Y. and J.L. Bassani, *Guided assembly of nanostructures via elastic interactions*. Journal of the Mechanics and Physics of Solids, 2008. **56**(12): p. 3507-3526.

70. Jancu, J.-M., et al., *Empirical spd^s* tight-binding calculation for cubic semiconductors: General method and material parameters*. Physical Review B, 1998. **57**(11): p. 6493-6507.
71. Sze, S.M. and K.K. Ng, *Physics of semiconductor devices*. 3rd ed. 2007, Hoboken, NJ: Wiley-Interscience. 815 p.
72. Sholl, C.A., *Diffusion correlation factors and atomic displacements for the vacancy mechanism*. Journal of Physics C: Solid State Physics, 1981. **14**(20): p. 2723.
73. Aziz, M.J., et al., *Pressure and stress effects on the diffusion of B and Sb in Si and Si-Ge alloys*. Physical Review B, 2006. **73**(5): p. 054101.
74. Allred, C.L., et al., *Elastic constants of defected and amorphous silicon with the environment-dependent interatomic potential*. Physical Review B, 2004. **70**(13): p. 134113.
75. Centoni, S.A., et al., *First-principles calculation of intrinsic defect formation volumes in silicon*. Physical Review B, 2005. **72**(19): p. 195206.
76. Antonelli, A. and J. Bernholc, *Pressure effects on self-diffusion in silicon*. Physical Review B, 1989. **40**(15): p. 10643-10646.
77. Antonelli, A., E. Kaxiras, and D.J. Chadi, *Vacancy in silicon revisited: Structure and pressure effects*. Physical Review Letters, 1998. **81**(10): p. 2088-2091.
78. Sueoka, K., et al., *DFT study of the effect of hydrostatic pressure on formation and migration enthalpies of intrinsic point defects in single crystal Si*. physica status solidi (c), 2012. **9**(10-11): p. 1947-1951.
79. Tang, M.J., et al., *Intrinsic point defects in crystalline silicon: Tight-binding molecular dynamics studies of self-diffusion, interstitial-vacancy recombination, and formation volumes*. Physical Review B, 1997. **55**(21): p. 14279-14289.
80. Windl, W., et al., *Multiscale Modeling of Stress-Mediated Diffusion in Silicon - Volume Tensors*. MRS Online Proceedings Library, 2001. **677**: p. AA9.4.1-AA9.4.6.
81. Dai, J., W.D. Seider, and T. Sinno, *Lattice kinetic Monte Carlo simulations of defect evolution in crystals at elevated temperature*. Molecular Simulation, 2006. **32**(3-4): p. 305-314.
82. Bortz, A.B., M.H. Kalos, and J.L. Lebowitz, *A new algorithm for Monte Carlo simulation of Ising spin systems*. Journal of Computational Physics, 1975. **17**(1): p. 10-18.
83. Edelman, F., et al., *Crystallization of a-Si_{1-x}Ge_x: Decomposition and modulated structure formation features*. Journal of Crystal Growth, 1995. **157**(1-4): p. 177-180.
84. Gibson, M.A. and J. Bruck, *Efficient exact stochastic simulation of chemical systems with many species and many channels*. Journal of Physical Chemistry A, 2000. **104**(9): p. 1876-1889.
85. Pugh, W., *Skip Lists - a Probabilistic Alternative to Balanced Trees*. Communications of the ACM, 1990. **33**(6): p. 668-676.
86. Plimpton, S., *Fast Parallel Algorithms for Short-Range Molecular-Dynamics*. Journal of Computational Physics, 1995. **117**(1): p. 1-19.

87. Tersoff, J., *Empirical Interatomic Potential for Silicon with Improved Elastic Properties*. Physical Review B, 1988. **38**(14): p. 9902-9905.
88. Tersoff, J., *Modeling Solid-State Chemistry - Interatomic Potentials for Multicomponent Systems*. Physical Review B, 1989. **39**(8): p. 5566-5568.
89. Tersoff, J., *New Empirical-Approach for the Structure and Energy of Covalent Systems*. Physical Review B, 1988. **37**(12): p. 6991-7000.
90. COMSOL. 2015.
91. Brantley, W.A., *Calculated elastic constants for stress problems associated with semiconductor devices*. Journal of Applied Physics, 1973. **44**(1): p. 534-535.
92. Plimpton, S., *Fast Parallel Algorithms for Short-Range Molecular-Dynamics*. J. Comput. Phys., 1995. **117**(1): p. 1-19.
93. Thompson, A.P., S.J. Plimpton, and W. Mattson, *General formulation of pressure and stress tensor for arbitrary many-body interaction potentials under periodic boundary conditions*. J. Chem. Phys., 2009. **131**(15): p. 154107.
94. Kelires, P.C., *Microstructural and elastic properties of silicon-germanium-carbon alloys*. Applied Surface Science, 1996. **102**: p. 12-16.
95. Alivisatos, A.P., *Semiconductor clusters, nanocrystals, and quantum dots*. Science, 1996. **271**(5251): p. 933-937.
96. Wang, C.S. and B.M. Klein, *First-principles electronic structure of Si, Ge, GaP, GaAs, ZnS, and ZnSe. I. Self-consistent energy bands, charge densities, and effective masses*. Physical Review B, 1981. **24**(6): p. 3393-3416.
97. Lianfeng, Y., et al., *Si/SiGe heterostructure parameters for device simulations*. Semiconductor Science and Technology, 2004. **19**(10): p. 1174-1182.
98. Elkurdi, M., et al., *Near-infrared waveguide photodetector with Ge/Si self-assembled quantum dots*. Applied Physics Letters, 2002. **80**(3): p. 509-511.
99. Carlomagno, G.M., *Computational methods and experimental measurements XV*. Vol. 51. 2011: WIT Press.
100. Kaiser, D., et al., *Modeling and simulation of compositional engineering in SiGe films using patterned stress fields*. Molecular Systems Design & Engineering, 2016. **1**(1): p. 74-85.
101. Stolk, P.A., et al., *Physical mechanisms of transient enhanced dopant diffusion in ion-implanted silicon*. Journal of Applied Physics, 1997. **81**(9): p. 6031-6050.
102. Jain, S.C., et al., *Transient enhanced diffusion of boron in Si*. Journal of Applied Physics, 2002. **91**(11): p. 8919-8941.
103. Voronkov, V.V. and R. Falster, *Intrinsic Point Defects and Impurities in Silicon Crystal Growth*. Journal of The Electrochemical Society, 2002. **149**(3): p. G167-G174.
104. Cowern, N.E.B., et al., *Energetics of Self-Interstitial Clusters in Si*. Physical Review Letters, 1999. **82**(22): p. 4460-4463.
105. Petroff, P.M. and A.J.R. De Kock, *Characterization of swirl defects in floating-zone silicon crystals*. Journal of Crystal Growth, 1975. **30**(1): p. 117-124.
106. Fahey, P.M., P.B. Griffin, and J.D. Plummer, *Point-Defects and Dopant Diffusion in Silicon*. Reviews of Modern Physics, 1989. **61**(2): p. 289-384.
107. Griffin, P.B., et al., *Measurement of silicon interstitial diffusivity*. Applied Physics Letters, 1985. **47**(3): p. 319-321.

108. Ural, A., P.B. Griffin, and J.D. Plummer, *Self-Diffusion in Silicon: Similarity between the Properties of Native Point Defects*. Physical Review Letters, 1999. **83**(17): p. 3454-3457.
109. Needs, R.J., *First-principles calculations of self-interstitial defect structures and diffusion paths in silicon*. Journal of Physics: Condensed Matter, 1999. **11**(50): p. 10437.
110. Blöchl, P.E., et al., *First-principles calculations of self-diffusion constants in silicon*. Physical Review Letters, 1993. **70**(16): p. 2435-2438.
111. Voronkov, V.V., *The mechanism of swirl defects formation in silicon*. Journal of Crystal Growth, 1982. **59**(3): p. 625-643.
112. Höchbauer, T., et al., *Physical mechanisms behind the ion-cut in hydrogen implanted silicon*. Journal of Applied Physics, 2002. **92**(5): p. 2335-2342.
113. Sueoka, K., E. Kamiyama, and J. Vanhellemont, *Theoretical study of the impact of stress on the behavior of intrinsic point defects in large-diameter defect-free Si crystals*. Journal of Crystal Growth, 2013. **363**: p. 97-104.
114. Prasad, M. and T. Sinno, *Internally consistent approach for modeling solid-state aggregation. I. Atomistic calculations of vacancy clustering in silicon*. Physical Review B, 2003. **68**(4): p. 045206.
115. Prasad, M. and T. Sinno, *Internally consistent approach for modeling solid-state aggregation. II. Mean-field representation of atomistic processes*. Physical Review B, 2003. **68**(4): p. 045607.
116. Prasad, M. and T. Sinno, *Atomistic-to-continuum description of vacancy cluster properties in crystalline silicon*. Applied Physics Letters, 2002. **80**(11): p. 1951-1953.
117. Kapur, S.S., A.M. Nieves, and T. Sinno, *Detailed microscopic analysis of self-interstitial aggregation in silicon. II. Thermodynamic analysis of single clusters*. Physical Review B, 2010. **82**(4): p. 045206.
118. Kapur, S.S., et al., *Role of configurational entropy in the thermodynamics of clusters of point defects in crystalline solids*. Physical Review B, 2005. **72**(1): p. 014119.
119. Kapur, S.S., M. Prasad, and T. Sinno, *Carbon-mediated aggregation of self-interstitials in silicon: A large-scale molecular dynamics study*. Physical Review B, 2004. **69**(15): p. 155214.
120. Kapur, S.S. and T. Sinno, *Entropic origins of stability in silicon interstitial clusters*. Applied Physics Letters, 2008. **93**(22): p. 221911.
121. Kapur, S.S. and T. Sinno, *Detailed microscopic analysis of self-interstitial aggregation in silicon. I. Direct molecular dynamics simulations of aggregation*. Physical Review B, 2010. **82**(4): p. 045205.
122. Rice, J.R., *Continuum Mechanics and Thermodynamics of Plasticity in Relation to Microscale Deformation Mechanisms*, in *Constitutive Equations in Plasticity*, A.S. Argon, Editor. 1975, MIT Press: Cambridge, MA. p. 23-79.
123. Aziz, M.J., *Stress effects on defects and dopant diffusion in Si*. Materials Science in Semiconductor Processing, 2001. **4**(5): p. 397-403.
124. Erhart, P. and K. Albe, *Analytical potential for atomistic simulations of silicon, carbon, and silicon carbide*. Physical Review B, 2005. **71**(3): p. 035211.

125. Justo, J.F., et al., *Interatomic potential for silicon defects and disordered phases*. Physical Review B, 1998. **58**(5): p. 2539-2550.
126. Stillinger, F.H. and T.A. Weber, *Computer simulation of local order in condensed phases of silicon*. Physical Review B, 1985. **31**(8): p. 5262-5271.
127. Baskes, M.I., *Modified embedded-atom potentials for cubic materials and impurities*. Physical Review B, 1992. **46**(5): p. 2727-2742.
128. Larkins, F.P. and A.M. Stoneham, *Lattice distortion near vacancies in diamond and silicon. II*. Journal of Physics C: Solid State Physics, 1971. **4**(2): p. 154-163.
129. Cook, S.J. and P. Clancy, *Comparison of semi-empirical potential functions for silicon and germanium*. Physical Review B, 1993. **47**(13): p. 7686-7699.
130. Kaczmarek, M., R. Rurali, and E. Hernández, *Reversible scaling simulations of the melting transition in silicon*. Physical Review B, 2004. **69**(21): p. 214105.
131. Seunghwa, R., et al., *Improved modified embedded-atom method potentials for gold and silicon*. Modelling and Simulation in Materials Science and Engineering, 2009. **17**(7): p. 075008.
132. Kevrekidis, I.G., et al., *Equation-Free, Coarse-Grained Multiscale Computation: Enabling Microscopic Simulators to Perform System-Level Analysis*. Communications in Mathematical Sciences, 2003. **1**(4): p. 715-762.
133. Kevrekidis, I.G., C.W. Gear, and G. Hummer, *Equation-free: The computer-aided analysis of complex multiscale systems*. AIChE Journal, 2004. **50**(7): p. 1346-1355.
134. Liu, P., Y.W. Zhang, and C. Lu, *Computer simulations of the Stranski-Krastanov growth of heteroepitaxial films with elastic anisotropy*. Surface Science, 2003. **526**(3): p. 375-382.
135. Chiu, C.H. and Z. Huang, *Numerical simulation for the formation of nanostructures on the Stranski-Krastanov systems by surface undulation*. Journal of Applied Physics, 2007. **101**(11): p. 113540.
136. Ngo, T.T., et al., *Simulation model for self-ordering of strained islands in molecular-beam epitaxy*. Physical Review B, 1996. **53**(15): p. 9618-9621.
137. Meixner, M., et al., *Formation of island chains in SiGe/Si heteroepitaxy by elastic anisotropy*. Physical Review B, 2001. **64**(24): p. 245307.
138. Nurminen, L., A. Kuronen, and K. Kaski, *Kinetic Monte Carlo simulation of nucleation on patterned substrates*. Physical Review B, 2000. **63**(3): p. 035407.
139. Much, F. and M. Biehl, *Simulation of wetting-layer and island formation in heteroepitaxial growth*. Europhysics Letters, 2003. **63**(1): p. 14-20.
140. Haftel, M.I., et al., *Molecular-Dynamics Observations of Interdiffusion and Stranski-Krastanov Growth in the Early Film Deposition of Au on Ag(110)*. Physical Review Letters, 1994. **72**(12): p. 1858-1861.
141. Rafii-Tabar, H., H. Kamiyama, and M. Cross, *Molecular dynamics simulation of adsorption of Ag particles on a graphite substrate*. Surface Science, 1997. **385**(1): p. 187-199.